Energy Dispersed Ion Signatures at Auroral and Subauroral Latitudes

A Thesis Submitted to the
College of Graduate Studies and Research
in Partial Fulfillment of the Requirements
for the degree of Master of Science
in the Department of Physics and Engineering Physics
University of Saskatchewan
Saskatoon

By

Robert Douglas Schwab

Permission to Use

In presenting this thesis in partial fulfilment of the requirements for a Postgraduate degree from the University of Saskatchewan, I agree that the Libraries of this University may make it freely available for inspection. I further agree that permission for copying of this thesis in any manner, in whole or in part, for scholarly purposes may be granted by the professor or professors who supervised my thesis work or, in their absence, by the Head of the Department or the Dean of the College in which my thesis work was done. It is understood that any copying or publication or use of this thesis or parts thereof for financial gain shall not be allowed without my written permission. It is also understood that due recognition shall be given to me and to the University of Saskatchewan in any scholarly use which may be made of any material in my thesis.

Requests for permission to copy or to make other use of material in this thesis in whole or part should be addressed to:

Head of the Department of Physics and Engineering Physics
116 Science Place
University of Saskatchewan
Saskatoon, Saskatchewan
Canada S7N 5E2

Abstract

During magnetically disturbed periods, the spatially and temporally structured electron precipitation in the auroral zone creates a significant population of thermal secondary ions. Acceleration mechanisms exist that are capable of energizing the thermal population to suprathermal energies (1 eV to 1 keV). Suprathermal ions escape into the magnetosphere and undergo "bounce" motion along magnetic field lines. These ions are bound to the magnetic flux tubes, which undergo $\vec{E}\times\vec{B}$ convective drift within the magnetosphere. Magnetospheric convection transports flux tubes of bouncing suprathermal ions through the auroral zone and the subauroral polarization stream (SAPS) regions. Precipitating suprathermal ions enhance ionospheric plasma density structure and constitute a possible source for the enhanced echo occurrence observed by ground-based radars in the SAPS region. Satellite energy spectrometer data often show multiple bands of suprathermal particles with enhanced number and energy flux, and with an energy increase with increasing latitude. The present work examines the hypothesis that these signatures are the result of thermal secondary ions that have been accelerated out of the auroral ionosphere over the short time scales characterizing bursts of intense auroral electron precipitation. The analysis of three events of energy-dispersed ion signatures was facilitated by three-dimensional ion tracing software developed for this thesis. The short-lived acceleration hypothesis can account for the energy-dispersed ion signatures if there exist inter-hemispheric field aligned potentials of the order of 100 V. If the source of the ions is within the auroral zone, the suprathermal ions observed in the SAPS region are most likely to be O^+ ions. The long bounce period of O^+ (compared to H^+) allows convection to transport O^+ auroral ions equatorward through a convection reversal, into the SAPS region during a single half-bounce.

Acknowledgements

I would like to take this opportunity to thank all those people, without whom, this thesis would not have been possible. First and foremost, I thank Dr. George Sofko, my supervisor, for his support and encouragement. His passion for science is truly contagious and inspired this research from the very beginning. I thank Dr. Kathryn McWilliams, my co-supervisor, for her positive comments, her invaluable editorial skills, and for asking the questions which helped keep the project in focus. I would like to thank my committee members, Drs. Sasha Koustov, Glenn Hussey, Chijin Xiao, and Robert Johanson for their advice, encouragement and insightful comments.

Many thanks go out to all members of the Institute of Space and Atmospheric Studies and the Department of Physics and Engineering Physics for providing the facility, the computer tools, an ideal working environment and all other necessary services, without which, my research would not have been possible. Raw DMSP Data and processing software was provided by Fred Rich of the Air Force Research Laboratory. Financial support, for which I greatly appreciate, was provided from the NSERC Team Discovery Grant to Drs A. V. Koustov and G. J. Sofko, and from ISAS scholarships, most notably, the B.W. Currie Memorial Graduate Scholarship and the Jack Henry Meek Scholarship.

My experience would not have been nearly as enjoyable without the support and friendship of my fellow graduate students, Robyn Drayton Fiori, Robert Gillies, James Gorin and Jeff Pfeiffer. Special thanks is extended to Reid McDonald, for his editorial services, guidance and friendship.

Finally, I extend my deepest gratitude to my family for their constant support, love, encouragement, and of course their sense of humour, which helped to keep things in perspective.

Contents

List of Tables

List of Figures

List of Abbreviations

AE-C	Atmospheric Explorer C
APS	Auroral Post-Secondary
ATS-6	Applications Technology Satellite 6
CASSIOPE	CAScade, Smallsat and IOnospheric Polar Explorer
DMSP	Defense Meteorological Satellite Program
DAPS	Dusk Auroral Post-Secondary
DE-1, DE-2	Dynamics Explorer 1 and 2
dE_f	Differential Energy Flux
dN_f	Differential Number Flux
D_{st}	Disturbance Storm Time Index
e-POP	Enhanced Polar Outflow Probe
FAST	Fast Auroral SnapshoT
GUVI	Global Ultraviolet Imager
ILAT	Invariant Latitude
IMF	Interplanetary Magnetic Field
IMS	Ion Mass Spectrometer
IRM	Imagine and Rapid-scan Mass Spectrometer
K_p	Index of Geomagnetic Activity
LEO	Low Earth Orbit
LEP	Low Energy Particle
LP	Langmuir Probe
LT	Local Time
MAPS	Morning Auroral Post-Secondary
MLAT	Magnetic Latitude
MLT	Magnetic Local Time
PSBL	Plasma Sheet Boundary Layer
RPA	Retarding Potential Analyzer
SAID	Subauroral Ion Drifts
SAPS	Subauroral Polarization Stream
SAPS	Subauroral Post-Secondary
SMS	Suprathermal Mass Spectrometer
SSIES	Special Sensor Ion and Electron Scintillation Monitor
SSJ/4	Special Sensor Precipitating Electron and Ion Spectrometer
SuperDARN	Super Dual Auroral Radar Network
TIMED	Thermosphere Ionosphere Mesosphere Energy and Dynamics
TOF	Time of Flight

Chapter 1

Introduction

The Sun is not only a source of light and heat but is also a giant nuclear pot of hydrogen and helium ions which produces a continuous stream of outflowing plasma known as the solar wind. The emitted plasma is completely ionized and quasi-neutral and expands through the solar system in all directions with a velocity which is normally from 300 to 800 km/s [*Cowley*, 1995], but which can exceed 2000 km/s (e.g., *Skoug et al.* [2004]). Carried with the plasma is the Sun's magnetic field, also known as the interplanetary magnetic field (IMF). The IMF extends outward towards the heliopause, the boundary where the pressure due to the solar wind plasma is balanced by the pressure due to plasma of interstellar medium [*Holzer*, 1989]. The Sun physically interacts with every object within this boundary, including the Earth.

The Earth has its own magnetic field which is produced by the electric currents generated by the convection of the liquid outer-core of the Earth [*Glatzmaier and Roberts*, 1995]. Unperturbed, the magnetic field of the Earth resembles the dipole configuration of the magnetic field of a simple bar magnet. The axis of the Earth's dipole is tilted approximately 11° off the axis of rotation, with the magnetic north pole positioned near the geographic south pole. The dipole field of the Earth creates a magnetic cavity in the IMF. This cavity, known as the magnetosphere, is compressed on the dayside of the Earth and is stretched into an elongated tail by the streaming IMF. However, at distances up to 5 Earth radii (R_E), the magnetic field still resembles a magnetic dipole.

The magnetosphere is strongly influenced by the IMF, which has highly variable plasma density, plasma velocity, and magnetic field strength. During active solar events, the interaction between the solar wind and the magnetosphere can lead to

magnetic storms, which can damage or destroy satellites, hinder radio communications, and even disrupt electrical power grids. The solar wind-magnetosphere interaction is also responsible for the aurora borealis, one of the most beautiful natural light-shows in the world. One studies the solar-terrestrial near-Earth environment in an attempt to understand the very dynamic processes of the magnetosphere with hopes of better forecasting space weather.

The following two sections describe the regions of the magnetosphere and the ionosphere based largely on information from *Hargreaves* [1992], *Baumjohann and Treumann* [1996], and *Kivelson and Russell* [1995]. Section 1.4 is an overview of the objectives of the thesis and provides the thesis outline.

1.1 The magnetosphere

From numerous observations of magnetic fields and particle characteristics, the magnetosphere of the Earth can be broadly categorized into the regions as shown in Figure 1.1. In this figure, the Sun is located to the left, and the north pole is located at the top of the Earth. The solar wind, which is comprised mainly of hydrogen ions with a density normally ranging from 1 to 15 cm^{-3} but which can exceed 50 cm^{-3}, streams outward from the Sun at supersonic speeds [*McPherron*, 1995]. The interaction of the supersonic solar wind and the magnetic field of the Earth creates a bow shock, indicated with the dashed line.

Earthward of the bow shock, the speed of the solar wind drops to subsonic values in the magnetosheath. The convection inside the sun facing side of the magnetosheath is turbulent and the plasma density is enhanced by a factor of 3 to 4. The solar wind dominates the plasma and magnetic field motion in this region, and the plasma is driven tailward around the magnetosphere where the density is more comparable to that of the solar wind.

The boundary where the solar wind pressure is in dynamic equilibrium with the magnetospheric pressure is called the magnetopause and is illustrated in Figure 1.1. When the IMF is directed southward, magnetic flux from the IMF can connect or

"merge" with the magnetic field lines of the Earth on the dayside creating an opening for the solar wind particles to enter the magnetosphere via the polar cusps. These merged magnetic field lines, which have one end tied to the Earth and the other tied to the solar wind, are called open field lines. The open fields lines convect tailward, dragged by the solar wind.

The mantle is a region of open field lines, located poleward of the cusp, extending antisunward towards the tail. The plasma density in the mantle region gradually decreases with increasing distance from the magnetopause, eventually dropping to values typically less than 0.1 cm^{-3} within the tail lobe. The magnetic field lines in the tail lobes extend to 100–200 R_E [*Nishida et al.*, 1995]. The plasma sheet is

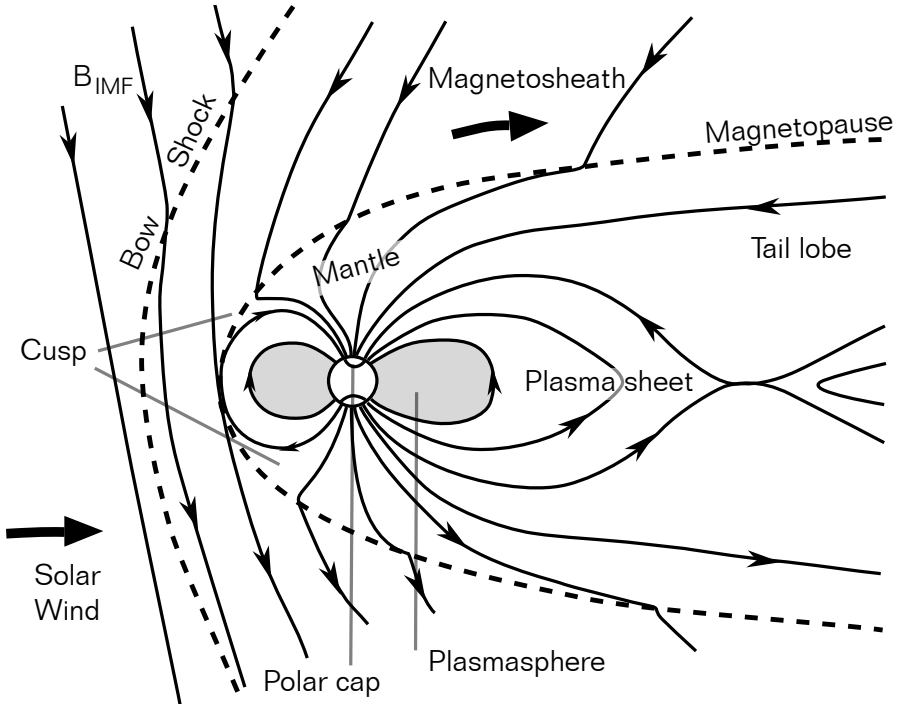

Figure 1.1: Schematic diagram of the magnetosphere of the Earth. Adapted from *Hughes* [1995].

composed of the central plasma sheet and the plasma sheet boundary layer (PSBL). The PSBL is the boundary layer separating the central plasma sheet and the tail lobes. Densities in the central plasma sheet range from 0.1 to 1 cm^{-3}, which is only slightly greater than the density of $\sim$0.1 cm^{-3} in the PSBL. The particles in the

central plasma sheet also have higher energies, with the electron energies around 1 keV and the ion energies ranging from 5 to 10 keV, compared to only $\sim$ 100 eV in the PSBL.

Within approximately 5 R_E of Earth is a region of corotating plasma known as the plasmasphere. In this region the density of the plasma ranges from 100 to 1000 cm^{-3}, but it is mainly comprised of cold ions and electrons whose energies are less than 0.1 eV. The region between the plasmasphere and plasma sheet is known as the plasma trough. The boundary between the plasmasphere and the trough is the plasmapause, across which densities drop precipitously from around 100 cm^{-3} to around 1 cm^{-3}. During magnetically disturbed periods, the plasmasphere and plasma trough regions are host to relatively hot particles with energies ranging from 20 to 300 keV that are injected from the tail. The hot ions are trapped, bouncing along field lines, and drifting around the Earth. These highly energetic particles are also known as the ring current particles as they establish a large current circulating westward around the Earth that can persist for days during magnetically disturbed periods [*Wolf*, 1995]. The plasmasphere is also host to extremely hot particles with energies reaching up to 400 MeV. These particles make up the radiation belts, and they have large enough energies to cause damage to electrical instruments or living tissue of people travelling in this region. These charged particles circulate the Earth much like the ring current particles but the density of the radiation belt ions and electrons is too low to constitute a significant fraction of the ring current [*Wolf*, 1995].

1.2 The ionosphere

Stretching from an altitude of approximately 60 km to roughly 1000 to 2000 km is an electrically conducting layer of the atmosphere called the ionosphere. Ion recombination rates in this region are sufficiently low that a significant, quasi-stable plasma population exists. The main ionizing mechanism is photo-ionization, whereby the interaction of solar photons with neutral atoms and molecules can dissociate

electrons, creating ion-electron pairs. The plasma of the ionosphere, like the solar wind plasma, is quasi-neutral.

The ionosphere is divided into three regions characterized by the plasma number density. Figure 1.2 illustrates the typical values of the electron density in each region for both day and night conditions [*Hargreaves*, 1992]. The D region, located from ∼60 to 90 km, suffers from higher recombination rates due to collisions with the highly abundant neutrals in the lower ionosphere, and it has a low peak in electron density. During the night, this peak can disappear completely. The E region, which ranges from altitudes of about 90 to 180 km, has a higher peak electron density ranging from approximately 10^3 cm^{-3} at night to 10^5 cm^{-3} during the day. The F region has the largest peak electron density located at an altitude of about 300 km with values of 10^5 cm^{-3} at night to 10^6 cm^{-3} during the day. Note that during the day the F region is often observed to be further divided into the F_2 and the F_1 peaks. The F_1 peak, which is more of a ledge on the F_2 peak, can be described by the Chapman theory of ionospheric layers [*Hargreaves*, 1992]. The F_2 peak requires one to consider diffusion to describe its behavior. A more complete discussion of the physics of the layers of the ionosphere can be found in Chapters 6 and 7 of *Hargreaves* [1992].

As an electrically conducting layer, the ionosphere not only acts as a medium for electric currents, but is a giant energy-absorbing and refracting layer for radio waves. In fact, the labeling of the E region came about when E. V. Appleton and M. A. F. Barnett timed the reflection of pulsed radio waves from the ionosphere in 1925. They used E to label the electric vector of the return signal which then became the name of the reflecting layer itself [*Russell*, 1995]. Labeling of the F region and D region followed after the discovery of reflections at higher and lower altitudes.

The composition of the ionosphere consists of both ionized and neutral atoms and molecules as illustrated in Figure 1.3. This plot is an example of the density of the ions and electrons, as well as the neutral atoms and molecules, as a function of height. Although the plasma density of the ionosphere is significant enough to have strong measurable electrical properties, the density of the neutral particles is

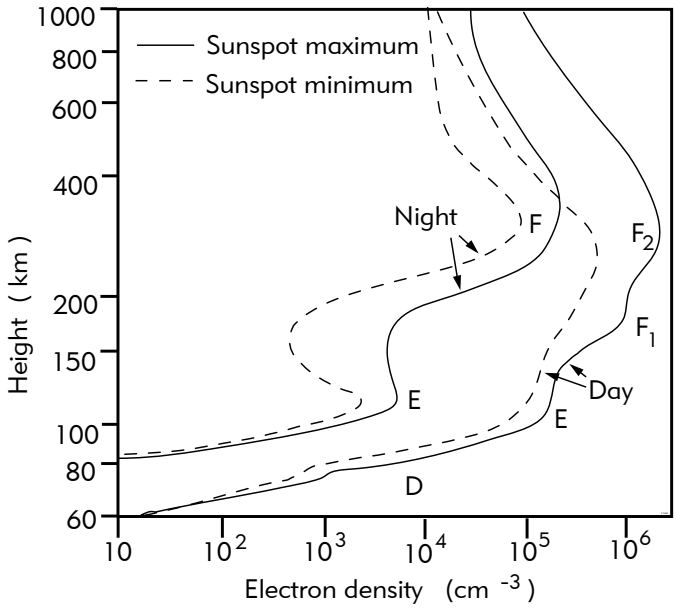

Figure 1.2: Electron density profiles of the ionosphere of the Earth. Includes day and night profiles for sunspot maximum (solid lines) and minimum (dashed lines). From *Hargreaves* [1992].

between 2 to 3 orders of magnitude larger than the electron density. Figure 1.3 also illustrates that, like the electron and ion density, the ion composition is also a function of height. Below 150 km, the ionosphere is dominated by molecular oxygen (O_2^+) and nitrogen oxide (NO^+). Atomic oxygen (O^+) is dominant in the ionosphere from roughly 150 to 1000 km. Above $\sim$ 1000 km, the density of O^+ drops off and hydrogen is the dominant species, and therefore this region is often referred to as the protonosphere. Since the ionosphere is quasi-neutral, the electron density profile, highlighted by the dark band, is comparable to the sum of all the ion density profiles.

1.3 The ionosphere as a source of magnetospheric plasma

During periods of strong southward IMF, the magnetosphere is strongly coupled to the solar wind. Reconnection in the dayside and nightside is enhanced, which

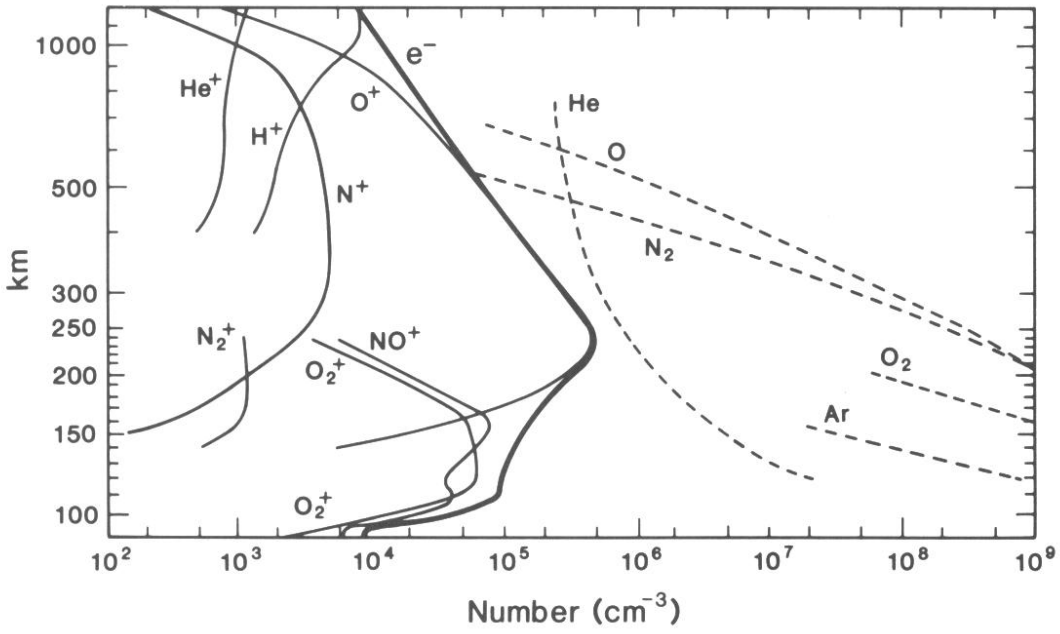

Figure 1.3: Ion, electron, and neutral atom and molecule densities as a function of height. From *Johnson* [1969].

strongly drives magnetospheric convection and creates strong magnetospheric and ionospheric current systems, such as the ring current. This period of enhanced magnetic activity is known as a magnetic storm. During magnetic storms, energy from the solar wind can be stored in the stretched magnetic field lines in the magnetotail. The sudden release of this energy into the magnetosphere is called a magnetic substorm [*Baumjohann and Treumann*, 1996]. One of the most easily observed characteristics of magnetic substorms is the aurora borealis (or aurora australis in the southern polar region) [*Carlson and Egeland*, 1995].

The aurora is a secondary effect of the precipitation of high energy (0.5–20 keV) electrons into the ionosphere. When these particles collide with neutral atoms and molecules, some of the kinetic energy of the precipitating electrons is converted to stored chemical energy of the neutral atoms and molecules. As these excited particles return to their ground state, energy is released in the form of light.

The precipitating auroral particles originate from the plasma sheet, which maps to the ionosphere as an oval, the auroral oval, at high magnetic latitudes normally

from 65° to 77° magnetic latitude (MLAT). The flow of these electrons (and ions) along the field lines produces currents called field-aligned currents (FACs). Poleward of the auroral oval is the polar cap, which corresponds to the zone of open field lines surrounding the magnetic pole [*Hughes*, 1995].

During the substorm, the auroral zone is a very dynamic region and the aurora is just one indicator of the enhanced magnetic activity. In addition to producing the aurora, the precipitation of high energy electrons creates a significant secondary plasma population. It only takes ∼36 eV of energy to create one ion-electron pair, which implies that a typical auroral electron with an energy of 1 keV has the potential to create over 25 ion-electron pairs [*Carlson and Egeland*, 1995]. It is this population that is a source of low-energy plasma for the plasma sheet during magnetically disturbed periods as inferred from numerous satellite observations. For example, *Lennartsson and Sharp* [1982] showed that the density ratio of O^+ to H^+ in the plasma sheet region increases by a factor of 1.2–4.7 during magnetically disturbed conditions. As noted in Section 1.2, the ionosphere has a significant population of O^+ but the solar wind does not. This is direct evidence for the ionosphere acting as a source of plasma for the magnetosphere.

In the nightside auroral zone photoionization can not take place, so electron precipitation is the primary ionization mechanism in the ionosphere. However, the energy of the secondary ion-electron pairs is low, too low for them to escape into the magnetosphere. Since the observations show that some do escape, the implication is that during disturbed periods, strong parallel and/or perpendicular acceleration mechanisms that are capable of accelerating the auroral secondary ions from thermal to suprathermal energies are active in the auroral zone. This is supported by the satellite observations of upward flowing ion clusters with a velocity distribution that varies from being aligned along the magnetic field (ion beams) to being perpendicular to the magnetic field (ion conics), implying that both parallel and perpendicular acceleration mechanisms must exist [*Wahlund et al.*, 1992, and references therein]. As the majority of the ionospheric ions that populate the plasma sheet at suprathermal energies are the secondary ions created from primary electron precipitation, *Sofko*

et al. [2007] termed these ions auroral post-secondary (APS) ions.

1.4 Objectives and thesis outline

The present work examines the hypothesis that the acceleration of ionospheric ions from thermal (less than 1 eV) to suprathermal energies (from ∼1 eV up to 1 keV [*Whalen et al.*, 1990]) within the auroral zone occurs over short time scales relative to the time scales of the bounce motion of the ions. Observations of suprathermal ion populations in the magnetosphere and the high altitude ionosphere are presented, and these populations are shown to constitute significant density and charge contributions in both auroral and subauroral regions.

The suprathermal ions are often observed in multiple banded energy-dispersed structures, where the energy of the measured ion flux increases with increasing latitude. The present work examines if the proposed "short-lived ionospheric acceleration" hypothesis can account for the magnitude of the measured ion energy dispersion. Three-dimensional ion tracing software was developed to aid this analysis.

The format of the thesis is as follows. Chapter 2 reviews the basic physics explaining the motion of ions in the magnetosphere and explores magnetospheric convection mapping to the high-latitude ionosphere. One major point of this chapter is that the suprathermal ions, like thermal ions, convect with the magnetic flux tubes to which they are bound. Chapter 3 discusses the implications of strong subauroral convective drifts of suprathermal ions in the nightside inner magnetosphere and conjugate subauroral ionosphere. This region of enhanced flow is called the subauroral polarization stream (SAPS). The implications of the production and subsequent convection of suprathermal ions during strong auroral events is shown to be consistent with ground based radar observations of enhanced echoes in the SAPS region.

Chapter 4 discusses observations from previous satellite data in which suprathermal ions in the magnetospheric region mapping to the low-latitude portion of the auroral oval are illustrated. Two conflicting explanations previously proposed to explain the energy-dispersing mechanism are discussed. This chapter provides a

new theory, which attempts to consolidate the differences between the conflicting explanations and which is consistent with the hypothesis that the acceleration of the ionospheric ions from thermal to suprathermal energies occurs over a short time period relative to the bounce period of the ions.

Chapter 5 presents low-altitude (840 km) satellite data highlighting that suprathermal ions are directly observed in the SAPS region and that the number density of these ions is at least comparable to or greater than that of ions with energies ranging from 1 to 30 keV. It also emphasizes that the energy-dispersed suprathermal ion signatures with the characteristic increase in energy with increasing latitude are observed in both the auroral and the SAPS regions.

Chapter 6 discusses first the design and testing of the three dimensional ion tracing software. This chapter then analyzes the ability of the new dispersion theory presented in Chapter 4 to account for the magnitude of the energy-dispersed signature for three events. Two of these events are at the centre of the conflicting theories discussed in Chapter 4. The third event is an example taken from Chapter 5, for which an energy-dispersed ion signature was observed in the SAPS region.

Chapter 2

Physics of space plasma

Understanding ionized particle drifts created by electromagnetic fields is fundamental to space physics. Particle drifts in the magnetosphere lead to large-scale current systems such as the ring current, the cross tail current and field-aligned currents. The key particle motions in space physics are the $\vec{E}\times\vec{B}$ or convective drift, the curvature-gradient drift, and the field-parallel bounce motion. These are introduced in Section 2.1. Section 2.2 contains derivations of the adiabatic invariants of charged particle motion in a dipole magnetic field. This section highlights that although there are three adiabatic invariants, only the first is valid for suprathermal ions during magnetically disturbed periods. Section 2.3 introduces magnetospheric convection which maps to the high-latitude ionosphere.

2.1 Ionized particle motion

Consider an ion moving with a velocity $\vec{v}_0$ in a magnetic field $\vec{B} = B\hat{z}$, as illustrated in Figure 2.1(a). The ion experiences the Lorentz Force, $\vec{F}_L$, which is related to the particle charge q, velocity $\vec{v}$, and the magnetic field,

$$\vec{F_L} = q\vec{v} \times \vec{B}. \tag{2.1}$$

Using Newton's Second Law one may write the equation of motion of the charged particle as

$$m\vec{a} = q\vec{v} \times \vec{B}, \tag{2.2}$$

whose component form is given by:

$$\dot{v}_x = \frac{qB}{m} v_y; \quad \dot{v}_y = -\frac{qB}{m} v_x. \tag{2.3}$$

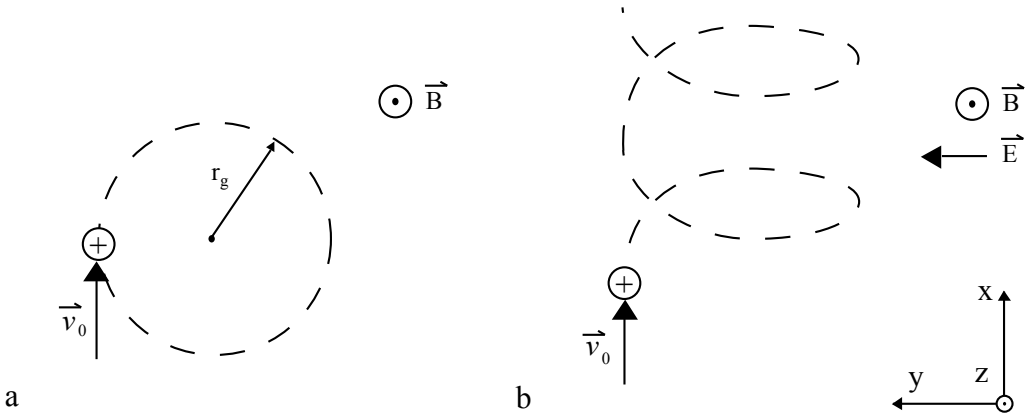

Figure 2.1: a) Ion motion in a static magnetic field. b) Ion motion in crossed electric and magnetic fields.

By differentiating Equation 2.3 and substituting $\dot{v}_x$ and $\dot{v}_y$ into the result, one finds

$$\ddot{v}_x + \left(\frac{qB}{m}\right)^2 v_x = 0; \quad \ddot{v}_y + \left(\frac{qB}{m}\right)^2 v_y = 0, \tag{2.4}$$

which are two second order differential equations. Using the initial condition $\vec{v}_{initial} = v_0\hat{x}$ illustrated in Figure 2.1(a), the solutions are

$$v_x = v_0 \cos\left(\frac{qB}{m}t\right); \quad v_y = v_0 \sin\left(\frac{qB}{m}t\right), \tag{2.5}$$

which describe circular motion. The term $\left(\frac{qB}{m}\right)$ is the gyrofrequency. It is also known as the cyclotron frequency, ω_c. One can quickly see that the period of gyration, given by

$$T_c = \frac{2\pi}{w_c} = \frac{2\pi m}{qB}, \tag{2.6}$$

is independent of the particle energy. Also, by substituting the relation for centripetal acceleration

$$a_c = \frac{v^2}{r}, \tag{2.7}$$

into Equation 2.2, the radius of gyration is determined to be

$$r_g = \frac{mv}{qB}. \tag{2.8}$$

Because the radius of gyration is proportional to the particle mass, ions have a much larger radius of gyration than electrons with the same velocity. Also note that

due to the charge dependence of the Lorentz force, ions rotate with a left-handed sense and electrons with a right-handed sense around the magnetic field. If there is a component of the velocity aligned along the magnetic field line, the particle maintains that component along $\vec{B}$ as it gyrates in circles perpendicular to $\vec{B}$, thereby tracing out a helical pattern. The angle between $\vec{B}$ and the total velocity vector $\vec{v}$ is called the pitch angle α. The pitch angle can be written as a function of the perpendicular and parallel components of the particle velocity as

$$\tan\alpha = \frac{v_\perp}{v_\parallel}. \tag{2.9}$$

Consider the application of an electric field $\vec{E} = E\hat{y}$ as illustrated in Figure 2.1(b). Incorporating the equation for the Coulomb Force

$$\vec{F}_c = q\vec{E}, \tag{2.10}$$

into the equation of motion, Equation 2.2, results in the following solution,

$$v_x = v_0 \cos\left(\frac{qB}{m}t\right) + \frac{E}{B}; \quad v_y = v_0 \sin\left(\frac{qB}{m}t\right). \tag{2.11}$$

Effectively, this solution is the gyromotion calculated in the purely static magnetic field case superposed on a constant drift of the centre of gyration, which is proportional to E/B and is directed perpendicular to both $\vec{E}$ and $\vec{B}$. In vector format this drift is written as

$$\vec{v}_{E\times B} = \frac{\vec{E}\times\vec{B}}{B^2}, \tag{2.12}$$

and is called the $\vec{E}\times\vec{B}$ or convective drift. Note that this drift is independent of the charge of the particle and so ions and electrons in a collisionless plasma undergo $\vec{E}\times\vec{B}$ drift at the same speed and in the same direction.

In space plasma physics, it is common to study the motion of the centre of gyration of the charged particles while implicitly understanding that the charged particles are continuously gyrating around this centre. This is called the guiding centre approach to studying charged particle motion. For a particle subject to an external force $\vec{F}$ in the magnetoplasma, the resulting drift velocity will be

$$\vec{v} = \frac{\vec{F}\times\vec{B}}{qB^2}. \tag{2.13}$$

One notes that the substitution of Equation 2.10 into 2.13 results in Equation 2.12.

Equation 2.13 is called the general drift equation and it can be used to help derive the curvature and gradient drifts. For inhomogeneous magnetic fields, such as the Earth's dipole field, the force $\vec{F}_{grad}$ on charged particles due to the magnetic field gradient is

$$\vec{F}_{grad} = -\mu \nabla B, \tag{2.14}$$

where μ is the magnetic moment. As a charged particle travels parallel to the magnetic field and experiences an increasing B, this gradient force increases and is directed opposite to $\vec{B}$. This causes the parallel velocity to decrease. The point where the parallel velocity reaches zero is known as the mirror point and the particle is said to "bounce", after which it moves in the opposite direction. The invariance of μ is discussed in Section 2.2.

As the particle bounces between hemispheres in the dipole field of the Earth, it will also experience a gradient force perpendicular to $\vec{B}$ since the magnetic field increases in strength at distances closer to the Earth. Taking the perpendicular component of the gradient force from Equation 2.14 and substituting it into the general drift equation (Equation 2.13) results in an expression for the gradient drift $\vec{v}_{grad}$ as a function of the perpendicular energy $K_\perp$ of the particle, namely

$$\vec{v}_{grad} = \frac{mv_\perp^2}{2qB^3}(\vec{B} \times \nabla_\perp B) = \frac{K_\perp}{qB^3}(\vec{B} \times \nabla_\perp B). \tag{2.15}$$

Particles travelling along the curved magnetic field line also experience a force $\vec{F}_{curv}$ due to the curved trajectory (centrifugal tendency), according to the centrifugal force expression:

$$\vec{F}_{curv} = \frac{mv_\parallel^2}{\rho_c}\hat{n}, \tag{2.16}$$

where ρ_c is the local radius of curvature, $v_\parallel$ is the velocity parallel to $\vec{B}$ and $\hat{n}$ is the unit vector away from the centre of curvature. Substituting Equation 2.16 into Equation 2.13 results in an expression for the curvature drift $\vec{v_c}$ as function of the parallel energy $K_\parallel$ of the particle,

$$\vec{v_c} = \frac{mv_\parallel^2}{qB^2\rho_c}(\hat{n} \times \vec{B}) = \frac{2K_\parallel}{qB^2\rho_c}(\hat{n} \times \vec{B}). \tag{2.17}$$

For a dipole magnetic field, one can show that

$$\frac{\hat{n}}{\rho_c} = -\frac{\nabla_\perp B}{B}, \tag{2.18}$$

and Equation 2.17 becomes

$$\vec{v_c} = \frac{2K_\parallel}{qB^3}(\vec{B} \times \nabla_\perp B). \tag{2.19}$$

The sum of the curvature drift (Equation 2.17) and the gradient drift (Equation 2.15) is known as the curvature-gradient drift,

$$\vec{v}_{cg} = \frac{K_\perp + 2K_\parallel}{qB^3}(\vec{B} \times \nabla_\perp B). \tag{2.20}$$

This drift is a function of both the parallel and perpendicular kinetic energy of the particle. It is also dependent on the charge of the particle. Ions drift westward in the $\vec{B} \times \nabla_\perp B$ direction and electrons drift eastward.

The complete motion of the charged particles is the vector sum of the convective and curvature-gradient drifts perpendicular to $\vec{B}$ and the parallel drift along $\vec{B}$. However, for low energy ions and electrons, the curvature-gradient drift is small in comparison to the $\vec{E}\times\vec{B}$ drift and can be neglected. This is true for ions with an energy up to $\sim$ 1500 eV when the ionospheric $\vec{E}\times\vec{B}$ drifts are on the order of 500 m/s. At this energy, the effective longitudinal drift due to the curvature-gradient drift averaged over a bounce period is less than 10% of that due to the $\vec{E}\times\vec{B}$ drift. A complete derivation of the bounce-averaged curvature-gradient drift is provided in Appendix B.2. In the present work, the term "drift-bounce motion" refers to the motion of charged particles due to the combined $\vec{E}\times\vec{B}$ drift and bounce motion.

2.2 Adiabatic invariants of motion

For charged particles in a symmetrical dipole magnetic field, there are three adiabatic invariants of motion, that is, one adiabatic invariant for each periodic motion that the charged particles may experience. Adiabatic invariants are not absolute invariants like total energy or total momentum but, during conditions where system variables

change slowly enough, adiabatic invariants remain constant to a very high degree of accuracy. Adiabatic invariants are very useful in studying plasma motions in the space environment; for example, they aid in the understanding of adiabatic heating and the mechanics of bounce motion [*Baumjohann and Treumann*, 1996].

The general theory of an adiabatic invariant is that the action integral

$$J_i = \oint p_i dq_i, \tag{2.21}$$

where q is the coordinate in which the periodic motion takes place and p is the momentum in q, remains constant [*Wolf*, 1995]. One can derive the adiabatic invariants by applying this equation with the three periodic motions of charged particles in a symmetrical dipole field, namely the gyromotion, the parallel bounce motion and the curvature-gradient drift motion around the Earth.

The first adiabatic invariant is related to the gyromotion of a particle around a magnetic field line. Substituting the momentum of the particle perpendicular to the magnetic field into Equation 2.21, and integrating over one period of gyration, one finds,

$$J_1 = \oint m v_\perp ds = \int_{\theta=0}^{2\pi} m v_\perp r_g d\theta = \frac{\frac{1}{2} m v_\perp^2}{B} \frac{4\pi m}{q} = \text{constant}. \tag{2.22}$$

The term

$$\mu = \frac{\frac{1}{2} m v_\perp^2}{B} = \frac{K_\perp}{B} = \text{constant} \tag{2.23}$$

is the first adiabatic invariant. It is also known as the magnetic moment, as it is equal to the current of the particle moving as a ring current about the magnetic field multiplied by the area enclosed by the loop.

The first adiabatic invariant is sometimes written in terms of the magnetic flux, Φ_μ, enclosed by the gyrating charged particle. In the general case, the magnetic flux passing through an area made up of differential area elements $\vec{da}$ is defined by

$$\Phi \equiv \int \vec{B} \cdot \vec{da}. \tag{2.24}$$

For a gyrating charged particle, Φ_μ can be written as

$$\Phi_\mu = B\pi r_g^2 = B\pi \left(\frac{mv}{qB} \right)^2 = \frac{2\pi m}{q^2} \mu = \text{constant}. \tag{2.25}$$

Conceptually, this illustrates that as the magnetic field strength changes slowly, r_g will change to keep the total magnetic flux through the loop constant [*Baumjohann and Treumann*, 1996].

The periodic bounce motion leads to the second adiabatic invariant, called the longitudinal invariant. Substituting the momentum of the particle directed along the magnetic field line into Equation 2.21 and integrating over one complete bounce results in

$$J_2 = \oint m v_\parallel ds_\parallel = 2ml\langle v_\parallel \rangle = \text{constant}, \tag{2.26}$$

where $ds_\parallel$ is the incremental length along the magnetic field line, l is the length of the field line between the mirror points and $\langle v_\parallel \rangle$ is the average parallel velocity along the field line between the mirror points [*Baumjohann and Treumann*, 1996].

The third adiabatic invariant can be derived from Equation 2.21 by integrating over the path of the particle as it completes a full orbit around the Earth due to the curvature-gradient drift. *Hess* [1968] has shown that by doing so, the third adiabatic invariant is equal to the magnetic flux encircled in the particle orbit given by,

$$J_3 = \Phi_M = \oint_{\text{orbit}} \vec{B} \cdot \vec{da} = \text{constant}, \tag{2.27}$$

where the integration is a surface integral over the entire area enclosed by the orbit of the particle.

The first adiabatic invariant can be used to aid the explanation of the process of mirroring. As a charged particle travels along the magnetic field line toward one of the magnetic poles, where B is increasing, the perpendicular energy of the particle must increase to conserve the invariant. Since a magnetic field does no work on the particle, conservation of energy implies that as the perpendicular energy increases, the parallel energy decreases. This continues until, at the mirror point, the parallel energy of the particle is completely converted to perpendicular energy, and the particle reverses directions and travels back up the field line until it reaches the mirror point in the opposite hemisphere. In a perfect dipole field and in the absence of particle-particle collisions or particle-wave interactions that cause pitch angle scattering, this bounce motion would continue indefinitely.

The first and second adiabatic invariants can be used to estimate the energy gained by charged particles drifting across magnetic field lines. Consider the simple motion of an ion along the equatorial plane from an outer field line, L_1, to an inner field line, L_2, while assuming a dipole magnetic field configuration given by

$$\vec{B} = \frac{B_{es}a^3}{r^3}[-2\sin\theta\hat{r} + \cos\theta\hat{\theta}], \tag{2.28}$$

where B_{es} is the magnetic field at the surface of the Earth, a is the radius of the Earth, and r and θ are the radial distance and latitude. The magnetic field at the equatorial plane is

$$\vec{B_0} = \frac{B_{es}}{L^3}\hat{\theta}, \tag{2.29}$$

where L is the distance to the field line along the equatorial plane in units of Earth radii; the L-value is used to label a field line.

From the first adiabatic invariant, Equation 2.23, the ratio of the perpendicular kinetic energy of the particle to the magnetic field strength must remain constant in moving adiabatically from position 1 to 2. Therefore,

$$\frac{K_{\perp 2}}{B_2} = \frac{K_{\perp 1}}{B_1}. \tag{2.30}$$

Using Equation 2.29 to write the magnetic field values at points 1 and 2 in terms of the L-value, one finds

$$K_{\perp 2} = K_{\perp 1}\left(\frac{L_1}{L_2}\right)^3, \tag{2.31}$$

that is, the perpendicular energy increases inversely with the cube of the L-value.

If the movement of the particle from an outer to an inner field line is slow compared to the bounce-period, the second adiabatic invariant can be used to determine the gain in the parallel energy of the particle. By squaring Equation 2.26 one finds

$$4m^2\langle v_\parallel\rangle^2 l^2 = 8m\langle K_\parallel\rangle l^2 = \text{constant}, \tag{2.32}$$

that is, the mean parallel energy of the particle multiplied by the square of the length of the field line between mirror points remains constant. Therefore, the parallel energy of the particle at point 2 is given by

$$\langle K_{\parallel 2}\rangle = \langle K_{\parallel 1}\rangle\left(\frac{l_1}{l_2}\right)^2, \tag{2.33}$$

which illustrates that the parallel energy is inversely proportional to the square of the length of the field line. The increase in parallel and perpendicular energy demonstrated by Equations 2.31 and 2.33 is commonly known as adiabatic heating.

The adiabatic invariants are constant only when the magnetic field changes slowly in comparison to the time scale of the periodic motion. The drift invariant is the invariant most easily violated as the drift period has the longest time scale of the three periodic motions of charged particles in a dipole magnetic field. In fact, the drift invariant is valid only for very high-energy (>1 MeV) ring current ions and electrons, at which energies the drift period is on the order of 10 minutes or less. Normal bounce times for suprathermal ions are much longer than the time scales of magnetospheric parameters (such as the electric field), particularly during magnetically disturbed periods. As a result, the second adiabatic invariant is not conserved. The period of gyration has the shortest time scale out of the three periodic motions and therefore, the first adiabatic invariant is the most difficult to violate. For example, the period of gyration of oxygen ions located at the equatorial plane on L = 6 is only ∼7 seconds and is independent of particle energy. The first adiabatic invariant is the only invariant valid for suprathermal ions and thus the most important for the present work.

2.3 Plasma convection

The IMF is continually streaming past the Earth. As it does, the magnetic and particle pressures cause a compression of the quasi-dipolar magnetic field of the Earth on the dayside and an elongation of the magnetotail. When the IMF is directed northward, the result is a "draping" of the IMF over and around the Earth. When the IMF turns southward, such as illustrated in Figure 1.1, the northward directed magnetic field lines of the Earth on the dayside begin to merge with the southward IMF. The newly connected field lines are dragged antisunward by the solar wind into the magnetotail where the open field lines subsequently reconnect and become closed, thereby forming extremely stretched dipole field lines. Observations have

indicated that reconnection can take place in the distant tail (>100 R_E) or in the near tail (20-30 R_E) [*Nishida*, 1990]. In fact, very recent results suggest that the near-Earth reconnection may occur as close as 7 R_E [*Miyashita et al.*, 2005].

The newly reconnected field lines in the tail convect sunward towards the Earth and return to the dayside around both the dawn and dusk sides. These field lines can be thought of as flux tubes to which the plasma, to a first approximation, is magnetically bound or "frozen", so the flux tubes and plasma convect together at the $\vec{E}\times\vec{B}$ drift velocity. These flux tubes map throughout the magnetosphere and to the ionosphere. The footprints of this convection can be observed at low altitudes by satellites or radars capable of measuring the electric field or the drift speed of the plasma. The ionospheric footprint of the flux tubes convecting antisunward across the polar cap, reconnecting in the tail, and returning around the dawn and dusk side of the Earth at lower latitudes is known as the "two-cell" convection pattern. Looking downward onto the northern high-latitude ionosphere, the dusk convection cell flows clockwise while the dawn or morning cell convects counter-clockwise.

Figure 2.2 is an example of the two-cell convection pattern. This convection pattern is an empirical model of the electrostatic equipotential contours (equivalently, convection velocity streamlines) based on electric field measurements from numerous passes of the Dynamics Explorer 2 satellite [*Heppner and Maynard*, 1987]. The Sun is toward the top of the figure, dawn is to the right and dusk is to the left. The streamlines pointing from the top to the bottom of the figure demonstrate antisunward flow over the polar cap. At lower latitudes, the plasma flow returns to the dayside with westward convective drift in the afternoon sector and eastward drift in the morning sector.

In space physics, measuring the plasma convection at low altitudes is one tool for monitoring the dynamics of the magnetosphere. For this thesis, an understanding of low altitude convection is required for accurate analysis of the ion transport in the magnetosphere. Chapter 3 presents observations of plasma convection at subauroral latitudes. These results provide insight into the overall convection patterns during magnetically disturbed conditions because the convection streamlines in the subau-

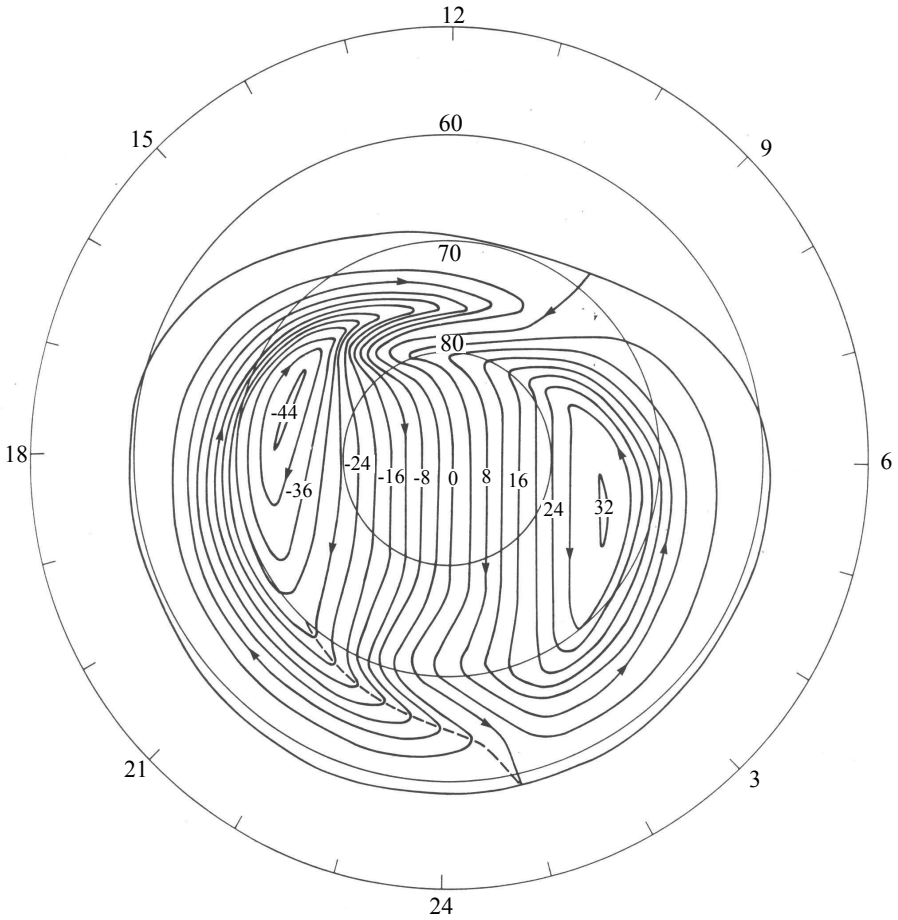

Figure 2.2: Electric potentials based on the electric field model A of *Heppner and Maynard* [1987] representing distributions encountered in the northern hemisphere under -BY IMF conditions. Contours spaced at 4 kV interval for $3^+ \leq Kp \leq 4^-$. From *Heppner and Maynard* [1987].

roral region are part of the two-cell pattern and are intimately related to the activity in the auroral zone and polar cap regions.

Chapter 3

Subauroral polarization stream

During magnetically disturbed periods, energetic ions and electrons are injected into the plasma sheet as a result of reconnection in the magnetotail. In the plasma sheet, the dawn-dusk electric field causes these particles to $\vec{E}\times\vec{B}$ drift sunward [*Wolf*, 1995], while the curvature gradient drift causes ions to drift westward and electrons eastward around the Earth as they bounce along the magnetic field between hemispheres.

As the particles bounce external influences, such as particle-wave interactions, can cause a change of the particle pitch-angle, known as pitch-angle diffusion. If the perpendicular energy is transferred from the particles to waves such as ion cyclotron or whistler waves, the pitch-angle decreases, which causes the mirror point to move to lower altitudes. If this causes the mirror point to drop into the lower ionosphere, the particles are likely to be lost due to collisions with neutrals.

Southwood and Wolf [1978] showed that the minimum lifetime for pitch-angle diffusion is proportional to the square root of the particle mass. This implies that the electrons will scatter due to pitch-angle diffusion much more quickly, and hence suffer greater loss rates than the ions. As a result, if electrons and ions are both convecting earthward in the plasma sheet due to the dawn-to-dusk electric field, the ions will remain bouncing long enough to penetrate to distances radially closer to the Earth. This charge separation creates a polarization electric field radially outward in the equatorial plane of the magnetosphere which maps down to a poleward-directed field in the ionosphere. It is this electric field that drives strong westward plasma flows on the nightside at subauroral regions during strongly magnetically disturbed periods, first observed by *Galperin et al.* [1974]. This strong westward flow was orig-

inally called a polarization jet but similar structures have been documented in the literature and termed subauroral ion drifts (SAIDs) [*Spiro et al.*, 1979] or penetration electric fields [*Rowland and Wygant*, 1998]. In 2002, *Foster and Burke* [2002] proposed the term Sub-Auroral Polarization Stream (SAPS) to replace the older terms, particularly because the radar observations indicated that the SAPS region could extend over a much larger latitudinal ($\sim 5°$) width than the polarization jet or SAID region ($\sim 1°$).

SAPS convection can extend from dusk into the postmidnight sector ($\sim$ 18 to 04 magnetic local time (MLT)). In the postmidnight sector, it can be clearly distinguished as a westward flow equatorward of the eastward auroral zone flow. Prior to midnight, both the auroral zone flow and the SAPS flow are westward but the SAPS can be distinguished by a distinct velocity increase in the equatorward portion of the velocity profile [*Foster and Burke*, 2002]. The most distinguishing feature of the SAPS region, however, is the precipitation of only low-energy primary ions, as opposed to the auroral energy ions that precipitate into the auroral zone. This is discussed further with respect to satellite particle measurements in Chapter 5.

3.1 SAPS characteristics

Foster and Vo [2002] presented the characteristics of the SAPS region using the Millstone Hill incoherent scatter radar. This radar is situated at 54° invariant latitude (ILAT) and scans more than 30° of latitude and 4 hours of local time at F-region heights. *Foster and Vo* [2002] analyzed 9800 scans measured over 22 years to determine the occurrence and properties of the SAPS convection peak. The existence of SAPS was characterized by its strong westward component of flow velocity as a function of ILAT.

The SAPS flows occur mainly during periods of high geomagnetic activity, particularly in the postmidnight sector. A measure of the geomagnetic activity is the Kp index, which is described in more detail in Appendix A.1. As the Kp index increases, the latitudinal separation between the peak of the SAPS flow and the location of the

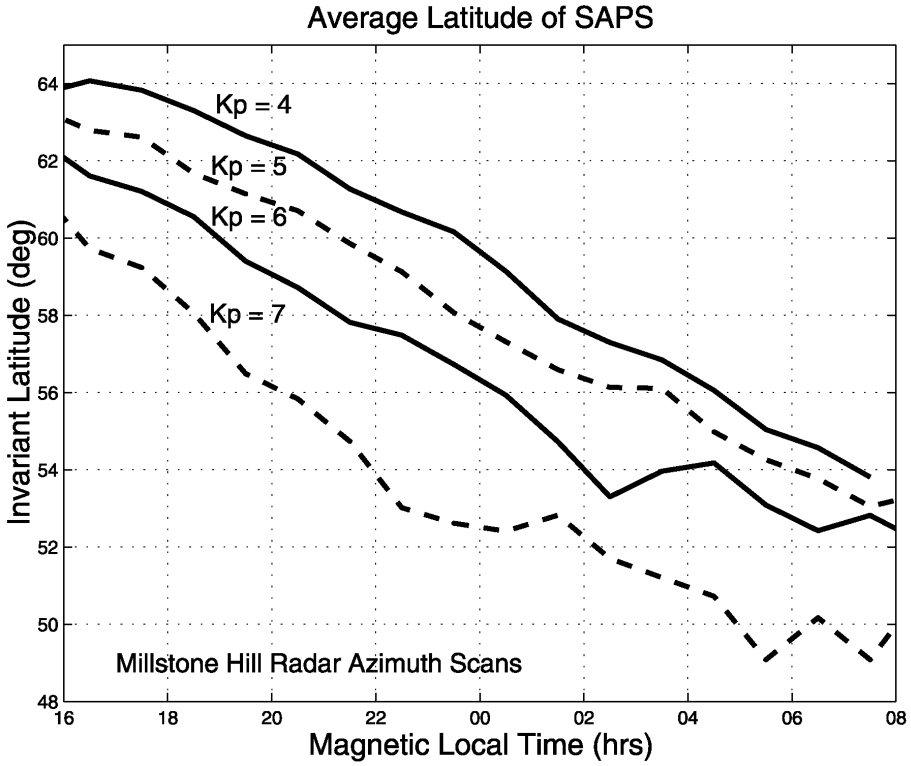

Figure 3.1: Average latitude of the peak of the SAPS decreasing as a function of both MLT and increasing Kp index. From *Foster and Vo* [2002].

peak auroral region flow increases [*Rowland and Wygant*, 1998]. In Figure 3.1 the average latitude of the SAPS peak flow is plotted as a function of invariant latitude and magnetic local time for Kp indices from 4^0 to 7^0 [*Foster and Vo*, 2002]. This figure illustrates that the latitude of the maximum flow speed increases as the plasma drifts westward from the postmidnight sector to the premidnight sector.

Figure 3.2 shows the average ion velocity, assuming a westward flow along shells of constant magnetic field strength, or L shells. This is a reasonable approximation for flows that are aligned within 25° of the L shell direction, for which the error is less than 10%. The plot includes all scans for Kp indices ranging from 5^+ to 6^0, adjusted so that the peak of each individual scan overlapped the average peak latitude. The curve for Kp 6^- shows that, around 16 MLT, the SAPS is observed at invariant latitude 62°, about 4° equatorward of the peak in the auroral zone convection. At

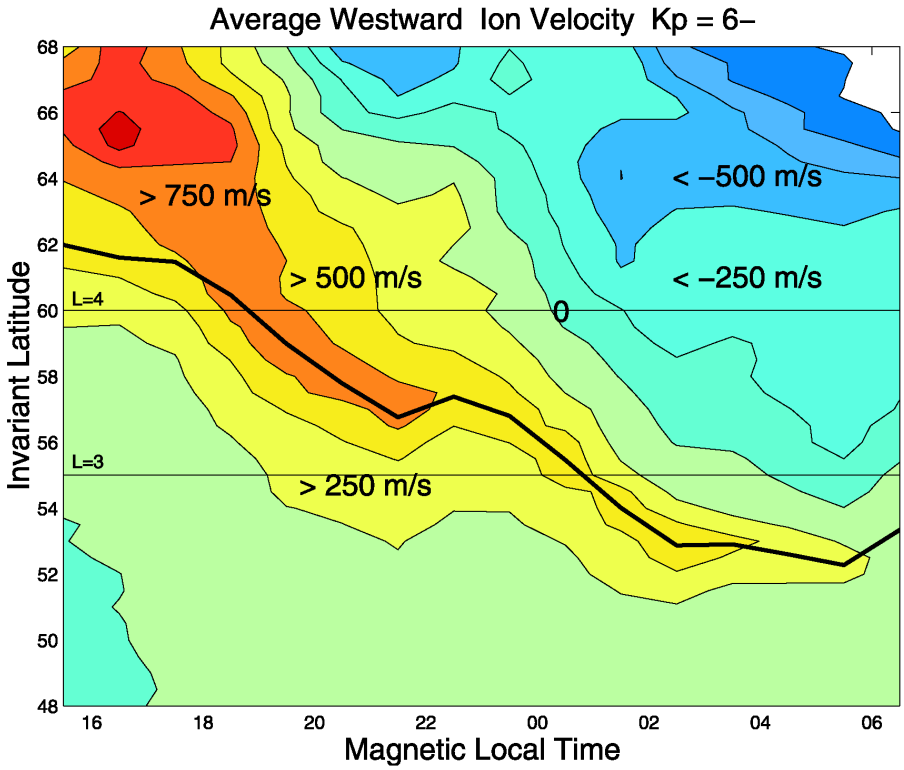

Figure 3.2: Averaged westward ion velocity from scans with $Kp[5^+,6]$ for which SAPS have been identified. The bold black curve indicates the average SAPS peak position. From *Foster and Vo* [2002].

20 MLT the Kp 6^- SAPS peak is located at about 58°. The latitude of this peak continues to decrease with increasing MLT, reaching 53° at 04 MLT. Figure 3.2 also characterizes the latitudinal width of SAPS for this specific range of Kp. This width decreases as the MLT shifts from premidnight to the postmidnight sector.

Figure 3.3 shows a contour plot of the percent occurrence of SAPS for all of the 9800 scans as a function of Kp and magnetic local time. As the magnetic activity increases, the probability of observing SAPS also increases. The probability of occurrence exceeds 50% at 02 MLT and 30% at 04 MLT for Kp greater that 5^+. Such high probabilities of occurrence indicate that SAPS is an important feature of the nightside convection during disturbed periods.

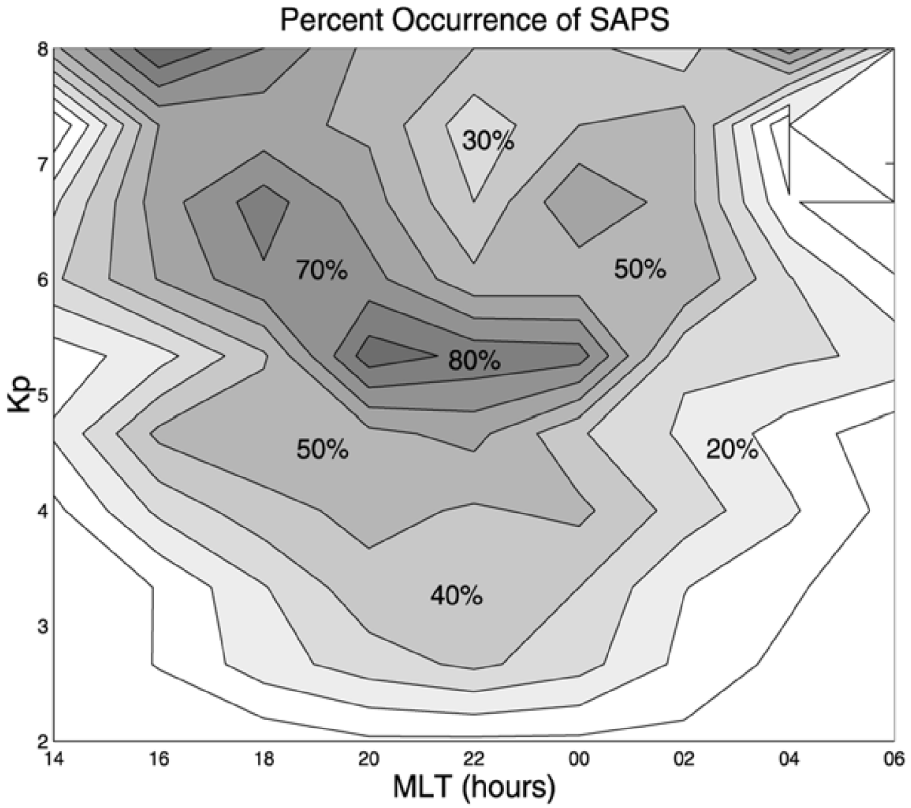

Figure 3.3: Occurrence probability for SAPS as observed by Millstone Hill. From *Foster and Vo* [2002].

3.2 Implication of SAPS on global electrostatic potential

The standard two-cell convection models such as the empirical models of *Heppner and Maynard* [1987] provide reasonable time-averaged convection maps for the high-latitude auroral region. However, the standard two-cell convection is an incomplete picture of the magnetospheric convection as it does not address SAPS, which persist during more magnetically disturbed periods. Using the results of the statistical study by *Foster and Vo* [2002] a more complete picture may be proposed.

Two important conclusions can be drawn from observations of SAPS to aid in deducing the full two-cell convection model. First, the westward flow peak of SAPS can extend well into the postmidnight sector to 04 MLT, after which the flow weakens.

Also, the latitude of the SAPS peak velocity decreases from the afternoon sector to the postmidnight sector. Figure 3.4 illustrates one possible interpretation of distorted flow contours associated with SAPS characteristics [*Sofko et al.*, 2007]. The heavy dashed line indicates the boundary between the auroral and the subauroral regions. The solid line connecting the dotted line indicates the approximate location of the open-closed field line boundary.

This illustration accounts for the latitudinally broad westward SAPS region as the elongated extension of the afternoon convection cell. Some streamlines travelling anti-sunward over the polar cap first turn eastward in the low-latitude part of the auroral oval and then reverse direction and return westward in the plasmatrough. As these convection streamlines are the ionospheric footprints of magnetospheric flux tubes, this illustration can be interpreted in terms of the magnetospheric convection. The open field lines in the polar cap are tied to the solar wind and convect antisunward where they reconnect in the stretched tail. As these flux tubes convect earthward, many flow west or east in the typical two-cell convection at auroral latitudes. Some, however can penetrate deeper into the plasmatrough region where the SAPS flow is located.

This interpretation is consistent with the observational results presented at the *Workshop on Penetration Electric Fields and Their Effects in the Inner Magnetosphere and Ionosphere* in September, 2005 [*Foster and Coster*, 2007]. It is also consistent with the analytical model presented by *Lyatsky et al.* [2006].

The extension of the auroral two-cell convection into the subauroral region has implications for the transport of ionospheric plasma into the inner magnetosphere. During disturbed periods, auroral precipitation occurs over a broad latitudinal and longitudinal band called the auroral oval. This precipitation, as described in Section 1.4, creates a substantial secondary ionospheric plasma population by primary auroral particle bombardment, which, in the presence of sufficient acceleration, can lead to a distribution of ions with suprathermal energies called APS. Suprathermal ions are of sufficiently low energy that they are primarily confined to the flux tubes that $\vec{E}\times\vec{B}$ drift along the convection streamlines. Figure 3.4 illustrates that the

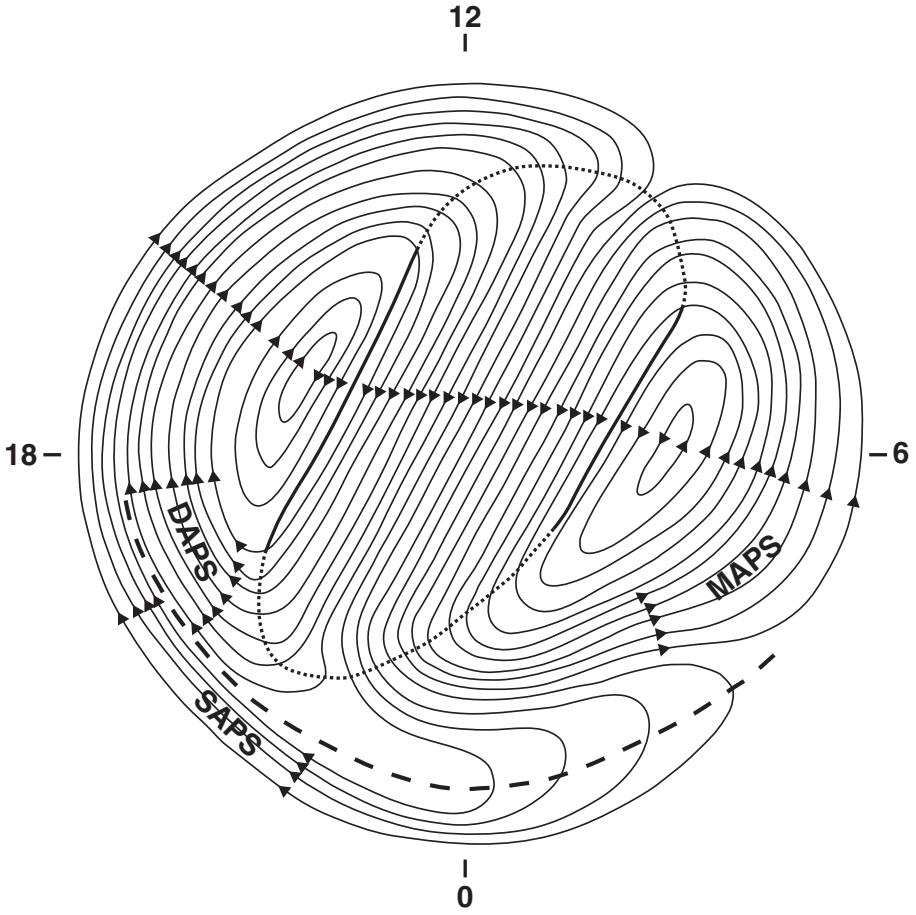

Figure 3.4: Schematic illustration of the two-cell convection pattern including the SAPS convection. The thin solid line connecting the dotted line over the polar cap indicates the open-closed field line boundary. The heavy dashed line approximates the boundary between the auroral and subauroral regions. Adapted from *Sofko et al.* [2007].

convection during magnetically disturbed conditions can transport these suprathermal APS ions westward or eastward from the midnight auroral oval region along the typical auroral zone convection. The convection can also drive APS ions equatorward of the auroral precipitation boundary into the SAPS region. *Sofko et al.* [2007] has classified the APS ions into the three categories based on the region where the APS ions convect into. These three categories are morning, dusk, or subauroral APS (MAPS, DAPS, and SAPS), and are labelled in Figure 3.4.

3.3 A hypothesis for the time delay between magnetic substorm onset and radar observations of SAPS-like flows

Koustov et al. [2006] presented a statistical study of observations of SAPS-like flows made with the King Salmon SuperDARN radar. The SuperDARN radars are a network of 19 (12 northern hemisphere and 7 southern hemisphere) coherent scatter HF radars which measure the $\vec{E}\times\vec{B}$ drift in the ionosphere [*Greenwald et al.*, 1995]. In their paper, an event on December 5, 2001, was examined in detail and a plot of the maximum plasma velocity measured as a function of the radar range was provided for a time period extending from 30 minutes prior to substorm onset to two hours after. During the event, the SuperDARN plasma convection velocity started to increase at substorm onset and continued to increase until a peak was reached roughly 20 minutes later.

Koustov et al. [2006] also presented data which showed that a large region of ionospheric echoes developed at the time when the strongest convection speeds were observed. The enhancement in the number of radar echoes persisted for ∼35 minutes. Similar increases in the number of radar echoes were noted in two other events from this study (R. Drayton, private communication) with time delays of 35 and 50 minutes from substorm onset. Such increases in the SuperDARN backscatter occurrence within the SAPS region are consistent with observations of the SAPS flow made with the Wallops Island SuperDARN radar [*Oksavik et al.*, 2006].

Enhancement in the number of radar echoes within the SAPS region may in part be explained by the theory that, during periods of active auroral precipitation such as at substorm onset [*Akasofu*, 1964], clusters of suprathermal ions are generated within the auroral zone. As the clusters travel along the magnetic field lines, the $\vec{E}\times\vec{B}$ drift drives the flux tubes, on which the ions are bouncing, equatorward into the SAPS region. Upon precipitating back into the ionosphere the ionization altitude of ions of suprathermal energies is within the F region. For example, the ionization

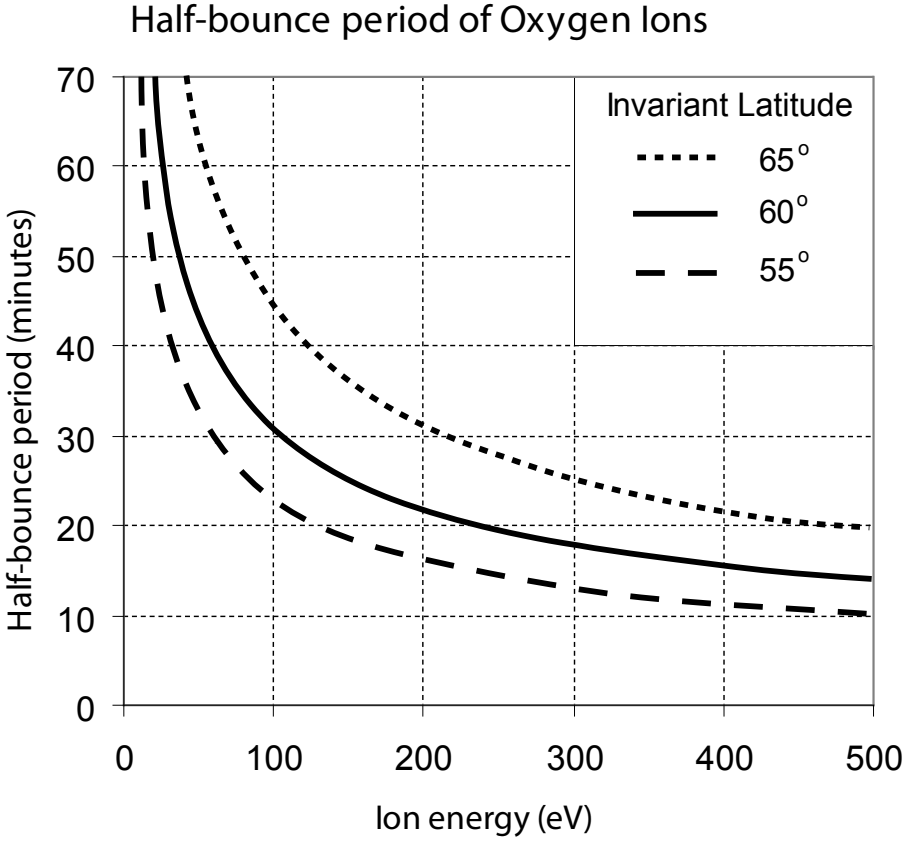

Figure 3.5: Half-bounce period of O^+ ions travelling on magnetic field lines with an invariant latitude of 55°, 60°, and 65°.

altitude of ions with an energy of 250 eV is located between 200–350 km, as seen in Figure 6 of *Rees* [1982]. This ion precipitation increases the amount of structure at the altitude range that the SuperDARN radars are designed to observe coherent echoes.

To illustrate further, Figure 3.5 provides the half-bounce period of O^+ ions for an energy range of 0 to 500 eV, assuming the ion bounce motion occurs on dipole magnetic field lines with invariant latitudes (ILAT) of 55°, 60° and 65°. This plot illustrates that the half-bounce period for the majority of ions in the energy range that is classified as suprathermal can be confined to a time range of 10–50 minutes. This time duration matches well with the observed time delay between onset and the increase in the number of radar echoes observed in *Koustov et al.* [2006].

One must note that, during a half-bounce period of 10 to 50 minutes, the ions may drift a significant distance due to the high velocity SAPS (or SAPS-like) flows. This implies that the region in which the APS ions precipitate back into the ionosphere and contribute to the increased number of radar echoes may be located westward of the location of the enhanced auroral activity that generated the APS ions. To provide an understanding of the magnitude of this drift, the change in longitude that the plasma drifts while experiencing a westward $\vec{E}\times\vec{B}$ drift for time periods of 10, 30 and 50 minutes was calculated and is illustrated in panels a), b), and c) of Figure 3.6. It is assumed that the ions initiated their drift-bounce motion at 24 MLT. The westward and eastward sides of the shaded areas indicate the distance travelled while assuming a westward ionospheric $\vec{E}\times\vec{B}$ drift of 1000 m/s and 500 m/s, respectively. This diagram illustrates that westward $\vec{E}\times\vec{B}$ drifts of 500 to 1000 m/s are capable of transporting ions roughly 1 to 3 hours of magnetic local time in the time required for O^+ ions to complete a single half-bounce. If one assumes that the acceleration of these ions takes place around the convection reversal region in Figure 3.4, it is clear that typical SAPS convection are capable of transporting APS ions equatorward of the auroral zone, into the SAPS region during their first half-bounce.

The following chapter examines satellite observations of suprathermal ions within the magnetospheric region which maps to the low-latitude portion of the auroral oval. Evidence suggests that these ions are ionospheric ions which have been accelerated to suprathermal energies. Spectrogram observations show that there are bands of enhanced ion flux whose energy increases with increasing latitude. Possible mechanisms to explain this energy dispersion are examined in detail and a hypothesis is presented.

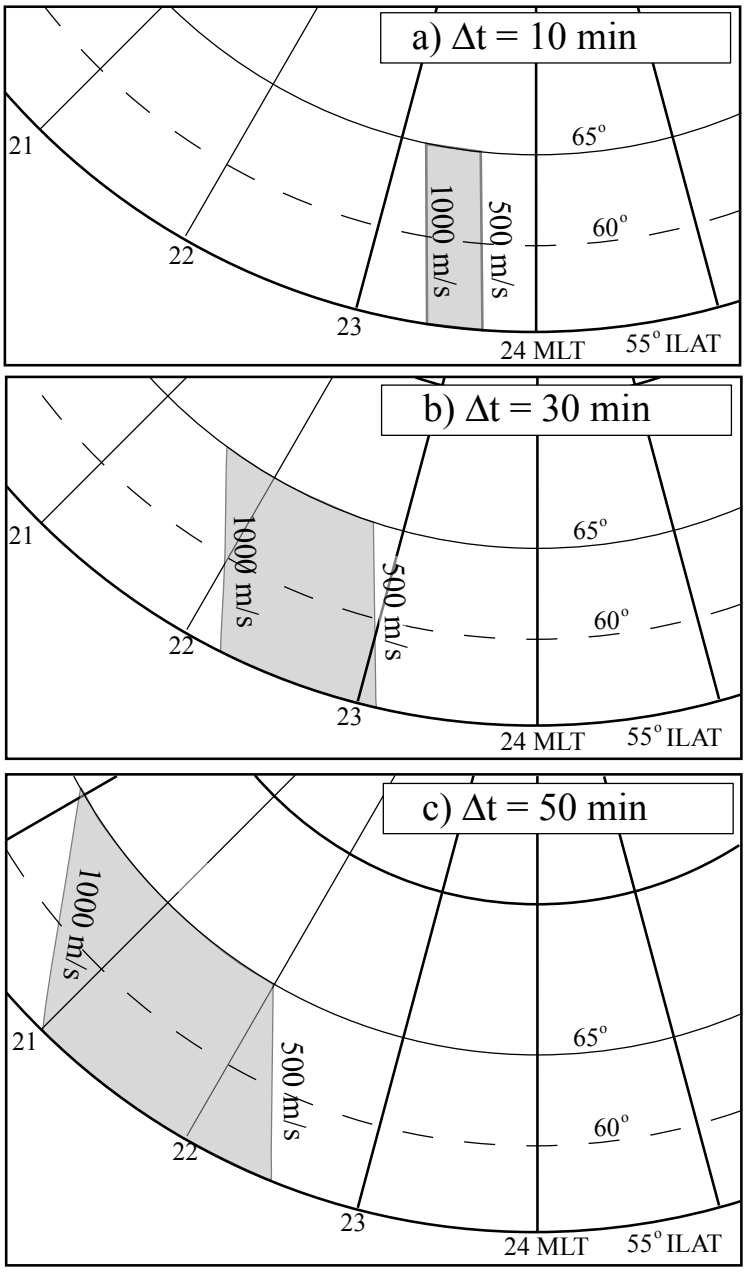

Figure 3.6: The longitudinal drift distance from 24 MLT after 10, 30 and 50 minutes in a mean westward $\vec{E}\times\vec{B}$ drift of 500 m/s and 1000 m/s.

Chapter 4

Energy-dispersed ion signatures

Particle spectrometers onboard satellites and rockets have allowed researchers to make in-situ observations of the flux, energy and pitch angle of ions and electrons. These observations have revealed flux enhancements displaying a relatively smooth change in energy as a function of time and/or space. Studies of the various types of energy-dispersed signatures contribute to the understanding of magnetospheric processes such as acceleration and drift mechanisms (e.g., *Hirahara et al.* [1997a]). The following section describes two energy dispersion mechanisms and presents published examples for each. Section 4.2 focusses on the observations of energy-dispersed signatures in the region mapping to the low-latitude portion of the auroral oval. A review of the hypotheses advanced to explain these specific signatures is provided in Section 4.3. Further discussion and a description of a new hypothesis is provided in Section 4.4.

4.1 Types of energy-dispersed ion signatures

In the literature, authors often attempt to classify the type of the energy dispersion of ion structures into one of two models (e.g., *Frahm et al.* [1986]). The Time-of-Flight (TOF) dispersion, proposed by *Quinn and McIlwain* [1979], has historically been used to explain the energy dispersion from observations made from satellites and rockets primarily located along a constant L shell. A second model called convective dispersion attempts to explain the ion energy dispersion measured by low-altitude satellites that cross high to mid-latitude regions on a time scale short in comparison to the bounce period of ions [*Frahm et al.*, 1986].

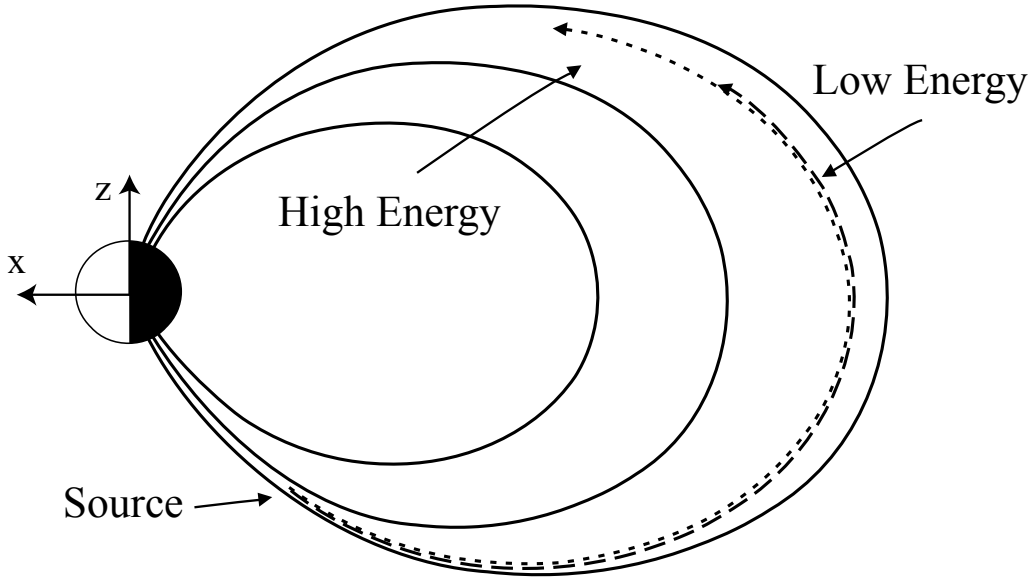

Figure 4.1: Illustration of the time-of-flight effect on a cluster of ions accelerated from the southern hemisphere in a latitudinally confined region. High energy ions (dotted line) pass the low energy ions (dashed line) as they drift along the magnetic field line. Adapted from *Frahm et al.* [1986].

A schematic illustration of the TOF effect is presented in Figure 4.1. In this model, a localized ion source is located on the same field line as the observer and is assumed to have a broad energy and pitch angle distribution. The acceleration of the ions is assumed to occur over a short time scale compared to the bounce times of the ions. After undergoing this acceleration, a cluster of ions bounce along the field line. An observer who is positioned some distance from the source along the field line and who is viewing ions in a discrete pitch angle range will detect the ions with the highest energies (velocities) first. Lower energy ions take a longer time to reach the observer. Effectively, the TOF effect is due to the velocity-dependent bounce period of ions and the energy dispersion is observed as a decrease in energy with an increase in time.

Quinn and McIlwain [1979] published some of the earliest observations of ion energy dispersion believed to be primarily due to the TOF effect. These observations from the Applications Technology Satellites ATS-5 and ATS-6 (geosynchronous

orbit) showed bands of enhanced ion flux in the energy range from 10 to 1000 eV, with the energy decreasing with time. At times, these observations revealed multiple bands which appeared to overlap, scattered throughout all magnetic local times. To explain this, *Quinn and Southwood* [1982] proposed that a dipolarization of the magnetic field near the equatorial plane had energized a cluster of ions. These ion clusters were subsequently dispersed in energy as they travelled along the magnetic field, with the lower energy ions lagging the higher energy ions. The energy range of the particles was sufficiently broad that, by the time the lowest energy particles reached the observing satellite, some higher energy particles had travelled the same path plus a full bounce and were observed simultaneously. A more detailed explanation of the concept of ions making multiple bounces or half-bounces is given in Section 4.3.

In the convective dispersion model, the ions are accelerated out of a source region with the same broad energy and pitch angle distribution that is assumed for the TOF model. However, the acceleration is assumed to be more sustained in time than the short-lived acceleration which is sufficient for the TOF model. It is assumed that, during the bounce motion, there is $\vec{E}\times\vec{B}$ drift, in which case the component of $\vec{E}$ perpendicular to the magnetic meridian plane is capable of driving the plasma to different L shells. Figure 4.2 illustrates the paths of high and low energy ions from a source in the southern hemisphere as ions undergo their bounce motion near the noon-midnight meridian plain in the presence of the dawn-to-dusk electric field ($\vec{E}\times\vec{B}$ drift directed toward lower L shells). The high energy ions drift only a small distance toward lower L shells in one half-bounce. The low energy ions also experience the $\vec{E}\times\vec{B}$ drift during their much longer half-bounce period, and they reach their mirror points at latitudes equatorward of the high energy ions. Thus, the ion energy decreases as the L-value and the magnetic latitude decrease. For the case illustrated in Figure 4.2, the latitudinal energy dispersion occurs in the noon-midnight meridional plane. Note that the assumption that the high-energy ions precipitating at higher magnetic latitudes are observable at the same time and altitude as the low-energy ions precipitating at lower magnetic latitudes directly

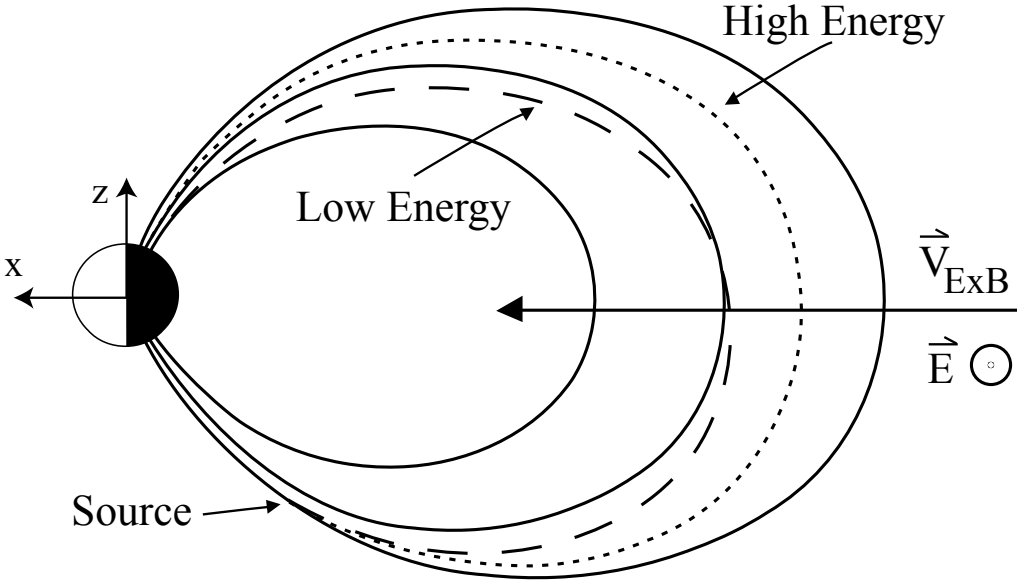

Figure 4.2: Illustration of the effect of convective dispersion on a cluster of ions accelerated out of the southern hemisphere from a latitudinally confined source region. Low energy ions that have a lower parallel velocity spend a longer time traveling from the injection region to the mirror point. Due to inward $\vec{E}\times\vec{B}$ drift which is independent of energy, they drift to lower latitudes than the high energy ions. Adapted from *Winningham et al.* [1984].

implies that the acceleration of the ions must have taken place for at least the time difference between the half-bounce period of the high and low energy ions.

Although Figure 4.2 illustrates the concept of convective dispersion occurring in the nightside magnetosphere, the idea of convective dispersion originated with plasma observations in the polar mantle in the dayside magnetosphere made by the Heos 2 satellite. Heos 2 was launched into an eccentric, polar orbit with an initial apogee of 2.4×10^8 km ($\sim$37.7 R_E) and a perigee of 409 km [*Rosenbauer et al.*, 1975]. In theory, magnetic merging on the dayside magnetopause accelerates and injects ions into and out of the cusp region. A poleward $\vec{E}\times\vec{B}$ drift drives the plasma toward higher latitudes on the recently opened field lines. Because the lower energy ions take a longer time to travel from the reconnection altitude to their mirror points, they will precipitate or bounce at higher latitudes than high energy ions. This is

the same as the convective dispersion illustrated in Figure 4.2 but with opposite sign (i.e., energy decreasing with increasing latitude poleward of the cusp). Early evidence of convective dispersion in the low-altitude projection of the cusp was provided by observations from the LEO satellites 1971-089A [*Shelley et al.*, 1976], Atmospheric Explorer C (AE-C) [*Reiff et al.*, 1977], and Dynamics Explorer satellites DE-1 and DE-2 [*Burch et al.*, 1982].

To clarify the difference between the TOF and convective dispersion models, consider the ideal convective dispersion situation where there is a continuous source of ions undergoing combined drift and bounce motion under the influence of an $\vec{E}\times\vec{B}$ drift directed earthward in the magnetosphere, which maps to an equatorward drift in the ionosphere. Since the $\vec{E}\times\vec{B}$ drift disperses the ions spatially in latitude as a function of the ion energy, the dispersion is seen as an increase (decrease) in energy with an increase (decrease) in latitude. An observer located at a fixed latitude would not observe the ion energy decrease in time but instead would see a flux of ions with a constant energy. This is contrary to the TOF situation where the ion injection is short-lived and only the bounce motion occurs. For this latter situation, the TOF effect dominates the energy dispersion and the energy of the incoming ions would decrease with time at a fixed latitude.

Confusion between the two models exists because in reality both effects are always present. In examples for which the TOF effect is the dominant dispersion, there is always some convective drift that could potentially cause spatial dispersion of ions. Even if the ions were accelerated over a time period that is nearly instantaneous, convective dispersion still disperses the ions spatially, but the ability of an observer travelling at a constant altitude to observe the dispersion decreases. This is because the time duration of ions crossing any given altitude is a function of the time duration of the acceleration. In the ideal convective dispersion situation the dependence of ion bounce period on the velocity, which by definition causes the TOF effect, is what allows the convection to disperse the ions spatially in latitude.

There is added difficulty in analyzing energy-dispersed ion signatures because there is no ideal instrument capable of fully detecting energy-dispersed particles. To

completely analyze an energy-dispersed ion signature, the entire spatial extent and temporal variation of the particles must be sampled. However, the primary instruments used to observe these particles are spectrographs on satellites. A satellite in a low Earth orbit (LEO) travels across a wide range of L shells quickly and can only sample precipitating ions along its trajectory. Such LEO satellite observations provide a reasonable measure of the spatial variation of ion energy but are not ideal for studying the temporal signature. Satellites in geosynchronous orbits travel relatively slowly across L shells which makes them well-suited for studying the temporal rather than the spatial signature. In general, due to the finite travel time of the satellite through the ion signatures, spatial effects cannot be absolutely distinguished from temporal effects in satellite measurements, i.e. space-time ambiguity occurs.

4.2 Energy-dispersed ion precipitation in the low-latitude portion of the auroral oval

Winningham et al. [1984] presented energy-time spectrograms from the Dynamics Explorer satellites DE-1 (∼10,000 km altitude) and DE-2 (∼1000 km), illustrating an energy-dispersed ion signature with a decrease in energy with decreasing latitude in the low-latitude auroral oval. One example from DE-2 is presented in Figure 4.3. The top and bottom panels represent the electron and ion differential energy flux (ergs/cm^2·s·sr·eV) respectively, plotted on a log energy scale (y-axis) versus time and satellite position (x-axis). The observations in Figure 4.3 are from one of the 15 electrostatic analyzers (field of view of 5° by 20°) making up the Low-Altitude Plasma Instrument, which was aligned to detect ions with a pitch angle of 15°±10° [*Winningham et al.*, 1981]. The ion panel shows two bands which decreased in energy as the satellite moved equatorward (left to right in the figure) from 61.5° to 58.1° ILAT. The authors hypothesized that the ions were accelerated from the ionosphere, travelled through the magnetosphere along the magnetic field lines and precipitated in the opposite hemisphere. The dispersion was believed to result from the nightside cross tail electric field, which created an $\vec{E}\times\vec{B}$ drift driving the lower energy ions to

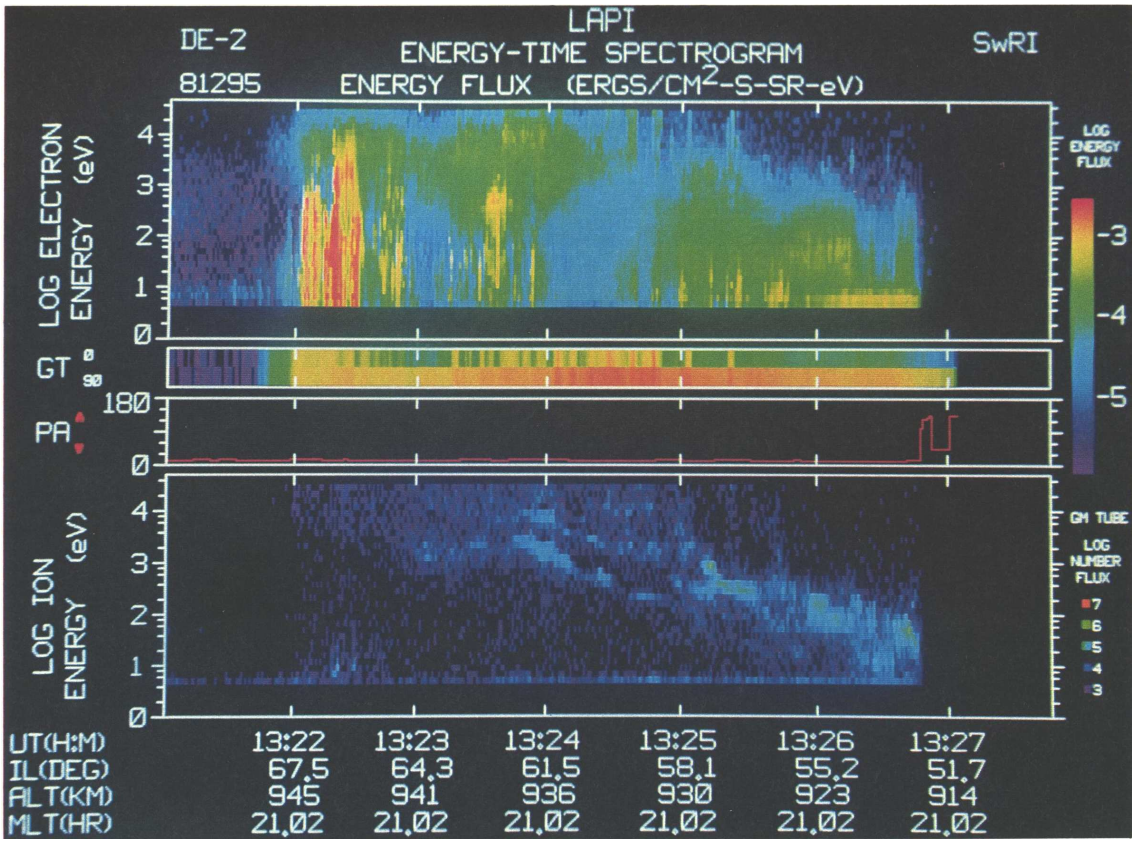

Figure 4.3: Energy-time spectrogram from the DE-2 satellite. The panel of interest is the bottom panel representing the differential energy flux (ergs/cm^2·s·sr·eV) of ions with a pitch angle of 15°. Two bands of enhanced ion flux are seen to decrease in energy as the satellite moved equatorward from 61.5° to 58.1° ILAT. From *Winningham et al.* [1984].

lower latitudes as they bounced between hemispheres. Their analysis of the energy dispersion indicated that the signatures were primarily due to O^+ ions, supporting their theory of an ionospheric ion source.

Frahm et al. [1986] presented similar DE-1 and DE-2 results and furthered the discussion of the mechanism causing the energy-dispersion. Both the TOF and the convective dispersion models were considered. It was concluded that convective dispersion was responsible for producing the measured energy-dispersed signatures. The main points presented by *Frahm et al.* [1986] in favor of the convective dispersion conclusion were that the signatures appeared stable in time, and that the increase in energy with increasing latitude was observed by the satellite for both poleward

and equatorward directed trajectories. It was argued that if the TOF effect were dominant, the ion energy would be observed to decrease with time, independent of the direction of motion of the satellite. With the aid of more recent results, both models are analyzed in more depth in Section 4.3. The analysis shows that, by considering a source of ions extended across a large range of L shells, the above argument supporting the convection dispersion model can be challenged.

4.3 Banding and dispersion of the energy-dispersed signatures in the low-latitude portion of the auroral oval

Hirahara et al. [1997a, b] presented an Akebono case-study of banded, energy-dispersed ion signatures in the low-latitude portion of the auroral oval and provided an in-depth review of the explanation for the banding and the energy dispersion. Akebono was launched into an elliptical orbit with an apogee and perigee of 10,500 km and 274 km respectively [*Oya and Tsuruda*, 1990]. A more detailed description of the Akebono satellite and the onboard instruments is provided in Appendix A.3. One of their examples, from an event on December 21, 1989, is reproduced in Figure 4.4. Panel 1 is the omnidirectional electron flux in detector counts per second plotted as a function of energy and time. Panels 2 to 5 show plots of the ion flux in detector counts per second as a function of energy and time for four pitch angle ranges in 20° increments. Panel 2 corresponds to the ion "loss cone" detector looking upward along the magnetic field line (ions with a pitch angle of 0° to 20°) and illustrates that the auroral-energy (>1 keV) ion precipitation boundary occurred near 0316 UT, at 66.4° ILAT.

Equatorward of this boundary, the flux of auroral-energy electrons ceased, as seen in Panel 1. However, in the absence of a panel dedicated to observations of only *precipitating* auroral-energy electrons (Panel 1 is the omnidirectional plot for electrons), the auroral-energy electron precipitation boundary is undefined. Panels 3, 4 and 5

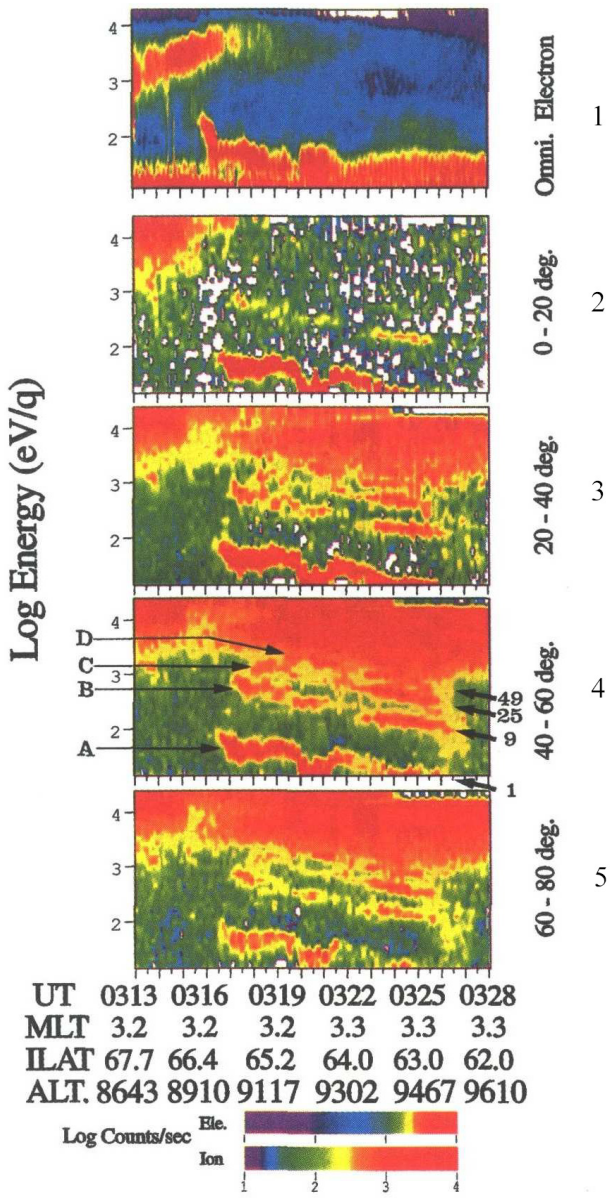

Figure 4.4: Electron and ion spectrogram taken from the Akebono satellite for an event on December 21, 1989: (1) the omnidirectional electron spectrogram, (2)–(5) the ion spectrograms sorted into four pitch angle ranges from field-aligned to perpendicular. From *Hirahara et al.* [1997a].

show the "trapped ion" fluxes. Four energy-dispersed ion bands labeled A, B, C and D in Panel 4 (pitch angles 40° to 60°) are seen extending equatorward from $\sim$ 66.0° to 63.0° ILAT with a decrease in energy with decreasing latitude. In all Akebono case studies presented by *Hirahara et al.* [1997a, b], the characteristic decrease (increase) in ion energy with decreasing (increasing) latitude was observed independently of the direction of the satellite auroral-zone crossing, and this signature was associated with the low-latitude portion of the auroral region.

In Panel 2, which corresponds to the field-aligned "loss cone" particles, the flux of the lowest energy band, Band A, is much higher than the flux of Band B. Bands C and D are not visible. However, all bands are observed in the "trapped ion" panels, Panels 3, 4 and 5. The energy ratios between the bands remain roughly constant with latitude. It is important to note that, in Panels 3 to 5, trapped, auroral-energy ions (ions with energies exceeding 1 keV) also are seen extending equatorward of the auroral ion precipitation boundary that was defined in Panel 2, across the entire latitudinal extent of the plot (down to 62.0° ILAT).

The major ion species determined with the Ion Mass Spectrometer (IMS) and the Suprathermal Mass Spectrometer (SMS) (see instrument description in Appendix A.3) was undetermined for this event. In the majority of the cases examined by *Hirahara et al.* [1997a], the dominant ion species in the low energy range ($<$ 100 eV) was O^+, with H^+ prevailing as the dominant species in the remaining events. The presence of O^+ supports the theory that these dispersed ions are generated and transported from the ionosphere where oxygen is the dominant atom above 150 km.

The study by *Hirahara et al.* [1997a] differed from the previous works by *Winningham et al.* [1984] and *Frahm et al.* [1986] because it included Akebono measurements of the electric field. The observations indicated that there was a strong longitudinal component of the $\vec{E}\times\vec{B}$ drift, which, when combined with a persistent acceleration mechanism, leads to convective dispersion aligned in the meridional direction. For an event like the example in Figure 4.4, where Akebono is located in the morning low-latitude auroral region, the equatorward component of the electric field in the

ionosphere (corresponding to the radially inward meridional electric field component in the equatorial plane in the magnetosphere) causes the ions to $\vec{E}\times\vec{B}$ drift eastward as they undergo the bounce motion along the magnetic field lines. Idealized particle trajectories are illustrated in Figure 4.5. A high-energy ion makes a half-bounce fairly quickly and drifts eastward only a relatively short distance (dotted line). A low-energy ion has a much longer half-bounce time and drifts farther eastward after making one half-bounce (solid line). The dashed lines trace the shape of the dipole field lines extending from the altitude of the source in the southern hemisphere to the mirror altitude in the northern hemisphere.

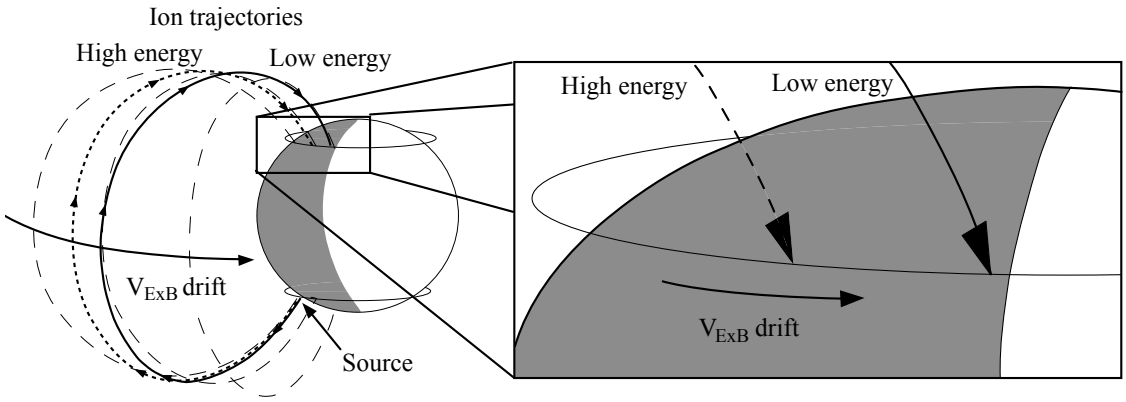

Figure 4.5: Illustration demonstrating the combined effects of parallel bounce motion along magnetic field and the $\vec{E}\times\vec{B}$ drift to the east due to an equatorward-directed electric field in the ionosphere (ion gyromotion and curvature-gradient drift are absent). The dashed lines trace the shape of the dipole field lines. The trajectories of a high and a low energy ion are illustrated by the dotted and solid lines, respectively.

To understand how the energy dispersion is observed when a satellite moves equatorward through the auroral region (perpendicular to the primary $\vec{E}\times\vec{B}$ drift), consider the postmidnight northern ionospheric convection map in Figure 4.6. This figure displays typical morning cell eastward convection (see Section 2.3) during a period of low to moderate Kp (2^+ to 3^+), such as the period during which the signatures in Figure 4.4 were observed. The black band near midnight indicates the northern-hemisphere mapping of a conjugate southern-hemisphere acceleration re-

gion, which acts as a source of ionospheric ions, located in the morning convection cell. The shaded area eastward of the source region indicates the position of the ions after travelling one half-bounce. Low-energy ions, indicated by the lighter shades, drift farther in longitude than the higher energy ions, indicated by the darker shades, during a half-bounce. Now consider the satellite track for an equatorward moving satellite (Figure 4.4). Two heavy convection lines indicate where the satellite intercepts the particles on the poleward and equatorward streamlines coming from the "injection band" near midnight. Due to the differing lengths of the drift-paths, which are the longitudinal distances between the acceleration region and the satellite track, the energy of the ions travelling along the shorter, poleward drift-path is greater than the energy of the ions travelling along the longer, equatorward drift-path. The magnitude of the energy dispersion is therefore a function of the $\vec{E}\times\vec{B}$ drift and the difference in the drift-path lengths. It is important to note that, when assuming the duration of the satellite crossing is negligible, the acceleration of the ions must have occurred over a time period at least comparable to the difference between the convective drift times (which equals the half-bounce times for those particles making a single half-bounce between the acceleration region and the observation point) of ions on the equatorward and poleward drift contours.

To explain the banded nature of the signatures, *Hirahara et al.* [1997a] proposed two mechanisms. "Type A" or "multiple-bounce" energy banding is the result of ions of one specific type (such as O^+) taking different numbers of half bounces to reach the observing satellite. The *full-bounce* time, T_{bounce}, for an ion is inversely proportional to the velocity and is given by

$$T_{\text{bounce}} = \frac{4La}{v}\int_{\theta=0}^{\theta_m}\cos\theta(1+3\sin^2\theta)^{1/2}\left[1-\sin^2\alpha_0\frac{(1+3\sin^2\theta)^{1/2}}{\cos^6\theta}\right]^{1/2}d\theta, \quad (4.1)$$

where L is the equatorial distance to the field line in increments of the radius of the Earth, a is the radius of the Earth, v is the total ion velocity, θ_m is the mirror latitude and α_0 is the particle pitch angle at the equator [*Baumjohann and Treumann*, 1996]. A full derivation of T_{bounce} is provided in Appendix B.1. *Hamlin et al.* [1961] showed that the integral in Equation 4.1 can be approximated by the expression

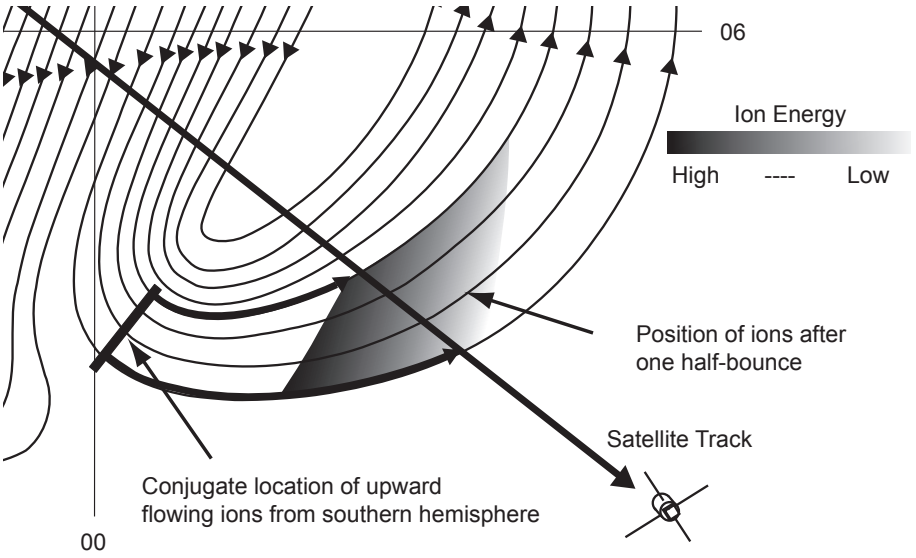

Figure 4.6: Illustration of the path ions must $\vec{E}\times\vec{B}$ drift as they travel from a southern hemisphere source (mapped to the magnetically conjugate position in the northern hemisphere) to the observing satellite track. Adapted from *Hirahara et al.* [1997a].

$1.30 - 0.56 \sin \alpha_0$, so Equation 4.1 may be rewritten as

$$T_{\text{bounce}} \simeq \frac{4La}{v}(1.30 - 0.56 \sin \alpha_0). \tag{4.2}$$

Consider the previous example where a source of ions with a broad spectrum of energies is generated in the southern hemisphere and observed in the northern hemisphere. In general, an ion must take an odd number (2n+1, for n = 0, 1, 2, ...) of *half-bounces* to travel from a southern hemisphere source to be observed by a northern hemisphere observer. The time required is thus

$$\Delta t = (2n+1)T_{hb_n} = (2n+1)[\frac{2La}{v_n}(1.30 - 0.56 \sin \alpha_0)]. \tag{4.3}$$

By replacing the velocity by $\sqrt{\frac{2E}{m}}$, where E and m are the particle energy and mass respectively, the above equation can be written as

$$\Delta t = (2n+1)T_{hb_n} = \frac{(2n+1)A}{\sqrt{E_n}}, \tag{4.4}$$

where

$$A(\alpha_0) = La\sqrt{2m}(1.30 - 0.56 \sin \alpha_0). \tag{4.5}$$

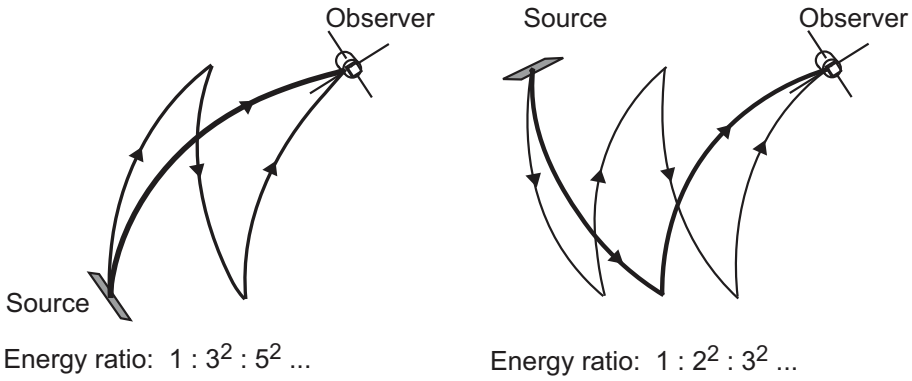

Figure 4.7: Mechanics of multiple-bounce energy banding. On the left, ions from a source in the opposite hemisphere from the observer may take odd multiples of half-bounces to reach the observer. On the right, ions from a source in the same hemisphere as the observer may take integer number of full-bounces to reach the observer.

Solving Equation 4.4 for integer values of n results in

$$\Delta t = \frac{A}{\sqrt{E_1}} = \frac{3A}{\sqrt{E_3}} = \frac{5A}{\sqrt{E_5}} = ... \tag{4.6}$$

For this equality to hold, the ion energies for 1, 3, 5 ... half-bounces must have ratios of $1 : 3^2 : 5^2$: etc. Figure 4.4 is therefore an example of multiple-bounce banding since the ratios between the energies of bands labeled A, B, C and D agree well with the ratios $1 : 9 : 25 : 49$.

For the situation where the ion source exists in the same hemisphere as the observer, the ions must take an even multiple of half bounces to be detected. The ion bounce time is then

$$\Delta t = (2n)T_{hb_n} = \frac{(2n)A}{\sqrt{E_n}}, \tag{4.7}$$

which results in

$$\Delta t = \frac{2A}{\sqrt{E_1}} = \frac{4A}{\sqrt{E_2}} = \frac{6A}{\sqrt{E_3}} = ... \tag{4.8}$$

For this case, ions would have energies in the ratios $1 : 2^2 : 3^2$: etc. Figure 4.7 illustrates these two situations.

"Type B" or "multiple-species" energy banding occurs when several different ion species take the same path from the source to the observation point. This requires

that the velocity of all ion species is the same and is illustrated as follows for the common ionospheric ions O^+, He^+, and H^+:

$$v = v_{O+} = v_{He+} = v_{H+}, \tag{4.9}$$

$$v = \sqrt{\frac{2E_{O+}}{m_{O+}}} = \sqrt{\frac{2E_{He+}}{m_{He+}}} = \sqrt{\frac{2E_{H+}}{m_{H+}}}. \tag{4.10}$$

For this to hold true, the energy ratios must be equal to the mass ratios of H^+, He^+, and O^+, namely 1:4:16.

One can determine whether Type A (multiple-bounce) or Type B (multiple-species) banding is occurring by examining the relative energies of the bands seen in the ion spectrogram. *Hirahara et al.* [1997a, b] presented observations of both banding types. Note that multiple-bounce banding is effectively the same mechanism proposed by *Quinn and Southwood* [1982] to explain the multiple bands of energy-dispersed ion signatures observed by the geosynchronous satellite ATS-6. The difference is that the source region of the ions for the observations by *Quinn and Southwood* [1982] was believed to be located in the equatorial plane in the magnetosphere.

Boehm et al. [1999] proposed a different mechanism to explain the banded energy-dispersed ion signatures in the low-latitude auroral oval studied by *Hirahara et al.* [1997a]. They argued that the acceleration of the ions was due to a compression pulse near the equatorial plane that occurred over the whole range of L shells for which the signature was observed. The decrease in observed ion energy with decreasing latitude was explained by the TOF dispersion model. Consider Figure 4.8 which illustrates their theory for equatorial acceleration. After acceleration, the ions have a broad energy and pitch angle distribution as they begin their bounce motion. Due to the dependence of the bounce period on the L-value of the field line, by the time the highest energy ions on the outer field line reach the observation altitude, lower energy ions are reaching the same altitude on the inner field line. A satellite crossing the low altitude projection of the field lines on a time period that is short relative to the bounce time of the ions would observe a decrease in ion energy with decreasing latitude.

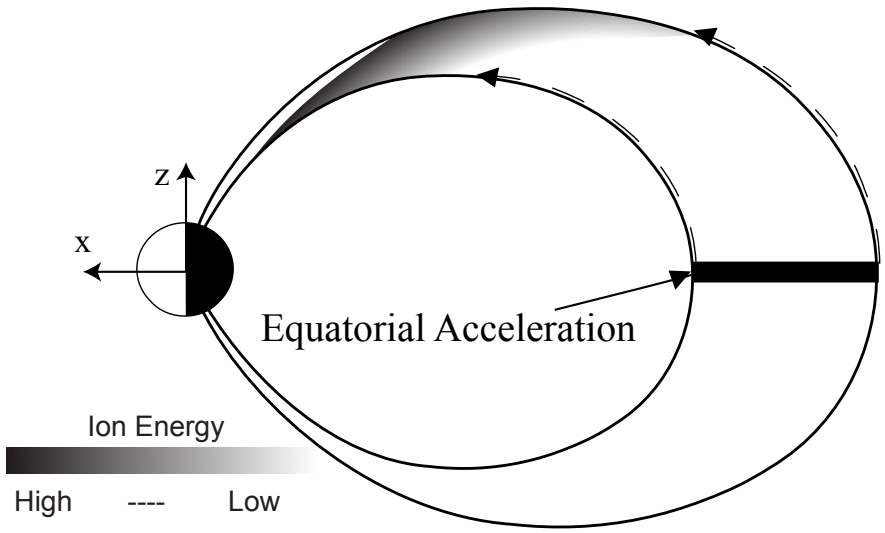

Figure 4.8: Illustration demonstrating the equatorial acceleration model combined with the TOF effect. An equatorial acceleration process occurs over a short time period. Because the field line length decreases moving inward towards the Earth, by the time high energy ions on the outer field lines reach the low altitude of a LEO satellite, lower energy ions have reached the same altitude on the shorter, inner field lines.

The banding mechanism described by *Boehm et al.* [1999] is the same as the banding mechanism described by *Quinn and Southwood* [1982], which is also like the multiple-bounce mechanism described by *Hirahara et al.* [1997a]. For *Boehm et al.* [1999], the lowest energy band is predicted to be due to ions travelling one quarter-bounce from the equatorial region to the observation altitude (initial motion northward in Figure 4.8). The second energy band is due to ions initially moving southward from the equatorial source region making three quarter-bounces. Similarly, the higher energy bands are due to ions making a consecutive odd number of quarter-bounces between the acceleration region and the observation point. With this theory, the energy ratios of the ion bands would be $1 : 9 : 25 : 49$, which is the same as the ratios expected from the multiple-bounce mechanism of *Hirahara et al.* [1997a] when the source region is in the opposite hemisphere as the observing satellite.

Boehm et al. [1999] presented a model that provided good agreement with the observations of multiple-banded, energy-dispersed signatures observed with the Fast Auroral SnapshoT (FAST) satellite (elliptical, polar orbit with initial perigee and apogee of 350 km and 4,175 km, respectively). They also stated that their model could provide a good fit to the observations of two Akebono results published by *Hirahara et al.* [1997a], especially at the lower-latitude extent of the signature. *Boehm et al.* [1999] note that the discrepancies between their model and the Akebono results could most likely be explained by inaccuracies of the Tsyganenko 96 magnetic field line model at the high-latitude extent of the signature. *Boehm et al.* [1999] also attempted to fit their model to DMSP results from *Hirahara et al.* [1997a] and found that, by assuming a field-aligned potential drop of 110 V occurring between the equatorial plane and the DMSP satellite (which is a retarding potential for precipitating ions), their model provided a "reasonable" fit.

Both authors present strong cases in favor of their own hypotheses. Examine the differences between the field-aligned ion populations and the trapped populations in the multiple-bounce banding example in Figure 4.4. The flux of the lowest energy band is the largest in the field-aligned ion panel, panel 2 (ions with a pitch angle of 0–20°). *Hirahara et al.* [1997a] state that this is evidence that the original ion distribution was a highly field-aligned structure located in the opposite hemisphere, which, after completing one half-bounce, was still a highly field-aligned structure. This supports their idea that the ions were accelerated in one hemisphere, forming ion beams that originated in the ionosphere. Wave-particle interaction with ion cyclotron waves leads to transverse accelerations, and hence to pitch angle broadening, capable of explaining the smaller but significant trapped ion distributions. *Hirahara et al.* [1997b] also noted that the ion composition measured with the IMS is often O^+, supporting their ionospheric source region hypothesis.

Hirahara et al. [1997a] also considered the full two-dimensional $\vec{E}\times\vec{B}$ convection. (By definition there is no $\vec{E}\times\vec{B}$ parallel to $\vec{B}$.) In the events studied, there was indeed a strong longitudinal component of the $\vec{E}\times\vec{B}$ drift which, when combined with a source of ions accelerated over a finite duration, would have dispersed the

ions in the same direction as the $\vec{E}\times\vec{B}$ drift. Note, however, that TOF dispersion is always present in a bouncing cluster of ions that has a large energy distribution, since TOF dispersion simply deals with the velocity dependence of the ion bounce-period.

Boehm et al. [1999] found that their Equatorial Acceleration/TOF model provided a reasonably good fit to the FAST and the Akebono data. It was rationalized that there was a lack of agreement using the TOF model at the poleward edge of the signatures because this is where the magnetic field line model is least accurate. For example, if the magnetic field model predicts a field line longer than the actual field line then the modelled energy of the ion would be too large as the ion must compensate for a longer travel distance in the same amount of time. In the TOF model, the acceleration of the event need only take place over a short time period relative to the bounce-period of the ions, but for the convective dispersion model *Hirahara et al.* [1997b] inferred that the energy-dispersed signatures "had long-term ($\sim$1 hour) and steady structures."

4.4 A generalized explanation for the dispersing mechanism

Both the explanation presented by *Hirahara et al.* [1997a, b] and that by *Boehm et al.* [1999] cannot completely explain the observations reviewed by both authors. One goal of this thesis is to reconcile the two hypotheses by postulating that the ions are of ionospheric origin and that they are accelerated out of the auroral zone, as predicted by *Hirahara et al.* [1997a], but that the acceleration of the ions took place over a short time period relative to the bounce period of the ions, as predicted by *Boehm et al.* [1999]. An ionospheric source is reasonable because of the numerous observations of outflowing ionospheric ions and the event specific observations of the presence of O^+ in the data by *Hirahara et al.* [1997a, b]. A model with a finite but not extended duration of acceleration is preferred over one that is more continuous because of the observed short term variability of the night-side auroral zone, such as auroral electron precipitation, which has time scales on the order of minutes (e.g.,

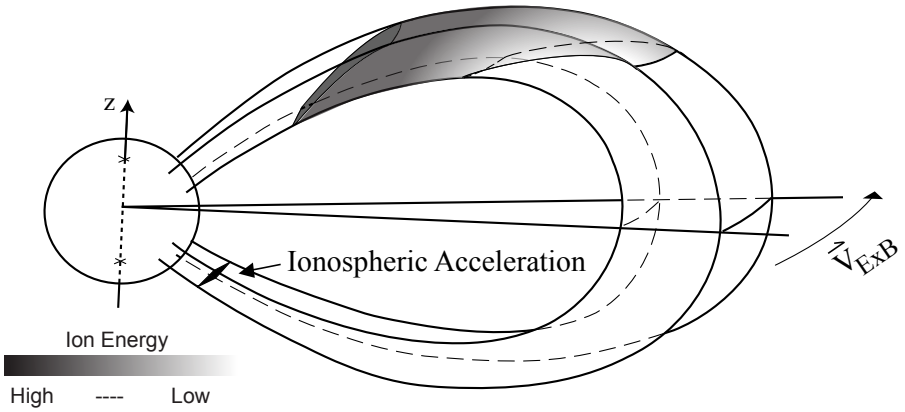

Figure 4.9: Illustration demonstrating the short-lived ionospheric acceleration model combined with the TOF effect in three-dimensions.

Trondsen and Cogger [1997]).

Assuming a short acceleration time implies that the dominant dispersing factor is the TOF mechanism, similar to what *Boehm et al.* [1999] predicted. *Boehm et al.* [1999] made the predictions under the assumption of negligible convection, but the observations made by *Hirahara et al.* [1997a] showed the existence of significant eastward convection. Therefore the simple two-dimensional illustration explaining the TOF according to *Boehm et al.* [1999] in Figure 4.8 must be expanded to three dimensions as shown in Figure 4.9.

In this figure, the acceleration region (located in the ionosphere) is extended across a finite range of L shells, as in the two-dimensional picture, and is also extended some finite distance in longitude. After a short-lived acceleration process, which heats ions to suprathermal energies, the higher energy ions outrun the lower energy ions. Low energy ions can travel one half-bounce to the altitude of an observing satellite on the shorter, inner L shell in the same time, Δt, that high energy ions reach the same altitude on the longer, outer L shell. In the 2D picture, Figure 4.8, this resulted in a 2D distribution of ions such that at a constant altitude, the ion energy decreases with decreasing L shell and therefore latitude. In the 3D picture, Figure 4.9, the same energy distribution across L shells is present in a 3D volume, which is extended in longitude.

For simplicity, imagine that the flux tubes on which the volume of ions bounce are corotating with the Earth. The dispersion of the ions along the magnetic field line (high energy ions outrunning the low energy ions) remains unchanged. After the time duration, Δt, the same volume of ions with the same energy distribution exist, but the flux tubes containing this volume of ions have rotated an angular distance, $\Delta\phi$. Therefore, a satellite moving meridionally from north to south at a constant altitude through the volume observes the same energy dispersion as it would moving through the nonrotating volume, assuming that the satellite crosses through the latitudinal extent of the volume before the entire longitudinal width has convected eastward, past the longitude of the satellite track. This illustrates that even though the observations of strong eastward (or westward) convection may lead one to conclude that convective dispersion is the dominating dispersion mechanism, the TOF mechanism may be the dominant dispersing mechanism as hypothesized in the present work.

The following chapter examines whether ions in the energy range defined as suprathermal make a significant contribution to the number density of magnetospheric ions. The production of secondary ionospheric ions is greatly enhanced within the auroral region during disturbed periods due to increased electron and ion precipitation. It is plausible then that the number of thermal ionospheric ions that are accelerated to suprathermal energies, including those responsible for the energy-dispersed ion signatures, is greatly enhanced during disturbed periods. In Chapter 5, DMSP observations of energy-dispersed ion signatures located in the dayside low-latitude auroral oval and in the SAPS region are discussed, and the possibility that suprathermal ions make a significant charge and number density contribution to the magnetosphere is examined.

In Chapter 6, a simple yet sophisticated method is described and used to determine if the short-lived ionospheric ion acceleration model can account for the magnitude of the observed energy-dispersion of two examples of multiple energy-dispersed ion signatures which were examined by both *Hirahara et al.* [1997a] and *Boehm et al.* [1999]. A similar analysis is performed for a DMSP observation of an

energy-dispersed ion signature located within the SAPS region. To aid the analysis, simulation software capable of tracing the motion of suprathermal ions in a magnetic dipole field was developed and tested, and this software is also described in Chapter 6.

Chapter 5

DMSP observations of energy-dispersed suprathermal ions

Satellite observations have shown the presence of suprathermal ions within the low-latitude auroral oval [*Winningham et al.*, 1984; *Hirahara et al.*, 1997a, a]. These signatures are characterized by a positive energy dispersion, that is an increase in energy with increasing latitude. Often these signatures are observed in several distinct energy bands. *Hirahara et al.* [1997a] predicted that these ions are accelerated out of the ionosphere due to parallel and/or transverse acceleration occurring within the auroral precipitation region. During magnetically disturbed periods, electron precipitation and observations of ion beams and conics are enhanced [*Wahlund et al.*, 1992, and references therein]. Since only 36 eV from a precipitating primary electron is required to produce a secondary ion-electron pair, the enhanced precipitating flux of the auroral energy electrons (1 keV and above) create an abundance of secondary ions within the auroral zone. Given the increase in the ionospheric ion population, combined with the increase in the probability of the ions being accelerated during auroral disturbances, one would expect a substantial number of ionospheric ions to be accelerated to suprathermal energies, creating a much larger density of suprathermal ions bouncing in the nightside magnetosphere. The disturbed two-cell convection pattern presented in Section 3.2 illustrates the ionospheric footprint of magnetic flux tubes, whose motion through the magnetosphere is governed by the $\vec{E}\times\vec{B}$ drift. Suprathermal ions are magnetically bound to these flux tubes and thus the convection maps are a two-dimensional projection of the magnetic footprint of the combined drift-bounce motion of suprathermal ions. During magnetically dis-

turbed conditions, the modified two-cell convection pattern that includes the SAPS flow illustrates velocity streamlines along which suprathermal ions may drift from the auroral zone, through the convection reversal equatorward, and into the SAPS region. Following a review of the components and format of the DMSP spectrograms in Section 5.1, Section 5.2 compares two examples of direct satellite observations of suprathermal ions flowing within both the dusk-side auroral zone and within the SAPS region. Section 5.3 presents two cases, one during magnetically disturbed conditions, one during quiet conditions, where there were only suprathermal ions flowing in the dusk-side auroral zone. In Section 5.4, a comparison between the two display options for DMSP spectrograms demonstrates the large differential number flux of these suprathermal ions in comparison to the auroral energy ions.

5.1 DMSP spectrogram format

Figure 5.1 shows the DMSP spectrogram from *Sofko et al.* [2007] for an event on April 6, 2000, plotted with software provided by the Air Force Research Lab [*F. Rich*, personal communications]. The spectrogram is composed of three panels, with the horizontal axis providing the position of the satellite in MLT, MLAT and UT. The data in the bottom panel are the vertical and horizontal ion drifts, as measured by the onboard ion drift meter, with horizontal velocities defined as positive in the sunward direction.

DMSP measures the ion drift velocity with respect to the satellite frame of reference. However, DMSP data are most often represented in a reference frame corotating with the Earth, which is useful when making comparisons with ground-based radar measurements. DMSP satellites are in a sunsynchronous orbit, and are three-axis stabilized, with the y-axis aligned along the direction of travel (see Appendix A.3). Therefore, the conversion between the satellite and the corotating frames of reference is as follows:

$$\vec{v}_{\text{ion/earth}} + \vec{v}_{\text{earth/satellite}} = \vec{v}_{\text{ion/satellite}}, \tag{5.1}$$

where $\vec{v}_{\text{ion/earth}}$ is the ion velocity with respect to the Earth and $\vec{v}_{\text{ion/satellite}}$ is the ion

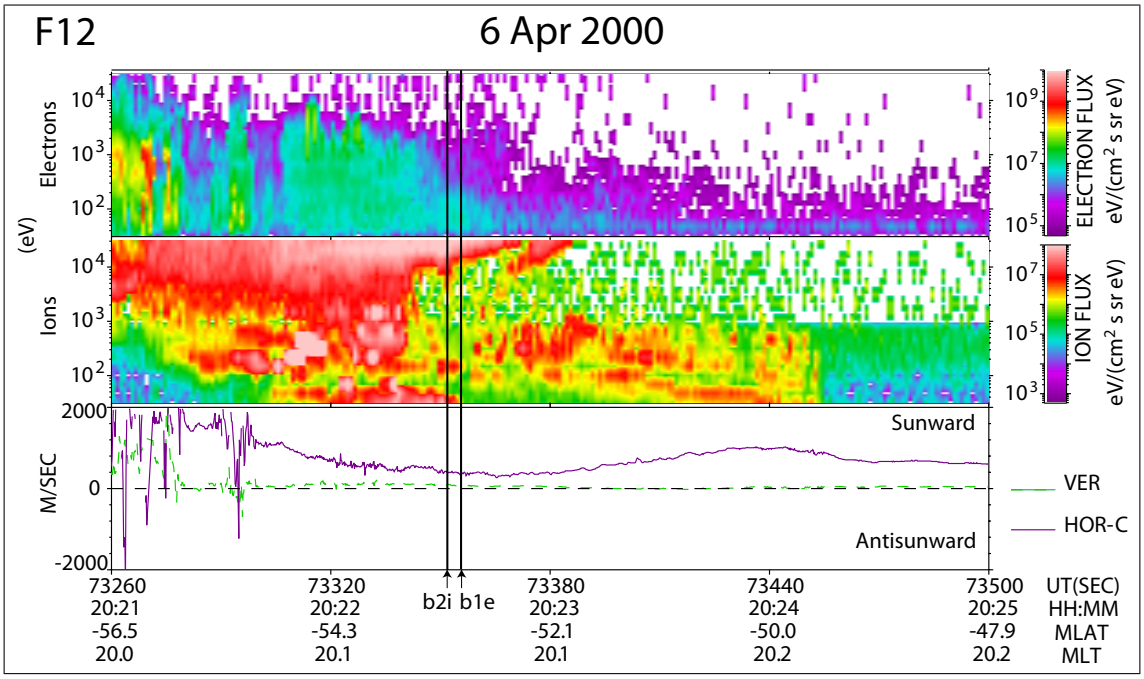

Figure 5.1: Spectrogram from DMSP F12 on April 6, 2000. Top panels display the electron and ion differential energy flux in units of eV/(cm^2·s·sr·eV). Bottom panel displays ion drift velocities plotted in the corotating frame of reference. Adapted from *Sofko et al.* [2007].

velocity with respect to the satellite. $\vec{v}_{\text{earth/satellite}}$ is the corotation velocity of the Earth given by

$$\vec{v}_{cor} = R\cos(\theta)\omega\hat{\phi}, \tag{5.2}$$

where R and θ are the satellite radial position and geographic latitude, respectively, and ω is the angular velocity of the Earth. Note that in the dusk sector where the low-latitude ion drift direction is westward, the ion velocity measured with respect to the Earth, rotating to the east, is greater than the ion velocity measured in the reference frame of the satellite. All spectrograms displayed in this chapter will contain drift measurements presented in the frame of reference corotating with the Earth.

The middle and top panels in Figure 5.1 correspond to the ion and electron differential energy flux measured in units of eV/(cm^2·s·sr·eV). The vertical axis represents the energy plotted in log scale from roughly 30 eV to 30 keV, corresponding to the

full energy range of the DMSP SSJ/4 detectors.

The automated nightside boundary identifications described by *Newell et al.* [1996] are available from the John Hopkins University online spectrogram database for the first two events. Two of these boundaries are plotted along the base of the diagram to help differentiate between auroral and subauroral regions. The b1e boundary is the zero energy electron boundary. *Newell et al.* [1996] noted that this boundary often maps magnetically to the location of the plasmapause. On DMSP spectrograms it is usually determined by the drop-off in flux in the lowest two energy channels at the equatorward edge of the auroral precipitation.

The b2i boundary is known as the high-energy ion, equatorward-precipitation cutoff, or the precipitating ion energy-flux maximum [*Newell et al.*, 1996]. In DMSP spectrograms this boundary is located by observing a peak in the ion energy flux in channels of 3 keV and greater near the equatorward edge of ion precipitation. This boundary is also the ion isotropy boundary described by *Sergeev et al.* [1983] since the ion pitch angle distribution poleward of this boundary is isotropic because of the pitch-angle scattering of ions bouncing along stretched magnetic field lines. There is, as a result, a definite precipitating flux of ions in the loss cone. Equatorward of this boundary the ions are trapped on nearly dipolar field lines, and little flux of high-energy ion precipitation is observed.

5.2 Suprathermal ions within the subauroral polarization stream

Event 1 (Figure 5.1), on April 6, 2000, occurred during an extreme geomagnetic disturbance. The Kp index exceeded 8^+ for roughly 9 hours. During this time the D_{st} index dropped below -200 nT. The DMSP satellite F12 travelled equatorward through the auroral zone in the southern hemisphere during this disturbed time. The satellite moved along the 20 MLT meridian from $-56.5°$ to $-47.9°$ MLAT in the time period from 20:21 to 20:25 UT. In the electron precipitation panel, the equatorward boundary of the keV electrons occurs at $-53.1°$ MLAT. Low energy

electrons extend 0.1° equatorward of the high energy electron boundary to the b1e boundary at −53.0° MLAT. The extension of electron precipitation to such low latitudes is extreme but not unexpected for such an intensely disturbed period.

As shown in the bottom panel, the ions underwent a strong sunward (westward) drift in the auroral zone reaching a peak speed of 2000 m/s. This drift tapers off to a minimum near the auroral electron precipitation boundary. Equatorward of this is the SAPS region of sunward flow at subauroral latitudes. In this subauroral region there is a velocity enhancement centered around -50° MLAT. The westward velocity in the SAPS region peaks at 1000 m/s, although drifts are greater than 700 m/s between −48° and −51° MLAT.

The ion panel contains three different ion precipitation cutoffs corresponding to three different ion energy ranges. The ions with energies in excess of 10 keV have high differential energy flux, and they extend equatorward to −52.1° MLAT. There is a slight flux enhancement at −53.1° MLAT, which explains the automated placement of the b2i boundary at this location. Ions in the energy range from 1 keV to 10 keV exhibit a precipitation cutoff at −53.7° MLAT, poleward of the b2i boundary. The suprathermal ions extend from well within the auroral zone at −56° MLAT, equatorward of both the b2i and b1e boundaries, into the SAPS region down to −49° MLAT.

The differential energy flux for suprathermal ions differs from that of the high-energy auroral ions. The differential energy flux of the high-energy ions is less discrete in both energy and satellite position as that of the suprathermal ions. The magnitudes of the differential energy flux of auroral ions, however, is comparable to that of the suprathermal ions within the auroral zone.

The clearest energy-dispersed suprathermal ion bands in Figure 5.1 appear near the lowest energy channels in both the auroral and subauroral regions. The lowest energy ion band in the auroral region does not appear to be correlated to the lowest energy band in the SAPS region, as there is a flux minimum near the auroral zone boundary markers. The lowest energy band in the SAPS region clearly displays an increase in energy with increasing latitude across 3° of MLAT. The increase in energy

with latitude of the suprathermal ion band in the auroral zone is not as large, but, as it spans the MLATs from the b2i boundary poleward, the peak in the energy flux moves from the lowest energy channel (30 eV) to channel 3 (68 eV). In studying ions of slightly higher energies (but still less than 1 keV), one can visualize a second, and possibly a third, ion band. However, the flux of these ions is much more intermittent in time and/or space. The differential energy flux of the suprathermal ions within the auroral zone is greater than the differential energy flux of suprathermal ions in the SAPS.

Event 2, measured on July 16, 2000, between 02:45 and 02:48 UT, occurred during another extremely disturbed period when the Kp index reached 8^- and the D_{st} index dropped below -250 nT. The magnetically active conditions persisted from 0600 UT on July 15 to 1400 UT on July 16. Figure 5.2 shows that the satellite travelled equatorward in the southern hemisphere, remaining near the 22.5 MLT meridian while traversing latitudes from $-57.5°$ to $-48.9°$ MLAT. In the top panel of Figure 5.2, the electron precipitation flux of the highest energy electrons began to taper off at $-56.4°$ MLAT. The electron energy became lower and the flux is no longer observed approximately 3° equatorward of the b1e boundary location.

The ion drift presented in the bottom panel displays a relatively sustained horizontal drift across the portion of the pass shown. A horizontal drift of approximately 800 m/s extends from $-58.0°$ to $-56.0°$ MLAT, where the velocity drops to 500 m/s. Near $-50.0°$ there are two small inflections in the horizontal drift speed profile. Equatorward of this the velocity magnitude tapers off to 200 m/s. Although not as clearly defined as the SAPS characteristics seen in the first event (Figure 5.1), the sustained drift velocity over a broad latitudinal width combined with the small inflections in the horizontal drift profile 3° equatorward of the b1e boundary is indicative of the SAPS region [*Foster and Vo*, 2002].

Similar to the first event, there are three distinct ion precipitation cutoffs. The highest energy ions (>10 keV) extend from $-57.5°$ MLAT, equatorward of the b2i boundary at $-55.2°$ MLAT, to just poleward of the b1e boundary at $-53.7°$ MLAT. The 1 to 10 keV ions are no longer observed equatorward of $-56.4°$ MLAT. The

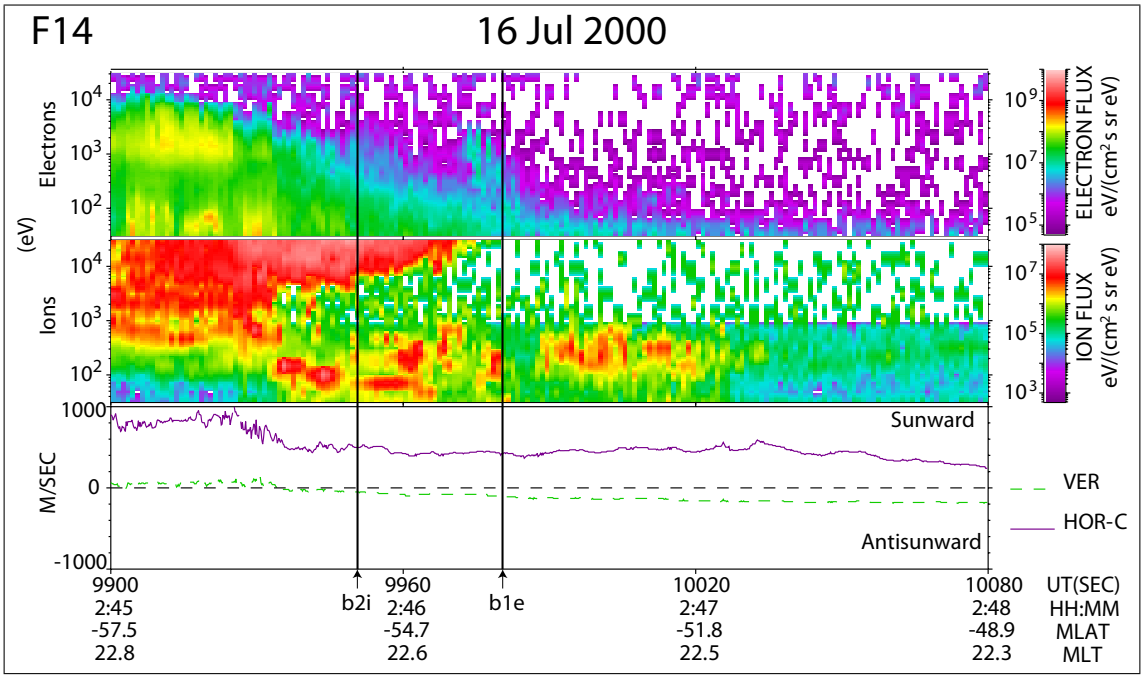

Figure 5.2: Spectrogram from DMSP F14 from 02:45-02:48 UT on July 16, 2000. Top panels display the electron and ion differential energy flux in units of eV/(cm^2·s·sr·eV). Bottom panel displays ion drift velocities plotted in the corotating frame of reference.

suprathermal ions extend through the auroral zone and roughly 2.5° into the subauroral region.

Like the first event (Figure 5.1), there is substantial low-energy ion differential energy flux within the SAPS region. However, this ion precipitation appears to be more intermittent, with no distinguishable bands within the SAPS region. There is a clear low energy band within the low latitude auroral oval that extends from −54.6° to −56.0° MLAT. At this latitude a higher and broader energy band begins and extends to the poleward edge of the spectrogram. This boundary between the lower energy band and a higher energy band aligns roughly with an increase in horizontal drift observed in the bottom panel.

5.3 Examples of pre-midnight suprathermal ions

This section compares two examples (Events 3 and 4) of energy-dispersed ion bands observed within the auroral zone in the pre-midnight sector. These two events differ from the previous two in that little to no ion precipitation within the SAPS region was observed. Event 3 was selected during the same disturbed period as Event 2, during which the D_{st} dropped below -250 nT during the most disturbed period. During Event 4 a single clear energy band was measured during a magnetically quiet period.

The DMSP F14 data for Event 3 is displayed in Figure 5.3. This event occurred on July 15, 2000, during which period the Kp index was greater than or equal to 8^+. As high as this Kp index was, the D_{st} index had not yet dropped to its lowest values of this disturbed period. At the time of this pass, the D_{st} index was -43 nT. The satellite travelled roughly along the 20 MLT meridian, moving equatorward in the southern hemisphere from -66.2° to -50.5° MLAT.

The horizontal ion drift in the bottom panel is similar to the horizontal drift from Event 2 described in Section 5.2. There is a strong sunward (westward) drift maximum centered around the poleward portion of the auroral precipitation region; the drift reaches a peak magnitude of 1200 m/s. Just equatorward of the velocity peak, the velocity drops to 700 to 800 m/s and extends across the auroral precipitation region (-62.0° to -56.0° MLAT). In the subauroral region (equatorward of -56.0° MLAT) there is evidence of the SAPS flow; the westward drift is slightly stronger near -54.5° MLAT with values of approximately 1000 m/s. The plasma drift decreases to 600 m/s at the equatorward edge (right hand side) of the plot.

The automated auroral boundary identifications were not available during this time period but the equatorward auroral precipitation boundary can be unambiguously located at -56° MLAT from the electron flux panel. Equatorward of this, the electron and ion flux is greatly reduced. Intermittent ion differential energy flux of 10^6 eV/(cm^2·s·sr·eV) (light green-yellow) extended a few degrees equatorward of this boundary, but the flux was much lower than the ion differential energy fluxes of

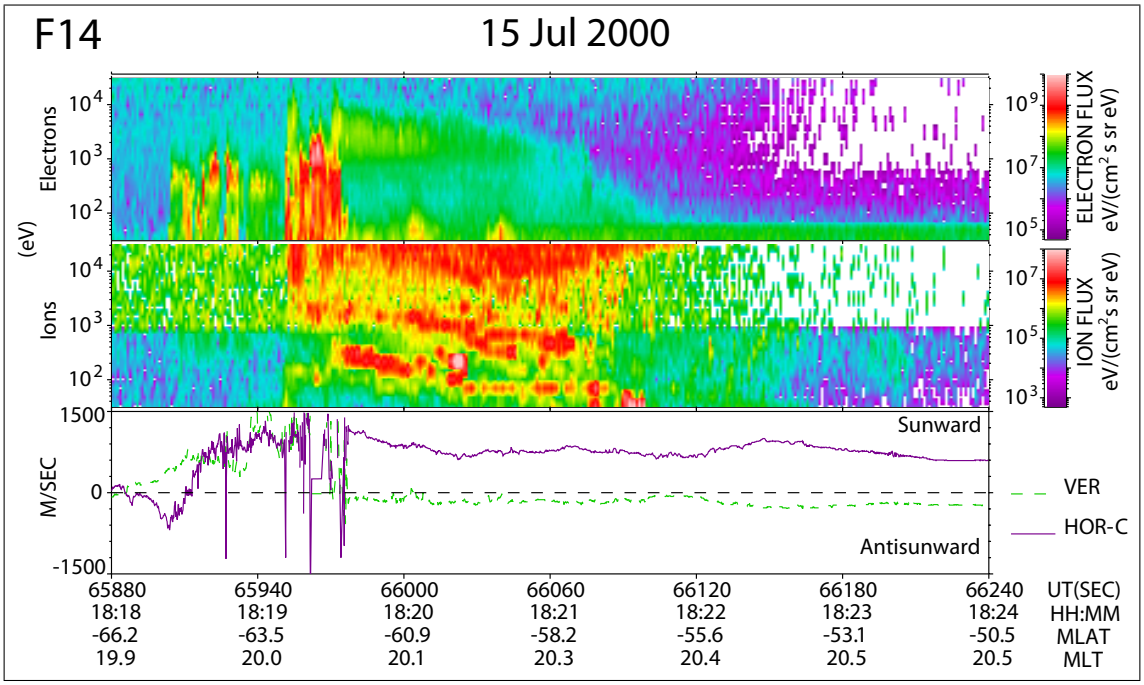

Figure 5.3: Spectrogram from DMSP F14 on July 15, 2000. Top panels display the electron and ion differential energy flux in units of eV/(cm^2·s·sr·eV). Bottom panel displays ion drift velocities plotted in the corotating frame of reference.

10^7 eV/(cm^2·s·sr·eV) and above (red-pink) within the auroral zone.

The most important feature of this diagram is that there are two very clear suprathermal ion energy bands. These bands occurred in the region of auroral precipitation. There is a clear increase in ion energy with increasing latitude. The lowest energy band ranges from 60 eV at the equatorward edge to roughly 200-300 eV at $-62.0°$. The higher energy band ranges in energy from 500 eV at the equatorward edge to 1–2 keV at $-62.0°$. The energy ratio between these two bands agrees with the ratio predicted by the multiple-bounce energy banding mechanism discussed in Section 4.3, which predicts a ratio of 1:9 between the two ion bands of lowest energy.

Event 4, presented in Figure 5.4, was measured during a quiet period on May 16, 2001. The Kp index was 2^- and the D_{st} index was at -12 nT. The DMSP F14 satellite moved westward from 23.3 to 21.9 MLT, as it travelled equatorward from $-68.8°$ to $-57.7°$ MLAT through the southern hemisphere auroral zone and into

subauroral latitudes.

The horizontal ion convection reveals a much different convection pattern than that of Event 3. While Event 3 took place in the westward low-latitude return flow of the afternoon cell, Event 4 showed precipitation across a convection reversal. Between $-68.0°$ and $-64.0°$ MLAT the horizontal drift ranged from 200 to 400 m/s antisunward. Note that the satellite trajectory in geomagnetic coordinates is northwestward and that antisunward convection corresponds to eastward convection. The convection reversal occurred between $-64.0°$ and $-62.5°$ where the horizontal velocity was approximately zero. Equatorward of the convection reversal the velocity increases. Centred around $-59.6°$ is a narrow channel of enhanced sunward flow which peaks at 1000 m/s.

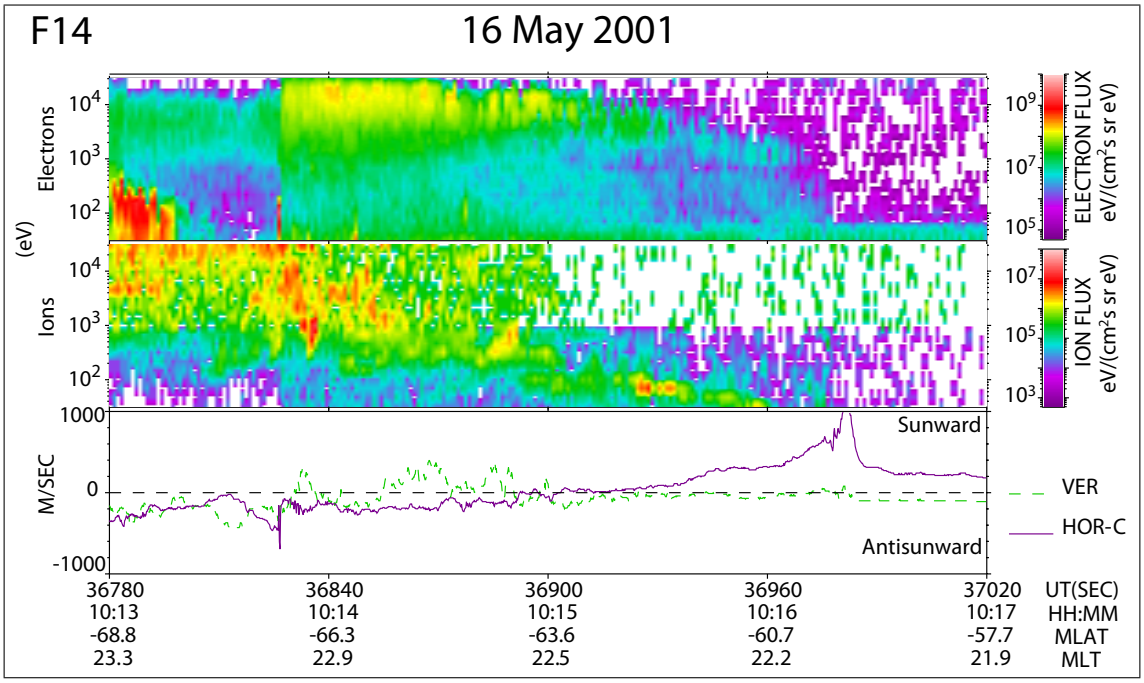

Figure 5.4: Spectrogram from DMSP F14 on May 16, 2001. Top panels display the electron and ion differential energy flux in units of eV/(cm^2·s·sr·eV). Bottom panel displays ion drift velocities plotted in the corotating frame of reference.

The equatorward electron precipiation cutoff is located near $-60.0°$ MLAT. The high energy ion cutoff was detected at $-63.5°$ MLAT, 3.5° poleward of the electron

cutoff. The ion differential energy flux is much weaker than that measured during the previous event. The suprathermal ions are also less abundant than during the more disturbed events, but they do persist over a similar range in latitude, extending from $-67.5°$ to $-60.7°$ MLAT. One striking feature of this event is the clear energy band that extends from the low energy limit of the detector at $-60.7°$ to the 100 eV range near $-64.0°$. This band occurs equatorward of the high-energy ion precipitation cutoff. The horizontal convection velocity in this region ranges from ∼300 m/s at $-60.7°$ to zero at the convection reversal.

5.4 Comparing the ion densities of suprathermal ions with ions of auroral energies

There are two commonly used display options for DMSP spectrograms. The preferred option is to plot the ion and electron differential *energy* flux which is ideal for studying the relative amount of energy that is precipitating in the form of ions and electrons. However, plotting the data as differential *number* flux better quantifies the relative amount of charge precipitating in the form of ions and electrons. The units of differential number flux are particles/(cm^2·s·sr·eV). As a comparison, the spectrogram from Event 1 (Figure 5.1) is replotted in Figure 5.5 displaying the differential number flux.

In Figure 5.1 the differential energy flux of ions of auroral energies (>1 keV) reach values nearing 10^8 eV/(cm^2·s·sr·eV) (pink). These values of the differential energy flux are comparable to that of the suprathermal ions within the auroral zone. In contrast, Figure 5.5 illustrates that the differential number flux of the suprathermal ions within the auroral zone is at least an order of a magnitude larger than the differential number flux of the auroral energy ions. This is to be expected when considering that the differential energy flux is the differential number flux multiplied by the energy per particle observed in each channel. When suprathermal and auroral energy ions are observed to have a comparable differential energy flux, as in the case presented in Figure 5.1, the differential number flux of the suprathermal ions must

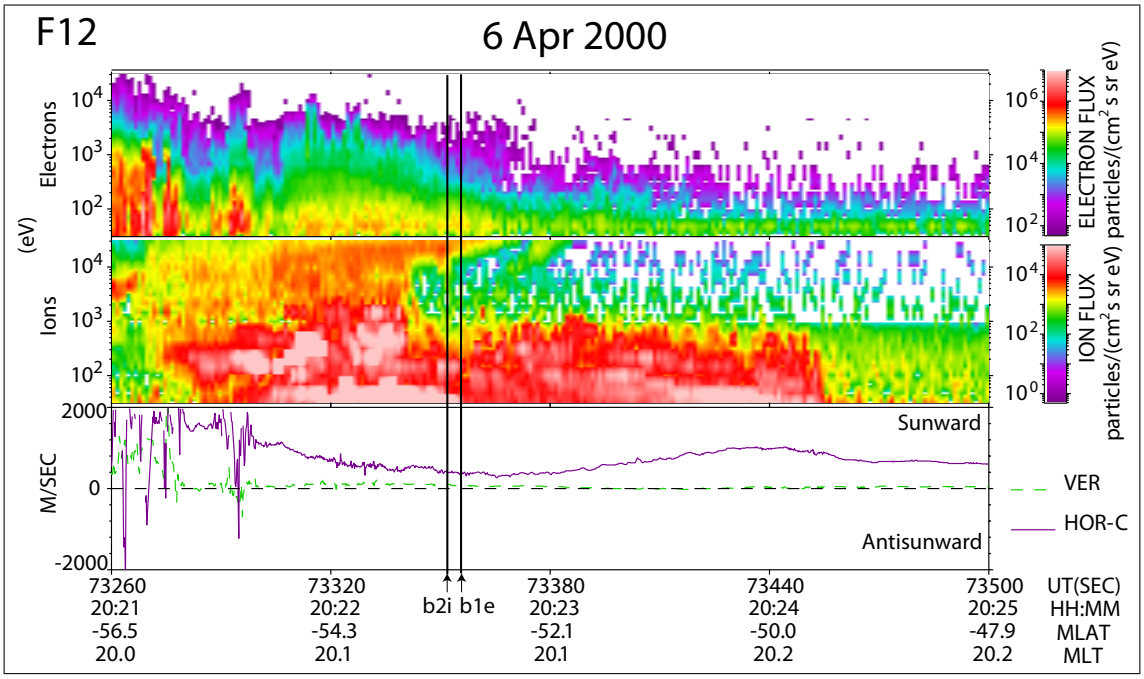

Figure 5.5: Spectrogram from DMSP F12 on April 6, 2000. Top panels display the electron and ion differential particle flux in units of particles/(cm^2·s·sr·eV). Bottom panel displays ion drift velocities plotted in the corotating frame of reference.

be greater than the differential number flux of the auroral energy ions.

Note that differential number flux and differential energy flux are measurements per unit energy width. To gain an understanding of the relative density or charge contribution of ions of both suprathermal and auroral energies, we must consider the energy ranges of auroral and suprathermal ions. Consider a rough order of magnitude calculation comparing the differential number flux across the energy width of suprathermal ions with the that across the energy width of auroral ions for Event 1. Although not a complete picture of the ion flux, the energy range of consideration can be limited to that of the SSJ/4 detectors on DMSP. For this comparison only, let us define the suprathermal ions as those ions having energies in the range from 30 eV to 1 keV, and auroral ions as those with energies from 1 keV to the highest energy channel of 30 keV. Clearly, the energy width of auroral ions is a factor of 30 larger than the energy width of suprathermal ions. In Figure 5.5 the suprathermal ions

are observed to have a peak differential number flux of 10^5 particles/(cm^2 s sr eV) while the auroral ions have a peak of 2x10^4 particles/(cm^2 s sr eV), which is spread over a narrower latitudinal width. Therefore, even with a smaller energy range, the number density of suprathermal ions can approach the total ion precipitation number flux (per unit area per unit time per unit solid angle) in the auroral zone. More importantly, when suprathermal ions are present within the SAPS region, where no auroral-energy ion precipitation is observed, suprathermal ions make the only significant contribution to the precipitating ion flux. In this specific example on April 6, 2000, the differential energy flux of suprathermal ions in the SAPS region is of the same order of magnitude as the differential energy flux of suprathermal ions observed in the auroral zone. In other words, the suprathermal secondary ions resulting from primary auroral precipitation have large enough number density and energy flux to contribute significantly to the dynamics of the disturbed magnetosphere-ionosphere system, especially in the SAPS region where only the suprathermal particles are present.

5.5 Summary and discussion of DMSP observations

This chapter highlighted the presence of suprathermal ions in both the auroral and the SAPS regions. In the April 6, 2000, event suprathermal ions are observed throughout both the auroral precipitation region and the SAPS region. There is, however, a definite boundary differentiating the two regions. Not only is the differential energy flux of suprathermal ions in the auroral zone greater than that in the SAPS region, but there is also a minimum in the differential energy flux observed at the b1e and b2i boundaries. This is consistent with the hypothesis that these ions are secondaries produced by auroral primary impact upon a thermal ionospheric population, and that the secondary ions of near-thermal energies were subsequently accelerated to suprathermal energies in the auroral zone. Recall the illustration of the modified two-cell convection in Figure 3.4. Based on this hypothesis, the

suprathermal ions observed in the SAPS region were produced in the auroral zone, from whence they followed the auroral zone convection streamlines, passing equatorward through the postmidnight convection reversal, and then westward in the SAPS region. The suprathermal ions that were observed only in the auroral zone would have been produced on auroral convection streamlines that did not go through a convection reversal, but that remain as auroral zone streamlines. It is not unexpected that such secondary ions produced in the auroral zone and then flowing on the more direct, auroral zone streamlines would have greater differential energy and number fluxes than those ions which travelled through the convection reversal into the SAPS region. The April 6, 2000, event is further analyzed in Chapter 6 to determine if the short-lived ionospheric acceleration hypothesis can explain the magnitude of the well-defined energy-dispersed signature which was observed extending approximately 4° equatorward into the SAPS region.

Suprathermal ions were also observed in both the auroral and subauroral regions during the event on July 16, 2000. In this event, however, energy-dispersed signatures were distinguishable only in the auroral region. The lack of any distinguishable energy-dispersed signatures in the SAPS region may be due to the need for a persistent, stable convection pattern. The observation of these energy-dispersed ion signatures is dependent on ions being accelerated in a region distributed in longitude and latitude and then convecting in the auroral and subauroral regions as they bounce from hemisphere to hemisphere. Fluctuations of the $\vec{E}\times\vec{B}$ drift across the latitudinal width or along the longitudinal convection path of the signature would cause the ion banding signature to deteriorate. This could account for why the poleward cutoff of the lowest energy energy-dispersed ion signature coincided with the step increase in westward convection. Also note that in all events the clearest energy-dispersed signatures coincide with convection that was observed to be rather constant or changed slowly over the latitudinal width of the signatures.

In Section 5.3, events from two different magnetically disturbed conditions were compared. The event on May 16, 2000, occurred during a magnetically quiet period. Although there were suprathermal ions observed in the region where there were

precipitating auroral-energy electrons, the differential energy flux was measurably less than during the previous events. This is expected because, during the quieter periods, less precipitation occurs, thereby resulting in a smaller secondary plasma population in the ionosphere. In addition, if the decreased auroral activity led to less favorable conditions for subsequent ion acceleration to suprathermal energies, a lower population of suprathermal ions would result. Also note that, even though there are some suprathermal ions observed in the auroral precipitation region, none are observed extending equatorward of this region. This is also expected because during the quiet periods the auroral convection pattern does not include the highly distorted penetration of the dusk cell into the dawn sector at low latitudes, which has a convection reversal that can carry auroral particles into the SAPS region. The SAPS flow is thus not enhanced because convection streamlines capable of transporting the suprathermal ions equatorward of the auroral precipitation region do not exist.

The event on July 15, 2000, occurred during a magnetically active period. Here, suprathermal ions were observed both in the auroral precipitation region and the SAPS region. The differential energy flux of the suprathermal ions in the SAPS region was an order of a magnitude less than the differential energy flux of the suprathermal ions observed in the auroral zone. This large difference in flux may be explained by the hypothesis that the ions originated due to primary precipitation in the auroral zone. Ions subsequently observed in the SAPS region would have bounced and drifted along much longer paths than the ions which were observed at auroral latitudes. If ions along this longer path make more than a single half-bounce, the distribution of ions in the loss cone is greatly reduced. After each half-bounce, ions in the loss cone are lost due to ion-particle collisions in the ionosphere and the loss cone is "emptied". Recall that the SSJ/4 detector on DMSP is aligned to view ions within the loss cone. Therefore, the only ions observable after the ions have precipitated on the second half-bounce are ions resulted from partial refilling of the loss cone by pitch-angle scattering from more transverse velocity distributions. The process of refilling may not be great enough to result in a loss cone particle flux comparable to that seen on the first half-bounce. This has important implication for

the model development and analyzed in Chapter 6. The clearest energy-dispersed signatures observed in the SAPS region by DMSP are likely to be ions that are precipitating after only a single half-bounce.

Hirahara et al. [1997a] did not emphasize the importance of studying the number density of these suprathermal ion signatures. Although much lower in energy than ring current and auroral ions, the charge of the SAPS ions gives these particles considerable significance. If present in large enough concentration, suprathermal ions may become pertinent to the study of electric fields, conductivities and shielding within the nightside magnetosphere. Section 5.4 has shown that the differential number flux of these suprathermal ions is comparable to and can be greater than that of auroral energy particles. In the SAPS region the suprathermal ions are the only significant ion flux observed.

It is interesting to note that DMSP observations reveal only the ions that precipitate below the DMSP altitude of ∼840 km. On the other hand, observations from Akebono have revealed substantial trapped distributions of ions mirroring above DMSP altitudes but below the altitude of Akebono (∼9000 km). The large energy and pitch angle distribution of suprathermal ions observed by Akebono combined with the observations of intense ion precipitation at DMSP supports the idea that a very large trapped particle population may exist, mirroring at altitudes above the orbit of Akebono. This in turn suggests that there is significant transverse acceleration which provides the ionospheric ions with enough perpendicular energy to mirror at high altitudes.

Chapter 6

Analysis of dispersed ion signatures

Primary particle precipitation within the auroral zone occurs in a region that extends over many degrees in longitude. However, the auroral precipitation is characterized by considerable spatial structure [*Akasofu*, 1964]. For example, auroral rays can be thought of as cylinders less than 2 km across [*Trondsen and Cogger*, 1998] and oriented along the magnetic field. The most intense bursts of primary auroral precipitation are often spatially localized. This region is hypothesized to be the source of both the production of a significant secondary ion population, and the acceleration mechanisms which energize the thermal secondaries to suprathermal energies. These ions, which have been called APS ions (see Section 1.3), are believed to be the source for energy-dispersed ion bands that have been observed with particle detectors on satellites.

It is hypothesized that the duration of the acceleration is comparable to the time scales of the auroral electron precipitation, which have been observed down to time scales of seconds [*Trondsen and Cogger*, 1997]. This time scale is short in comparison to the bounce period of ions. Assuming a short acceleration time implies that the dominant energy-dispersing mechanism is the TOF dispersion, as described in Section 4.4. The analysis in this chapter examines if the energy-dispersed ion signatures are consistent with the short-lived acceleration hypothesis.

DMSP particle spectrograms presented in Chapters 4 and 5 indicate that the latitudinal extent of the observed energy-dispersed ion signatures is of the order of 3°. Therefore, the latitudinal width of the ion source and acceleration region will be assumed to be roughly 3°. At an orbiting velocity of 7.5 km/s, DMSP would take roughly 50 s to traverse this latitudinal zone. During 50 s, even at a high convective

speed of 2000 m/s, ions would drift only 100 km or 1.6° in longitude. Based on this, it will be assumed that the longitudinal width of the source and acceleration region is confined to a narrow longitudinal extent of 2° .

In Section 6.3 an attempt is made to examine quantitatively the magnitude of the energy dispersion of the multiple-bounce banding event shown in Figure 4.4, as well as to investigate the possibility that the ions were accelerated over a short time period relative to the bounce period of the ions. In other words, the TOF particle dispersion will be examined as a viable mechanism to account for the magnitude of the observed energy-dispersed signature. Computer software capable of tracing the three-dimensional drift-bounce motion was developed. Using this software, an attempt was made to reproduce the multiple-banded, energy-dispersed ion signature presented in Figure 4.4. In Sections 6.4 and 6.5, two more events are presented and examined to determine if the proposed short-lived ionospheric ion acceleration model can account for the energy-dispersed ion signature. The event analyzed in Section 6.4 is a multiple-bounce auroral banding event taken from *Hirahara et al.* [1997a], which was also analyzed by *Boehm et al.* [1999]. The event analyzed in Section 6.5 consisted of well-defined, energy-dispersed ion signatures observed in the SAPS region. Additional analysis is performed for the SAPS event to determine if convection can explain the transport of the ions from the source region, which is predicted to be located in the auroral zone, to the subauroral latitudes at which they were observed.

6.1 Loss cone and bounce period calculations

The study focussed on observations of ions taken at both Akebono and DMSP altitudes. The altitude of Akebono, as listed in Figure 4.4, was 9400 to 8900 km as it traversed the region of interest from 63° to 66° ILAT. The DMSP satellite orbits the Earth at a much lower altitude of ∼840 km. Since the pitch angle of an ion increases continuously from 9000 km to 840 km, it is beneficial to compare the loss cone of ions at these two altitudes. Since the bounce period equation, Equation 4.1, is a

MLAT	L = r_0/R_E	Loss Cone at Altitude of		
		840 km	9000 km	Equator
50	2.42	57.0	12.3	12.2
55	3.04	57.4	13.6	8.4
60	4.00	57.6	14.4	5.5
65	5.60	57.8	14.9	3.2
70	8.55	58.0	15.3	1.7

Table 6.1: Calculated loss cones as a function of magnetic latitude and altitude, assuming a dipole magnetic field.

function of the equatorial pitch angle, it is also useful to calculate the loss cone at the equator. The ion loss cone at any altitude h is defined by the pitch angle $\alpha_m(h)$ that results in a mirror altitude of 100 km; all pitch angles in the range $0^\circ \leq \alpha_m(h)$ are in the loss cone for height h. Table 6.1 presents, for a dipole magnetic field, the loss cone at the equator, and at altitudes of 9000 km and 840 km for a range of invariant latitudes relevant to our study. Note that the observations from Akebono are reported in invariant latitude (ILAT) [*McIlwain*, 1961] and the DMSP observations are reported in corrected geomagnetic coordinates, or more simply, magnetic latitude (MLAT) [*Gustaffson*, 1970]. Therefore, the analysis refers to ILAT for all Akebono data and MLAT for all DMSP data.

Table 6.1 illustrates that at the low DMSP altitude, all ions with pitch angles less than 57° are within the loss cone; that is, they have a large enough field-aligned velocity component that they precipitate below 100 km. At Akebono altitudes the loss cone is defined by a smaller range of angles from 12.3° to 15.3° for an ILAT of 50° to 70°. Another way of reading this table is as follows: an ion bouncing at L = 4.0 with a pitch angle of 5.5° at the equatorial plane will have a pitch angle of 14.4° at an altitude of 9000 km, a pitch angle of 57.6° at an altitude of 840 km and 90° at the loss altitude of 100 km.

It is also beneficial to re-examine the bounce period and its dependence on pitch angle and L shell. In Figure 6.1 the half-bounce period is plotted as a function of

invariant latitude for O^+ ions mirroring at an altitude of 100 km with energies 10, 30, 50, and 100 eV. The plot illustrates that as the energy increases, the ion velocity also increases, and the time for the ion to bounce along the field line decreases. Also, as the invariant latitude increases, the length of the field line increases, and thus the bounce period increases. The pairs of vertical lines define the ranges of the invariant latitudes to which the upcoming analyses of the examples within Sections 6.3 (dashed) and 6.5 (solid) correspond.

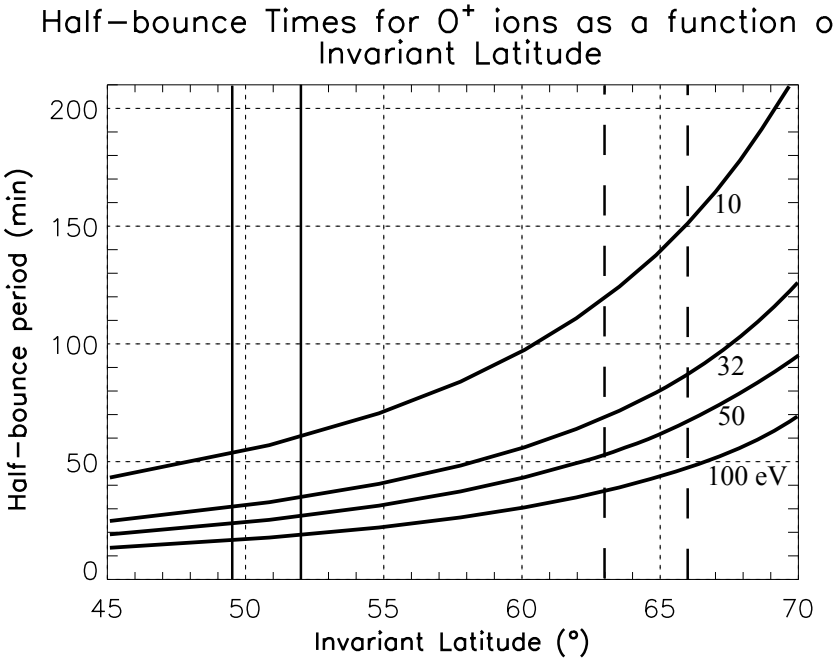

Figure 6.1: Half-bounce times for O^+ ions as a function of invariant latitude assuming a dipole magnetic field. The mirror altitude is 100 km corresponding to ions just at the loss cone. The sets of dashed and solid vertical lines define the range of ILATs which correspond to Sections 6.3 and 6.5, respectively.

6.2 Ion tracing software

6.2.1 Design of the ion tracing software

Software capable of tracing the three-dimensional motion of single particles was developed to aid the analysis of the observed energy-dispersed ion signatures. As inputs, the software requires the initial values of the ion energy, mass, position in three dimensions, and the equatorial pitch angle (which defines the initial mirror latitude). The software requires input values of the $\vec{E}\times\vec{B}$ drift velocity at all points on a chosen grid at a reference altitude in the ionosphere. The ion tracing software outputs the ion position in three dimensions, its perpendicular and parallel energy, its mirror point, and its pitch angle as a function of time.

The ion tracing software utilizes the guiding centre approximation of ion motion. Under this approximation, the perpendicular energy of the particle is defined as the sum of the perpendicular drift energy and the energy of gyration in the equation

$$K_{\perp} = \frac{1}{2}mv_D^2 + \mu B, \tag{6.1}$$

where v_D is the total drift velocity and μ is the first adiabatic invariant (see Section 2.2). The software iteratively calculates the position of the ion guiding centre (henceforth referred to as the ion position) through space using a user-defined time step, during which the ion velocity is assumed to be constant. This time step can be decreased until the accuracy of the bounce period converges to four significant figures. For H^+ ions as an example, this corresponds to an accuracy of 0.1 s in the bounce period.

Consider an ion with a known initial kinetic energy, pitch angle, and position. The ion tracing software first calculates the new position after one time-step. This involves calculating the changes in position along the magnetic field line from the original position to the new position along the original magnetic field line, and then calculating the perpendicular displacement to the magnetic field line from the new position to the final location after one time-step. This final position after the first time step becomes the starting position for the next step. The parallel velocity,

$v_\parallel$, is simply the pitch angle cosine component of the total velocity $v = \sqrt{2W/m}$. Using $v_\parallel$, the change in position along the field line is calculated. The electric field, which was input at the reference altitude, is mapped to the new position along $\vec{B}$ using the electric field mapping equations for a dipole magnetic field, as described by *Sofko and Walker* [2006]. The change in position perpendicular to the magnetic field is then calculated using the $\vec{E}\times\vec{B}$ drift from this new position. Because only the motion of suprathermal ions is being modelled, the software neglects the effect of curvature-gradient drift.

Given the final position after a step, the change in the ion perpendicular energy during that step is calculated from conservation of the first adiabatic invariant $\mu = K_\perp/B$, because the field B at the final position after one step can be calculated. The final parallel speed $v_\parallel$ at the end of the step is then calculated by conserving the total kinetic energy, given by

$$K_{\text{Total}} = \frac{1}{2}mv_D^2 + \frac{1}{2}mv_\parallel^2 + \mu B, \tag{6.2}$$

where v_D is the $\vec{E}\times\vec{B}$ drift [*Northrop*, 1963]. Given parallel and perpendicular energy of the ion at the final position after a step, the next step in time and space can be made. Whenever the ion reaches its mirror altitude, the ion tracing software reverses the direction of the field-parallel motion. The ion tracing continues until a user defined end time or a spatial crossing condition is met.

The ion tracing software assumes a magnetic dipole approximation, with the magnetic field given by Equation 2.28, reproduced here,

$$\vec{B} = \frac{B_{es}a^3}{r^3}[-2\sin\theta\hat{r} + \cos\theta\hat{\theta}], \tag{2.28}$$

It also assumes that the magnetic field lines are perfect conductors and thus no field-aligned electric fields exist.

The versatility of the software allows for further development. For example, the software may be adapted to include the effects of other drifts, such as curvature-gradient drift. Since the software traces the ion position in small increments of time, it can also be easily adapted to consider time varying functions for variables such as parallel and perpendicular acceleration.

6.2.2 Testing of the 3D ion tracing software

Testing of the 3D ion tracing software involved three independent comparisons between the numerical simulations of the software and the corresponding theoretically predicted values. These three comparisons tested the ability of the software to reproduce the correct bounce period of ions mirroring between hemispheres, the change in longitude of ions traveling longitudinally during their bounce motion, and the change in L shell of ions traveling towards lower or higher L shells during their bounce motion.

The ability of the software to predict the ion bounce period and thus the ability to model the parallel bounce motion was tested by performing multiple single particle traces under the zero $\vec{E}\times\vec{B}$ drift condition. The time required for the particles to trace a full bounce as calculated by the software was then compared to the bounce period as calculated with the full-integral bounce period equation, Equation 4.1, which is reproduced here,

$$T_{\text{bounce}} = \frac{4r_0}{v}\int_{\theta=0}^{\theta_m} \frac{\cos\theta\sqrt{1+3\sin^2\theta}}{\sqrt{1-\frac{\sin^2\alpha_0\sqrt{1+3\sin^2\theta}}{\cos^6\theta}}}d\theta. \tag{4.1}$$

The results of the comparison for an example test case are presented in Table 6.2. This test case assumed a 100 eV O^+ ion was bouncing at L = 4, and mirroring at an altitude of 100 km. The percent difference between the bounce period calculated by the software and that predicted by the full-integral bounce period equation, Equation 4.1, was 0.05%.

One of the assumptions of the ion tracing software is that the magnetic field lines are perfect conductors. *Northrop* [1963] and *Wolf* [1983] showed that when there are no field-aligned voltage drops, and when the only drift perpendicular to the magnetic field is the $\vec{E}\times\vec{B}$ drift, any two particles that are initially on the same field line will forever remain on the same field line regardless of the mirror point of each particle. This is the case for the present work which simulates the motion of low energy ions ($\sim$100 eV) for which the effect of the curvature-gradient drift perpendicular to $\vec{B}$ is negligible (see Appendix B.2). This is equivalent to the concept that the $\vec{E}\times\vec{B}$ drift

	Bounce period (sec)	Bounce period (min)
Modelled value	3709	61.83
Theortical value	3711	61.86
Percent Difference (%)		0.05

Table 6.2: Comparing the bounce period calculated by the software to that predicted with the full-integral bounce period equation. Assumes a 100 eV O^+ ion bouncing at L = 4 and mirroring at an altitude of 100 km.

is the convective drift of magnetic flux tubes onto which the low energy ions and electrons are magnetically "frozen".

If one considers the purely longitudinal motion of an ion due to an electric field which is aligned radially outward or inward in the equatorial plane, the change in longitude of an ion mirroring at ionospheric altitudes must be the same as the change in longitude of an ion whose equatorial pitch angle is 90°. The motion of the particle with the equatorial pitch angle of 90° is confined to a one-dimensional movement in the $\hat{\phi}$ direction and the change in longitude during a time period Δt is directly calculated with the relation

$$\Delta\phi\hat{\phi} = \frac{\vec{v}_{E\times B}\Delta t}{r_0}, \tag{6.3}$$

where the $\vec{v}_{ExB}$ and r_0 are the equatorial values of the $\vec{E}\times\vec{B}$ drift velocity and distance to the field line, respectively. Using the same input variables which were used for the example bounce period comparison, the software was used to predict the change in longitude due to an westward $\vec{E}\times\vec{B}$ drift of 500 m/s, mapped to the altitude of 840 km. Table 6.3 presents the change in longitude after 1800 seconds (30 minutes) predicted by the software compared to that predicted with Equation 6.3. The percent difference between the software and the theoretical calculation was 0.00004%.

For the case where the motion perpendicular to $\vec{B}$ is purely inward or outward (due to an electric field aligned west or east in the $\hat{\phi}$ direction), the change in L shell of an ion mirroring at ionospheric altitudes must be the same as the change of L shell of an ion whose equatorial pitch angle is 90°. The motion of the particle with an

	$\Delta\phi$ (°)
Modelled value	13.431110
Theortical value	13.431115
Percent Difference (%)	0.00004

Table 6.3: Comparing the calculation of the ion tracing software of the change in longitude after 1800 seconds due to a westward $\vec{E}\times\vec{B}$ drift of 500 m/s, to the theoretically calculated value. Assumes a 100 eV O^+ ion bouncing at L = 4 and mirroring at an altitude of 100 km.

	ΔL
Modelled value	1.664531
Theortical value	1.664504
Percent Difference (%)	0.002

Table 6.4: Comparing the calculation of the ion tracing software of the change in L shell after 1800 seconds due to an inward or outward $\vec{E}\times\vec{B}$ drift of 500 m/s, to the theoretically calculated value. Assumes a 100 eV O^+ ion that was originally at L = 4 and with a mirror altitude of 100 km.

equatorial pitch angle of 90° is confined to a one-dimensional movement in the $\hat{r}$ direction and the change in L shell is directly calculated with the relation,

$$\Delta L\hat{r} = \frac{\vec{v}_{E\times B}\Delta t}{\mathrm{R_E}}, \tag{6.4}$$

where $\mathrm{R_E}$ is the radius of the Earth. Using the same input variables which were used for the example bounce period comparison, the ion tracing software was used to predict the change in L shell due to a constant inward or outward $\vec{E}\times\vec{B}$ drift of 500 m/s, mapped to the altitude of 840 km at L=4 (equal to an equatorial drift of ∼5900 m/s). Table 6.4 presents the change in L after 1800 seconds (30 minutes) predicted by the software to that predicted with Equation 6.4. The percent difference between the software and the theoretical calculation was 0.002%.

It is important to note that the advantage of three-dimensional modelling is the ability to track the ion position along the field line as a function of time. Although one-dimensional calculations can predict the change in longitude and L shell, a full

three dimension simulation is needed to keep track of the position of the particle along the magnetic field line in time as the particle moves to higher or lower L shells because the bounce period of a particle is a function of the L shell. More specifically, with regard to the bounce period of ions moving from a higher L shell L_1, to a lower L shell L_2, the actual time for the ion to complete one bounce is less than the bounce period at L_1 and greater than that at L_2. The functionality of accurately tracing the location along the magnetic field line as the particle moves to different L shells is critical in any attempt to reproduce the banded energy-dispersed ion signatures studied in this thesis.

6.3 Analysis of dispersed banded structure in the morning low-latitude auroral zone

This section examines in detail the dispersed energy bands measured on December 21, 1989, and discussed by *Hirahara et al.* [1997a]. The energy spectrogram is reproduced in Figure 4.4. The goal of this analysis is to test the hypothesis that, if there is a primary particle precipitation and a resulting secondary particle population in a longitudinally narrow, latitudinally extended belt in the auroral zone, and if the resulting thermal ionospheric ions are accelerated to suprathermal energies over a time much shorter than the bounce period of the ions, the TOF mechanism can explain the magnitude of the energy-dispersed ion signatures observed with the Akebono satellite. Satellite data of the event are used to estimate the longitudinal distance between the acceleration region and the location where the ions were observed. In Section 6.3.3, the three-dimensional ion tracing software is used to reproduce the banded, energy-dispersed signature. In the following section, the ion tracing software is used to examine the effect of ion sources with differing pitch angle ranges on the energy of the observed ion bands.

6.3.1 Event on December 21, 1989

Consider Figure 6.2, which illustrates the northern hemisphere ionospheric projection of the drift component of the drift-bounce motion. The grey band labeled A is the conjugate mapping of a southern hemisphere source of APS ions. To simplify the criteria for testing if the TOF mechanism can account for the magnitude of the energy-dispersed signature, the duration of acceleration is first assumed to be instantaneous at time T_0. In Section 6.6.1, a discussion of the implications of a more finite acceleration duration is provided. For a satellite moving equatorward along a trajectory in the northern (opposite) hemisphere to observe any ions that cross point B1 at the time, T_1, then

$$T_1 = T_0 + T_{db}, \tag{6.5}$$

where T_{db} is the time for the ion to drift and bounce from the acceleration altitude in the southern hemisphere to the satellite altitude in the northern hemisphere. This time is assumed to be equal to the time for ions on drift path 1 to make one half-bounce, T_{hb1}. The error in this assumption is examined at the end of this section. Substituting for T_{db}, Equation 6.5 becomes

$$T_1 = T_0 + T_{hb1}. \tag{6.6}$$

Similarly, for the satellite to observe any ions convecting on the most equatorward streamline to point B2, T_2 is given by

$$T_2 = T_0 + T_{hb2}. \tag{6.7}$$

However, T_1 is equal to T_2 minus the time it takes the satellite to move from point B1 to B2. Therefore,

$$T_1 = T_2 - \Delta T_{sat}. \tag{6.8}$$

Written in terms of the half-bounce times, the above equation becomes

$$T_0 + T_{hb1} = T_0 + T_{hb2} - \Delta T_{sat}, \tag{6.9}$$

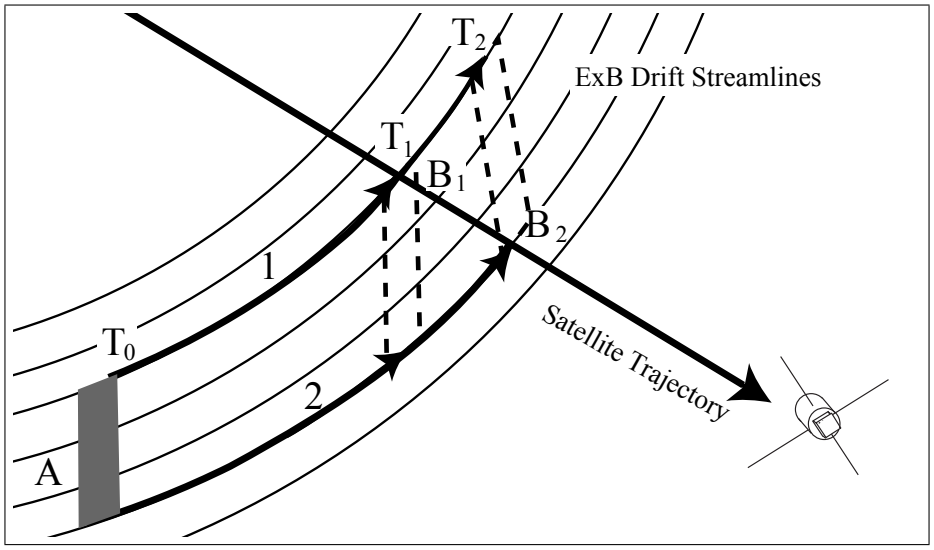

Figure 6.2: Illustration of the ionospheric projection of the transport of ions accelerated over a short time period from the narrow region labeled A at time T_0. The satellite crosses contour 1 (2) at time T_1 (T_2).

which may be simplified to

$$T_{hb1} = T_{hb2} - \Delta T_{sat}. \tag{6.10}$$

If the ions are known to have made more than one half-bounce (say three or five half-bounces) between the southern hemisphere acceleration region and the northern hemisphere observation points, then Equation 6.10 can be written in the more general form,

$$nT_{hb1} = nT_{hb2} - \Delta T_{sat}, \tag{6.11}$$

where n is the number of half-bounces.

Consider the single half-bounce case. If one can calculate the half-bounce time of ions at the poleward (B_1) and equatorward (B_2) edges of the observed energy-dispersed signatures, one can use Equation 6.10 as a simple test of whether the short-lived ionospheric ion acceleration model can account for the energy-dispersed signatures observed in the low-latitude portion of the auroral oval. In other words, after correcting for the satellite delay time, ΔT_{sat}, the poleward half-bounce time, T_{hb1}, should be equal to the equatorward half-bounce time, T_{hb2}.

For an example where the drift direction is primarily L shell aligned, as *Hirahara*

et al. [1997a] had indicated was the case for the event on December 21, 1989, the half-bounce period can be calculated using Equation 4.1. The input variables for Equation 4.1 include the ion velocity and equatorial pitch angle. The ion velocity can be calculated from the ion energy which is available from the measured energy spectrograms. Note, however, that the energy bands observed in the spectrogram have a finite energy width and thus there is a range of velocities that characterize the ion velocity at the latitudinal edges of the signature. This range results in a corresponding range of half-bounce times. Therefore, the test to see if the short-lived ionospheric ion acceleration model can account for the magnitude of the observed energy dispersion is a comparison between the *range of* T_{hb1} and the *range of* $T_{hb2} - \Delta T_{sat}$.

Figure 6.3 is the top ion panel from the spectrogram shown in Figure 4.4. These data correspond to ions in the pitch angle range of 0° to 20° at the Akebono altitude. In Section 4.3, it was shown that this is an example of multiple-bounce energy banding, in which the ion energy is proportional to the square of the number of half-bounces between the acceleration region and the observation point. Here the energy ratios agree well with the ratios 1:9:25:49, indicating that the ions have taken 1, 3, 5 or 7 half-bounces. Note that only ions making one and three half-bounces are visible in this panel. Let us first examine the time 03:17 UT when the satellite was at the poleward edge of the signature at 66.0° ILAT. A vertical dashed line at this time combined with an overlaid logarithmic scale shows that the minimum, mean, and maximum energies of the poleward edge of the lowest energy band at 66.0° ILAT are 20 eV, 50 eV, and 80 eV, respectively. Similarly, the minimum, mean, and maximum energies of the equatorward edge of Band A are 10 eV, 15 eV, and 20 eV, respectively. These values, along with the interpolated values for the energies characterizing the poleward and equatorward edges of Band B are reported in Table 6.5.

To calculate the half-bounce times T_{hb1} and T_{hb2} based on the energies interpolated from Figure 6.3 the ion mass (species) must also be known. *Hirahara et al.* [1997a] stated that their data from the suprathermal ion mass spectrometer onboard Akebono could not determine the dominant species for this event, but that the major

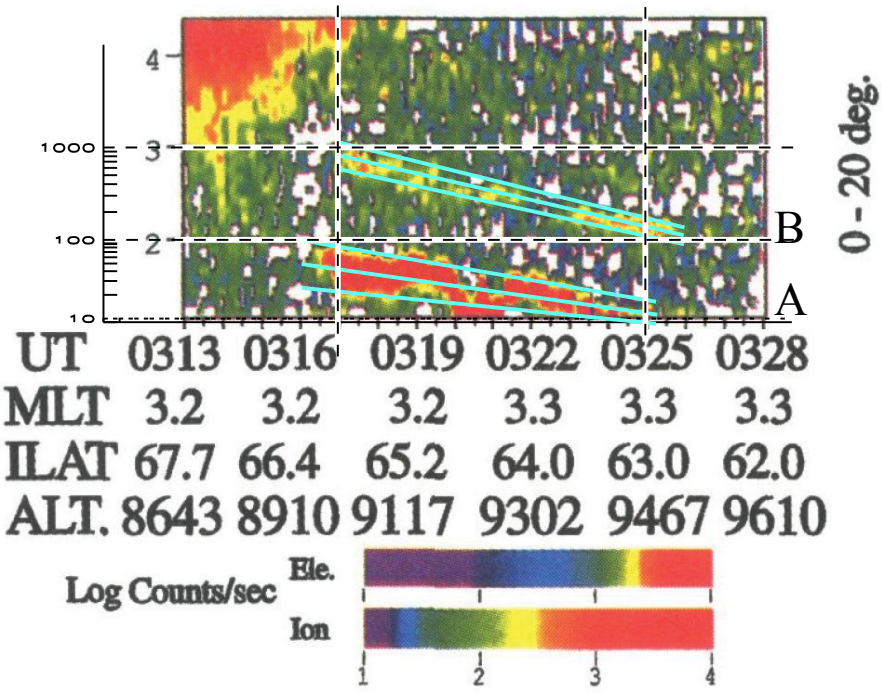

Figure 6.3: Akebono spectrogram for the event on December 21, 1989, illustrating the energy range of Bands A and B of the same event in the morning low-latitude auroral oval presented in Figure 4.4. The log scale has been added for ease of interpolation.

ion species in other events of this type is often O^+. However a very similar case was also presented where it was stated that the dominant species was H^+. Therefore, the times for T_{hb1} and T_{hb2} were calculated assuming both O^+ and H^+ ions are possible sources for the ion signature.

Figure 6.4 illustrates the comparison of the ranges of T_{hb1} with the ranges of $T_{hb2} - \Delta T_{sat}$ while assuming the ion species is O^+, as illustrated by the three solid and three dashed lines respectively. The values of the half-bounce times are plotted for pitch angles ranging from 0° to 90° (measured at an altitude of 9000 km). Note that ΔT_{sat} is 8 minutes, determined from the difference between the observation times of the two latitudinal extremes of the signature (see Table 6.5). In comparing the three solid curves defining the range of T_{hb1} with the three dashed curves defining the range of $T_{hb2} - \Delta T_{sat}$ one notes that times for $T_{hb2} - \Delta T_{sat}$ are almost completely

	ILAT (°)	Time (UT)	Ion Energy (eV) Maximum	Mean	Minimum
Band A	63.0	03:25	20	15	10*
Band A	66.0	03:17	80	50	20
Band B	63.0	03:25	200	150	100
Band B	66.0	03:17	1000	800	600

*Extrapolated value

Table 6.5: Ion energy at the poleward and equatorward extremes of the lowest energy, energy-dispersed signature, for the event on December 21, 1989.

bounded within the very large ranges of T_{hb1}, suggesting that the range of T_{hb1} is comparable to the range of $T_{hb2} - \Delta T_{sat}$. However, in comparing the middle solid curve, corresponding to the T_{hb1} calculated with the mean poleward ion energy of 50 eV, to the middle dashed curve, corresponding to the $T_{hb2} - \Delta T_{sat}$ calculated with the mean equatorward ion energy of 15 eV, one notes that the time difference between the two lines is as much as 25 minutes.

Figure 6.5 is the H^+ companion plot to Figure 6.4. When assuming the ions are H^+, there is a large region of overlap of T_{hb1} with $T_{hb2} - \Delta T_{sat}$ as defined by the bounding limits of the solid and dashed curves respectively, which is similar to the overlap for the O^+ case. However, the middle solid line, corresponding to the T_{hb1} calculated with the mean poleward ion energy of 50 eV, crosses the middle dashed line, corresponding to the $T_{hb2} - \Delta T_{sat}$ calculated with the mean equatorward ion energy of 15 eV, at a pitch angle of 5° suggesting that there is better agreement between T_{hb1} and $T_{hb2} - \Delta T_{sat}$ when assuming the ion is H^+. However, since the range of T_{hb1} overlaps the range $T_{hb2} - \Delta T_{sat}$ in both figures, the ion species can not be ascertained with any confidence.

To aid this analysis, the bounce-time comparison was repeated for the second energy band, Band B. These ions are predicted to have taken three half-bounces between the acceleration region and the observation point. Therefore the test equation,

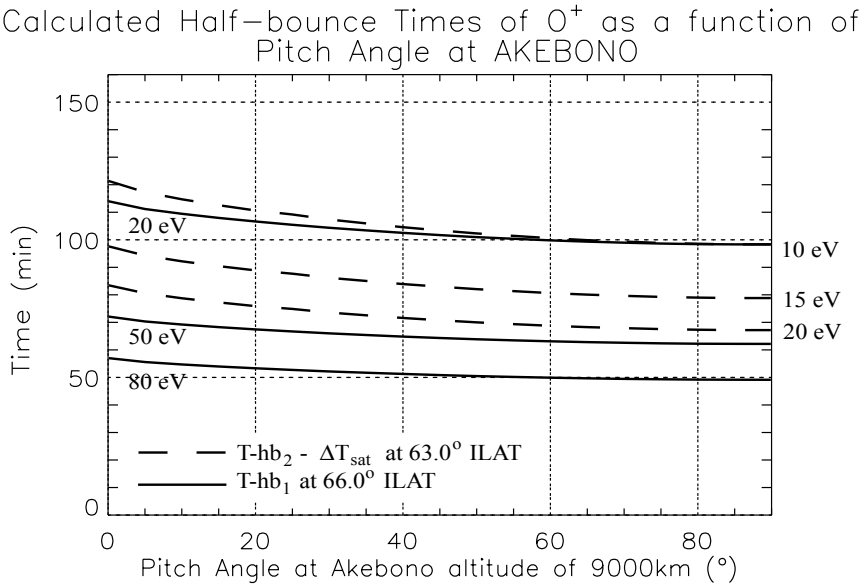

Figure 6.4: Comparison of T_{hb1} with $T_{hb2} - \Delta T_{sat}$ assuming the ions are O^+. The ion energies were interpolated from the lowest energy band (Band A) from the event on December 21, 1989.

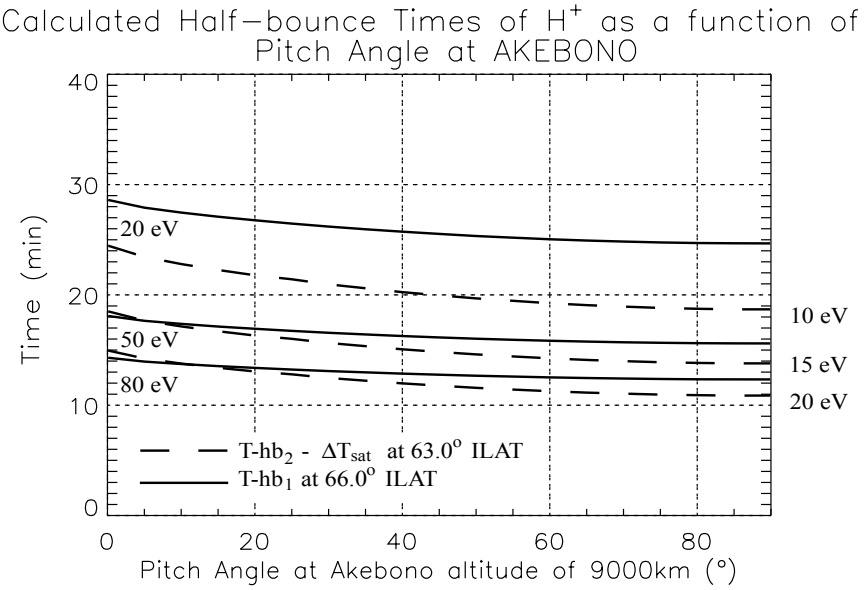

Figure 6.5: Comparison of T_{hb1} with $T_{hb2} - \Delta T_{sat}$ assuming the ions are H^+. The ion energies were interpolated from the lowest energy band (Band A) from the event on December 21, 1989.

Equation 6.11, simply becomes

$$3T_{hb1} = 3T_{hb2} - \Delta T_{sat}. \tag{6.12}$$

Figure 6.6 and 6.7 show the comparison between curves representing the range of $3T_{hb1}$ and those representing $3T_{hb2} - \Delta T_{sat}$ for O^+ and H^+. Here, there is some overlap of the two sets of curves for H^+, but no overlap exists for O^+. This suggests that the short-lived, ionospheric acceleration model can account for the magnitude of the energy dispersion if the ions are H^+.

In theory, ions making up Band B have taken three half-bounces between the time when they were accelerated and the time when they were observed, while ions in Band A have only taken a single half-bounce during the same time period. To test this theory, a comparison between curves of $3T_{hb}$ of ions of energy within the Band B is compared to the curves of T_{hb} of ions of energy within the Band A energy range in Figure 6.8. As postulated, there is considerable overlap observed in Figure 6.8. This indicates that, for H^+ ions, the multiple-bounce mechanism is responsible for the multiple bands of energy-dispersed ion signatures.

6.3.2 Estimating the location of the acceleration region

The next step in the analysis was to estimate the length of the drift path between the narrow acceleration region and the observation point (satellite track). Calculating this contour length required three variables, namely the number of half-bounces the ions made between source and observation locations, the time for the ions to make a half-bounce, and the $\vec{E}\times\vec{B}$ drift which drives the ions along the length of the bounce contour. The ions which cause the multiple bands of energy-dispersed signatures in the event on December 21, 1989 are hypothesized to have been transported from a single region. That hypothesis is supported by the excellent agreement between the range of $3T_{hb}$ of ions of energy within Band B and the range of T_{hb} of ions of energy within Band A in Figure 6.8. Therefore, this section of the analysis focuses on ions in Band A, which are ions that have made one half-bounce.

The time for one half-bounce can be interpolated from Figure 6.8. A time of

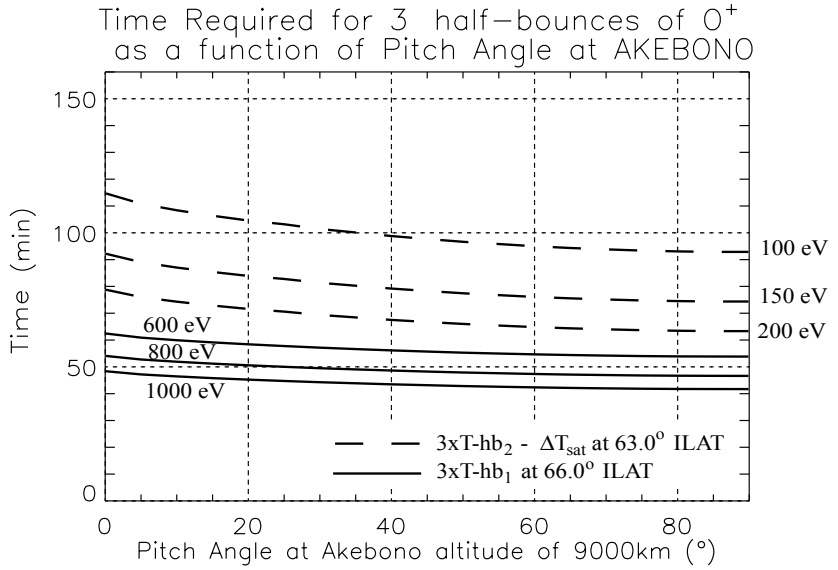

Figure 6.6: Comparison of $3T_{hb1}$ with $3T_{hb2} - \Delta T_{sat}$ assuming the ions are O^+. The ion energies were interpolated from the second energy band (Band B) from the event on December 21, 1989.

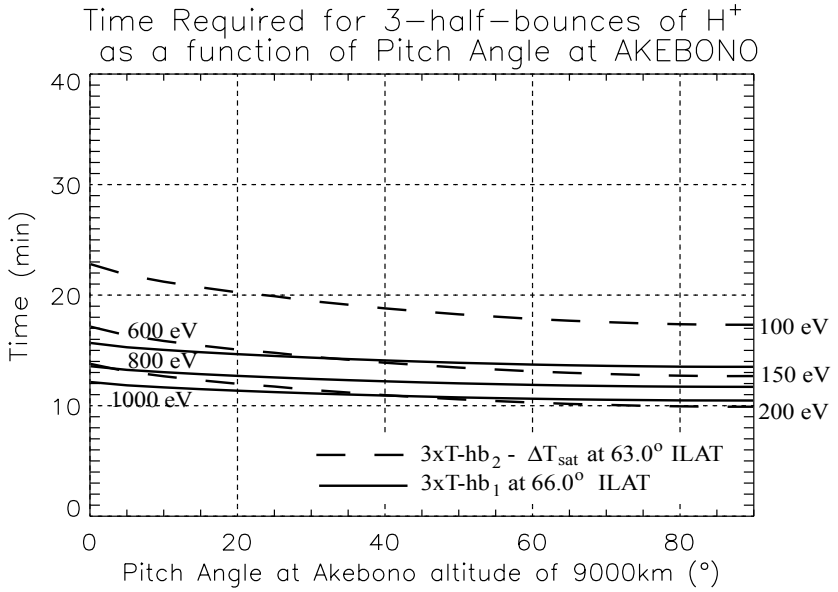

Figure 6.7: Comparison of $3T_{hb1}$ with $3T_{hb2} - \Delta T_{sat}$ assuming the ions are H^+. The ion energies were interpolated from the second energy band (Band B) from the event on December 21, 1989.

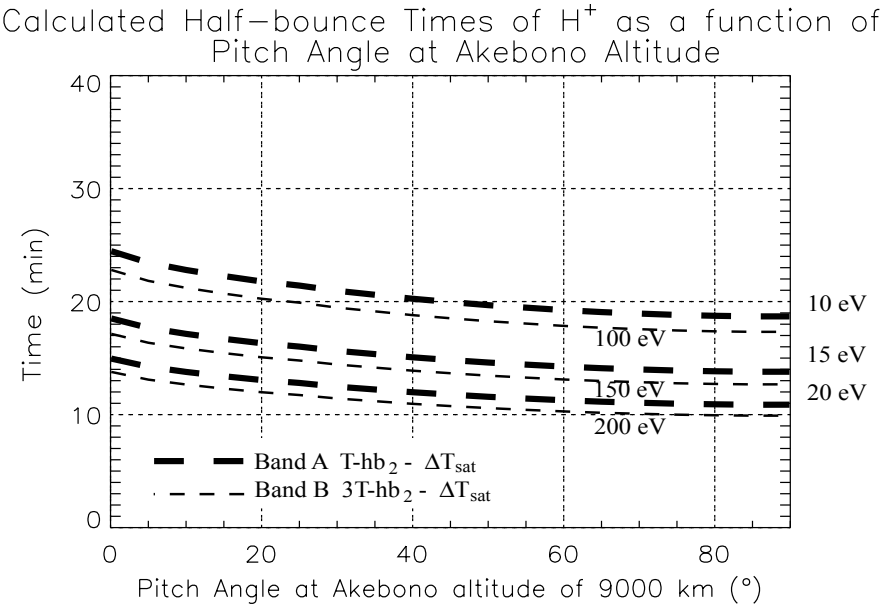

Figure 6.8: Comparison of $3T_{hb2}$ of Band B ions with T_{hb2} of Band A ions for the event on December 21, 1989. This plot assumes the ions are H^+ and the satellite delay time ΔT_{sat} was subtracted from both sets of lines.

16 ± 2 minutes fits within the overlap region across the entire pitch angle range. According to the legend on Figure 6.8, this time corresponds to $T_{hb2} - \Delta T_{sat}$ of ions in Band A, which is the half-bounce period of ions tracing along the equatorward contour minus the satellite delay time. For a ΔT_{sat} of 8 minutes, T_{hb2} is 24±2 minutes. Also, T_{hb1}, the half-bounce period of ions tracing along the poleward contour is equal to $T_{hb2} - \Delta T_{sat}$, or simply 16 ± 2 minutes.

The final missing variable required to quantify the drift path length and its variability with latitude is the $\vec{E}\times\vec{B}$ drift velocity over the region of interest for the duration of the ion drift-bounce motion. There is no data set that can completely characterize this drift for this case. However, for estimating the length of the drift path and for reproducing the ion banded dispersed structure, the drift velocity can be effectively modelled by estimating the mean drift velocity. The Akebono drift measurements (see Figure 2 of *Hirahara et al.* [1997a]) revealed a stable, eastward convection that is greater than or equal to 500 m/s (mapped to ionospheric altitudes

of 120 km) across the region of interest, over which the satellite takes slightly longer than ten minutes to travel [*Hirahara et al.*, 1997a]. Since the time spent in drift-bounce motion is greater than ΔT_{sat}, the total change in longitude between the acceleration region and the observation point is calculated at both the poleward and equatorward extremes of the signature for a range of drift velocities from 100 to 1000 m/s.

Assuming the convection is directed eastward, the calculations of the length of the drift paths are presented in Figure 6.9. The solid and dashed lines indicate the length of the equatorward and poleward drift paths, respectively, measured in degrees longitude. The error bars correspond to the error in the drift path due to the approximated error in the half-bounce times of ± 2 minutes. This figure illustrates that since the ions observed at the equatorward edge are predicted to have been drift-bouncing for 24 ± 2 minutes, 8 minutes longer than ions observed at the poleward edge, their distance between the acceleration region and observation point is also longer. Also, the length of the drift path increases linearly with increasing $\vec{E} \times \vec{B}$ drift velocity.

By combining these calculations with the actual location of the Akebono satellite during its crossing of the poleward and equatorward edges of the signature, a prediction of the possible locations of the source acceleration region was made, and three of these are presented in Figure 6.10. In this figure, the possible locations are plotted as a function of MLT and ILAT on a polar plot with the satellite track location indicated with a solid black line. A source of H^+ ions from any location combined with its corresponding $\vec{E} \times \vec{B}$ drift could explain the magnitude of the energy-dispersion seen in Figure 4.4.

6.3.3 Reproducing the banded energy-dispersed signatures

The next step in the analysis was to reproduce the multiple, energy-dispersed ion bands using the three-dimensional ion trace software. A source of H^+ ions was assumed, located along the source region and subject to a 500 m/s mean $\vec{E} \times \vec{B}$ drift speed, as displayed in Figure 6.10. The ions were assumed to have been accelerated

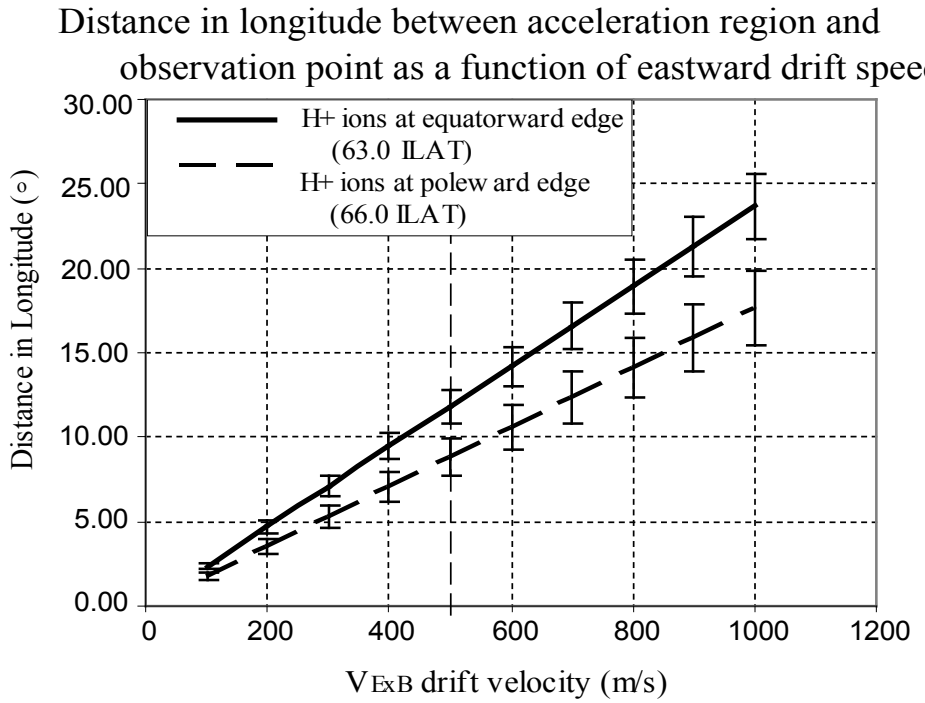

Figure 6.9: Plot of the total longitudinal distance between the acceleration region and the observation point for the event on December 21, 1989. Both the poleward (solid line) and equatorward (dashed line) longitudinal distances are illustrated. A purely eastward convection mapped to an altitude of 840 km is assumed. Error bars correspond to the error in the length of drift path calculated based on an error in the drift time of ± 2 minutes.

out of the source region in the southern hemisphere and to initiate their drift-bounce at their mirror altitudes in this hemisphere, where the mirror point is based on the pitch angle after the acceleration. A discussion on the effect of this assumption on the results is presented at the end of this section.

From the Akebono spectra, we know that the energy distribution of the ions extends from the lowest energy channel of 13 eV to the higher channels of 1 to 2 keV. This broad energy distribution was modelled with a set of single ion traces that cover the energy range from 1 eV to 1 keV using 5 eV steps except in the range between 1 and 10 eV, where 1 eV steps were used. The pitch angle of the ions at an altitude of 9000 km was initially assumed to be 20°, just outside the loss cone

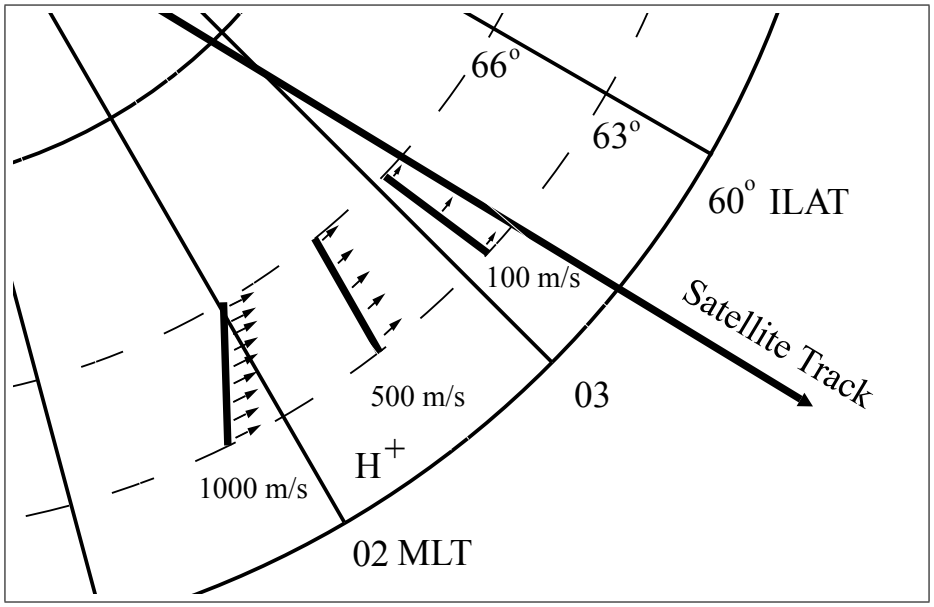

Figure 6.10: Two dimensional plot of the possible source locations for the event on December 21, 1989, assuming three eastward $\vec{E}\times\vec{B}$ drift velocities.

of 15°, and corresponds to ions with a mirror altitude of $\sim$ 1500 km. The source belt of narrow longitudinal width but extended in latitude was represented by seven positions with the ILAT of each increasing by 0.5° over the source latitude range from 63.0° to 66.0°. For example, for ions drifting at 500 m/s, the longitudinal angular extent between the observation points and the starting locations decreased linearly from 12° at 63.0° ILAT to 9.0° at 66.0° ILAT as shown in Figure 6.9.

To determine what ion energies would be observable by the Akebono satellite, the final radial position r_f measured from the centre of the Earth (in three dimensional coordinates r, θ, ϕ) was recorded for each ion trace after the ion had drifted the longitudinal distance between the acceleration region and the observation point. For each set of simulations, the final radial position was plotted for each ion. For example, consider the set of traces for the ions following streamlines at 66.0° ILAT. It was determined that the time between acceleration and observation of these ions was 16 minutes. Figure 6.11(a) plots the radial position after 16 minutes of all ions launched at an ILAT of 66.0°.

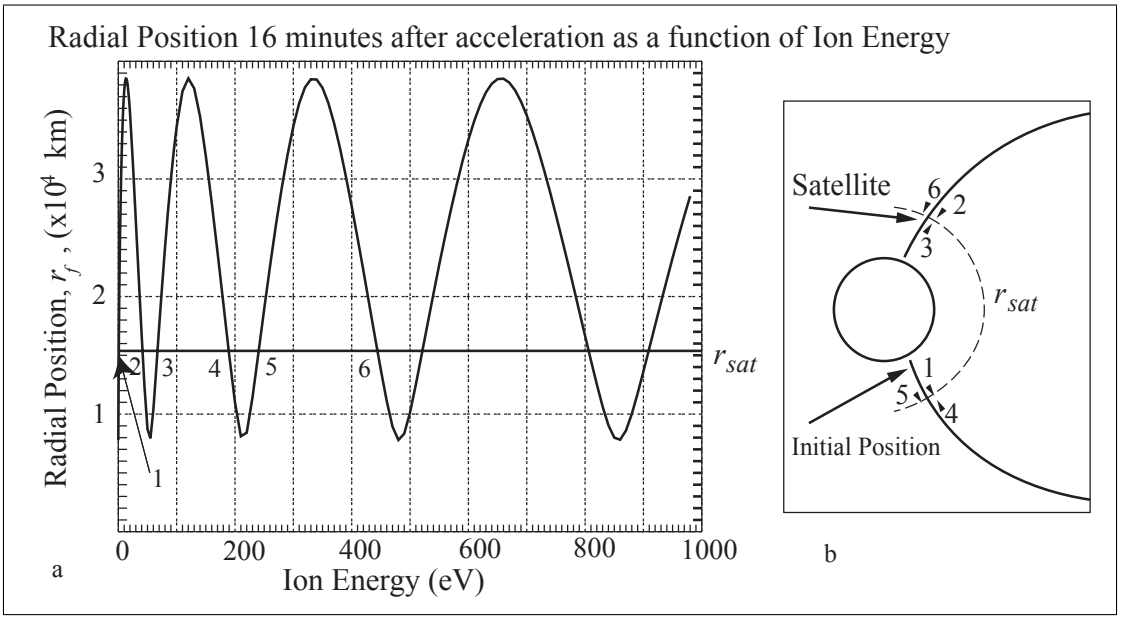

Figure 6.11: a) Plot of the final radial position r_f versus ion energy for the set of ion traces starting at ILAT 66.0°. b) Schematic of the direction and location of the first six intersections between the plot of r_f versus ion energy and the radial altitude of the satellite, r_{sat}. Plot corresponds to the analysis of the event on December 21, 1989.

Overlaid on the plot in Figure 6.11(a) is a horizontal line indicating the radial distance r_{sat} of the altitude of the satellite. The ion energies for which the plot of r_f crosses the line of r_{sat} are the energies of ions whose final radial position is at the altitude of the satellite orbit. In Figure 6.11(a), the first six crossing are labelled 1 to 6. Figure 6.11(b) points out the location of these first six crossing on the magnetic flux tube on which the ions are bouncing. The arrows in this figure indicate the direction which the ion was heading after the 16 minute drift-bounce time. For example, Point 1 corresponds to an ion with an energy of less than 1 eV, that just travelled the short distance from the starting location at its mirror point in the southern hemisphere to the altitude of the satellite in the southern hemisphere. As the satellite is located in the northern hemisphere, ions of this energy would not be observed. Point 2 corresponds to an ion with an energy of $\sim$ 40 eV. This ion travelled from the starting location at its mirror point to the satellite altitude in the

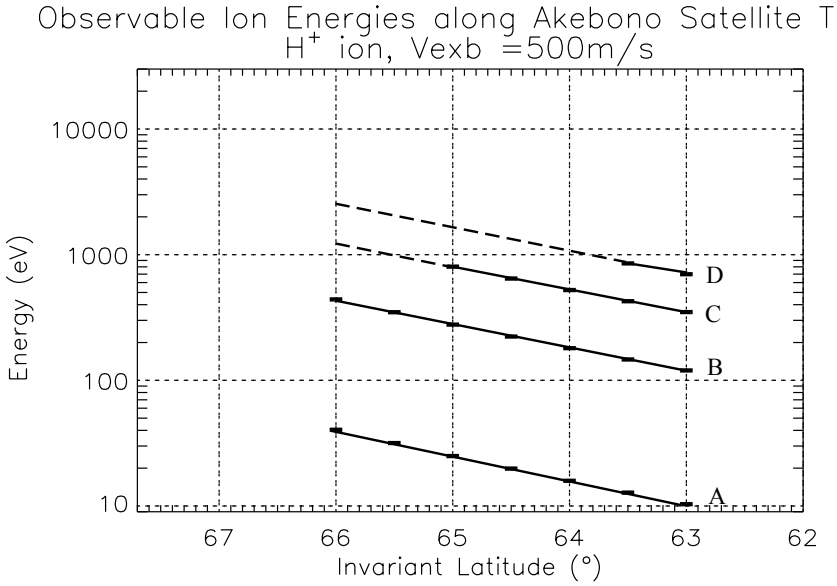

Figure 6.12: Modelled reproduction of the observable ion energies at the Akebono satellite for the event on December 21, 1989. H^+ ions of a broad energy (1–1000 eV) range were assumed to be accelerated out of one hemisphere along a narrow source region extending 3° in latitude. The pitch angle at an altitude of 9000 km was 20°.

opposite hemisphere in the 16 minutes of drift-bounce time. If one assumes that the satellite is observing ions precipitating down towards the Earth, then the satellite would observe ions of this energy. Point 3 corresponds to an ion with an energy of $\sim$ 60 eV. This ion travelled just over one complete half-bounce and is at the satellite in the north hemisphere. However, since the ion was travelling upward past the satellite, ions of this energy are not observed. The next higher energy that is observed by the satellite corresponds to ions with energy defined by Point 6. These ions are precipitating downwards past the satellite in the northern hemisphere after completing nearly three half-bounces. Using a plot like Figure 6.11 for each set of ion traces, the observable ion energies for each seven ILATs were determined.

For an assumed satellite altitude of 9000 km, the observable ion energies at each of the seven ILATs were plotted as log energy versus ILAT in Figure 6.12 for comparison with the measured Akebono spectrogram in Figure 4.4 or Figure 6.3. Just as in Figure 6.3, a straight line on the log plot fits the dispersed ion band

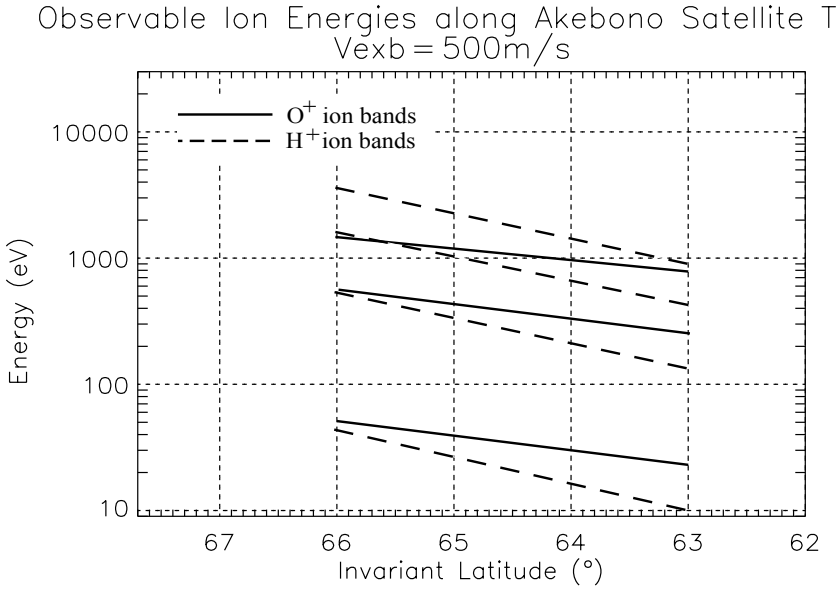

Figure 6.13: Comparing the observable bands of energy-dispersed ion signatures assuming both an H^+ (dashed lines) and O^+ (solid lines) source for which the acceleration occurred over a short time period. Assuming the $\vec{E}\times\vec{B}$ drift was constant for both ion species, the longitudinal distance travelled by the O^+ ions during their integer number of half-bounces is four times that of H^+. For the analysis of the event on December 21, 1989.

extremely well.

The simulations were repeated using an instantaneous source of O^+ ions. The $\vec{E}\times\vec{B}$ drift speed was again assumed to be 500 m/s, but the longitudinal distance between the source and the observation point was roughly four times the distance assumed for the H^+ simulation. This adjustment was to accommodate the bounce period of O^+ which, for any given energy, is four times that of H^+. Figure 6.13 compares the observable ion bands as calculated with the ion tracing software for the two ion species. The slope of the observable O^+ ion bands (solid lines) is not as steep as the slope of the H^+ ion bands (dashed lines). By comparing Figures 6.12 and 6.13 to the Akebono observations in Figure 4.4, the magnitude of the ion energy dispersion is observed to best match the H^+ ion bands.

6.3.4 The effect of pitch angle on the energies of the observable ion bands

Note that the obvious condition for an ion initially in one hemisphere to be observed after drifting and bouncing to the opposite hemisphere is that there is a common time for both motions, i.e., the drift time along the convection streamlines is equal to the bounce time (the time to complete an odd multiple of half-bounces). Consider the Hamlin approximation (Equation 4.2) for the bounce period. As the equatorial pitch angle increases, the bounce integral decreases. To meet the condition that the half-bounce time equals the drift time, which is independent of ion energy and pitch angle, the ion velocity must decrease. Referring back to Figure 4.4, which illustrates the energy-dispersed signatures in four pitch angle ranges, one might expect that the energy bands in the panel for a pitch angle range of 60° to 80° would be at lower energies than the energy bands in the panel for a pitch angle range of 0° to 20°. However, no noticeable difference in ion energy is observed, suggesting that the magnitude of the difference in energy between pitch angle panels may be too small to be observable on a spectrogram measured by a spectrometer with an energy resolution $\Delta\ E/E$ of 12%.

Using the 3D ion tracing software, the discrepancy was studied by performing another full set of single particle traces, but now assuming the ion pitch angle was 80° at altitude 9000 km. Figure 6.14 shows the observable ion energies as a function of ILAT calculated for both pitch angles (20° and 80°). Examining Band B (the second lowest energy band), the observable energy for ions with an equatorial pitch angle of 80° is indeed lower than the observable energy of ions with an equatorial pitch angle of 20°. However, the magnitude of this energy difference is roughly $\sim 2\%$ and therefore is too small to be noticeable from the Akebono spectrogram. The difference of observable energies is the smallest for the lowest energy band.

As stated earlier, the ions were assumed to initiate their drift-bounce motion at their mirror altitudes, which conflicts with the original hypothesis that the ions began their drift-bounce motion in the ionosphere. However, the effect of this difference

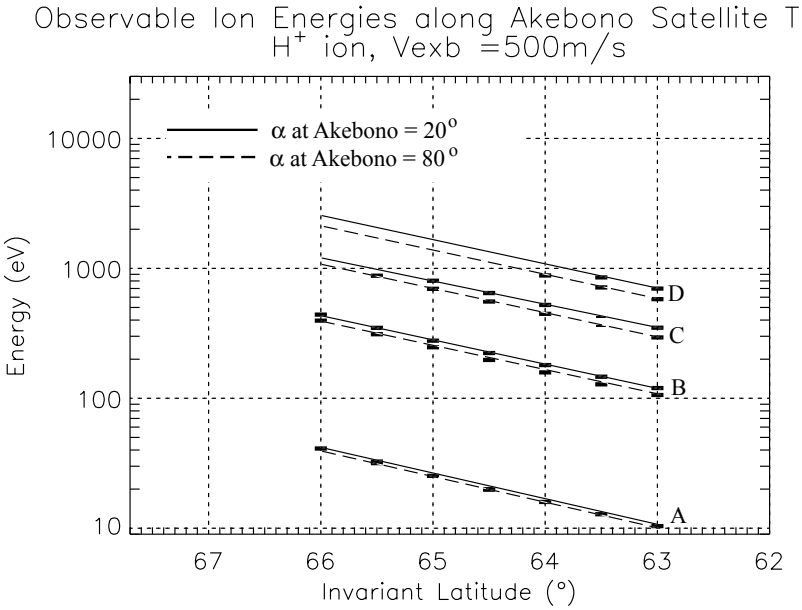

Figure 6.14: Comparing the observable ion energy for a source of H^+ ions with a pitch angle of 20° to the same source with a pitch angle of 80°. The pitch angles are referenced to an altitude of 9000 km for comparison with Figure 4.4. The graphs are applied to the analysis of the December 21, 1989, event.

in initial altitude of the drift-bounce motion on the results is small. Compare the observable ion energy bands for the ions with a pitch angle of 20° to that of ions with a pitch angle of 80° (at altitude 9000 km). Ions with a pitch angle equal to 20° mirror much closer to the ionosphere than the ions with a pitch angle of 80°. Therefore, the error imposed by assuming that the ions with a pitch angle of 80° initiate their drift-bounce motion at their mirror altitude, which is considerably higher than those with a pitch angle of 20°, must be examined.

The energies of the observable ion bands for the ions with a pitch angle of 80° are lower than the energies of the observable ion bands for the ions with a pitch angle of 20° (see Figure 6.14). If the ions with a pitch angle of 80° actually initiated their drift-bounce motion in the ionosphere, their bounce-path length would be larger. To travel this larger field-aligned distance in the same amount of time that it takes the ions to travel along the drift path, the parallel velocity, or equivalently, the

field-aligned energy of the particle must increase (noting that the time to travel along the drift-path is independent of the ion energy). Therefore, by assuming the starting point of ions with a pitch angle of 80° to be artificially higher than the actual starting point, the required parallel velocity is smaller and the calculated observable ion energy is artificially lowered. Thus, if the actual initial altitude of the ions whose observed pitch angle is 80° is near the ionosphere, the difference between the energies of the ion bands for the two simulated pitch angle ranges would be even less than the already negligible difference illustrated in Figure 6.14.

6.3.5 Discussion

In the derivation of Equation 6.11, the half-bounce period T_{hb} was assumed to equal the time required for the ion to travel between the acceleration region, which is located in the ionosphere, and the observation altitude, $T_{hb}{}'$. For an analysis using observations from DMSP, this assumption is extremely good since the altitude of DMSP is only 840 km, which is very near to the ionosphere. However, a less ideal scenario occurs when considering ions that travelled from the ionosphere in one hemisphere and are observed at the Akebono satellite, located at an altitude of 9000 km, well above the ionosphere in the opposite hemisphere. For the Akebono case presented in this section, the assumption causes over-estimates of $T_{hb1}{}'$ by 14% and of $T_{hb2}{}'$ by 18%, corresponding to roughly 3 and 4 minutes respectively, for H^+ ions. Since the assumption leads to over-estimates of both $T_{hb1}{}'$ and $T_{hb2}{}'$ by a comparable amount, the trend of the comparisons between T_{hb1} and $T_{hb2} - \Delta T_{sat}$ in Figures 6.4 and 6.5 remains the same. Note that for the comparisons in Figures 6.6 and 6.7, the assumption that $3T_{hb}$ equals $3T_{hb}{}'$ is better since the error occurs for just the last of three half-bounces instead of occurring once in a one half-bounce path.

This analysis has shown that the short-lived ionospheric ion acceleration model can account for the magnitude of the energy dispersion observed on December 21, 1989. The test criteria to examine if the TOF mechanism can account for the magnitude of the energy dispersion, which compares the drift-bounce times of ions observed at the poleward and equatorward edges of the signature, indicates that H^+

was the dominant ion species. Using the three-dimensional ion tracing software, the observed banded, energy-dispersed signature was successfully reproduced. The ion tracing software was also used to illustrate that there is negligible difference in the energy ranges of the ions bands for the two widely separated pitch angles (20° and 80°) presented in Figure 4.4.

6.4 A second event in the low-latitude portion of the auroral oval

Using the comparison of the drift-bounce time of ions travelling along the poleward and equatorward drift paths, a second event from *Hirahara et al.* [1997a] was analyzed to determine if the short-lived ionospheric ion acceleration model can account for the magnitude of the observed energy dispersion.

Figure 6.15 is the Akebono spectrogram from December 9, 1989 (from *Hirahara et al.* [1997a]), when the Kp index was 1^-. The SMS data suggested that the dominant ion species was H^+, but O^+ ions were also detected. The plot format is the same as that of Figure 4.4 with Panel 1 corresponding to the omnidirectional electron flux and Panels 2 to 5 corresponding to the ion flux in four 20° wide ranges of pitch angles from 0° to 80°. Multiple energy-dispersed ion bands are observed in the morning low-latitude auroral oval as the satellite moved equatorward (left to right in the figure) from 69.6° to 64.5° ILAT. The maximum, mean and minimum energies were interpolated from panel 2 (pitch angles 0° to 20°) for the lowest energy band near both the poleward and equatorward edges of the signature, and are presented in Table 6.6. The energy ratios between the ion bands were approximately $1 : 9 : 25 : 49$, indicating that the ions made 1, 3, 5 and 7 half-bounces between the acceleration region (southern hemisphere) and the observation points (northern hemisphere).

The $\vec{E}\times\vec{B}$ convection measured by Akebono (see *Hirahara et al.* [1997a]) was directed eastward at the latitudes over which the energy-dispersed ion signature was observed. Therefore, the ions were assumed to have travelled along a constant L shell during the drift-bounce motion. Equation 4.1 was used to calculate the half-bounce

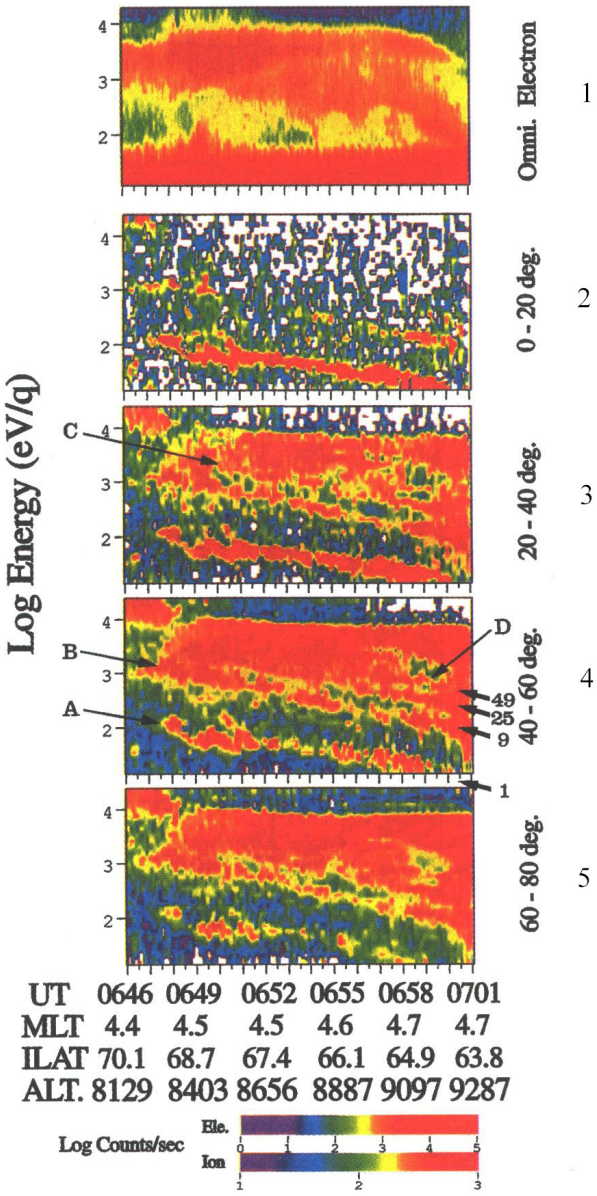

Figure 6.15: Electron and ion spectrogram taken from the Akebono satellite for the event on December 9, 1989. Ion spectrograms are sorted into four pitch angle ranges from field-aligned to near perpendicular. From *Hirahara et al.* [1997a].

	ILAT (°)	Time (UT)	Ion Energy (eV)		
			Maximum	Mean	Minimum
Band A	64.5	06:59	20	15	10*
Band A	69.6	06:47	100	80	60

*Extrapolated value

Table 6.6: Ion energy at the poleward and equatorward extremes of the lowest energy energy-dispersed signature.

time of ions with an energy in the ranges presented in Table 6.6. Figures 6.16 and 6.17 compare the three solid curves that define the ranges of T_{hb1} to the three dashed curves that define the ranges of T_{hb2} minus the satellite ΔT_{sat} assuming that the ions were O^+ and H^+, respectively. When assuming that the ions were O^+, there is poor agreement between the middle dashed curve, which represents $T_{hb2} - \Delta T_{sat}$ calculated with the mean energy at the equatorward edge, and the middle solid curve, which represents the T_{hb1} calculated with the mean energy at the poleward edge. In examining Figure 6.17, a significantly better agreement is found when assuming that the ions were H^+, as there is complete overlap of the curves defining the ranges of T_{hb1} and $T_{hb2} - \Delta T_{sat}$ for ions of a pitch angle of 20°. This indicates that the short-lived ionospheric ion acceleration model can account for the magnitude of energy dispersion observed in the event on December 9, 1989, and that H^+ is most likely the dominant species, which agrees with the observations from the SMS.

6.5 Analysis of an energy-dispersed ion signature in the subauroral polarization stream

This section presents an analysis of the event on April 6, 2000 (discussed by *Sofko et al.* [2007]) for which there was a strong flux of suprathermal ions observed in both the low-latitude auroral oval and the SAPS regions. The analysis tests whether the short-lived ionospheric ion acceleration model proposed in this thesis can account for the magnitude of the energy-dispersed signature observed in the SAPS region.

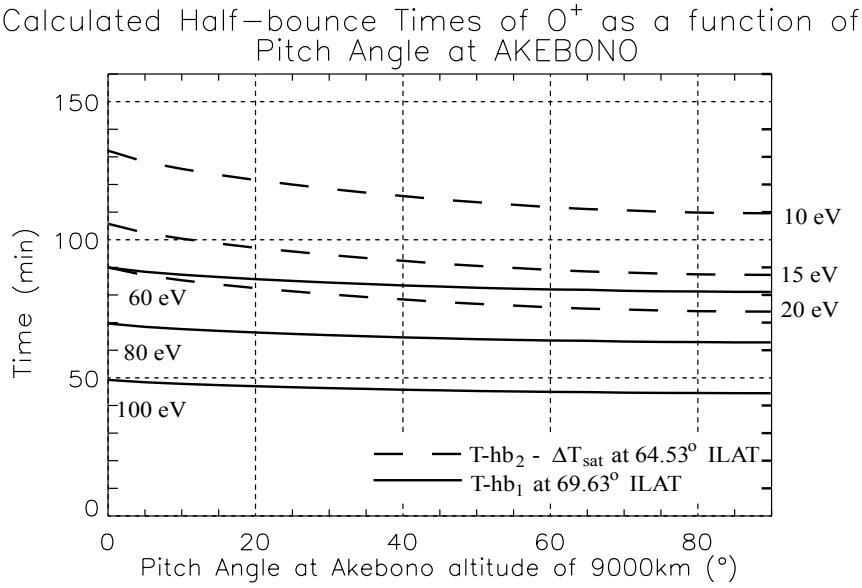

Figure 6.16: Comparison of T_{hb1} with $T_{hb2} - \Delta T_{sat}$ assuming the ions are O^+. The ion energies were interpolated from the lowest energy band (Band A) from the event on December 9, 1989.

In this section, an attempt is made to examine whether a reasonable $\vec{E}\times\vec{B}$ drift of suprathermal secondary ions from an ionospheric source located within the auroral zone can explain the subsequent presence of those suprathermal ions in the SAPS region. The methodology is similar to the analysis in Section 6.4.

The DMSP F12 satellite spectrogram in Figure 5.1 illustrates a well-defined energy-dispersed ion band appearing within the SAPS region extending from $-52.0°$ to $-49.5°$ MLAT. Table 6.7 lists the SSJ/4 channel number and its central energy, E, corresponding to the differential energy flux maximum at the latitudinal edges of the signature. The specifications in *Hardy et al.* [1984] illustrated that the discrete energy width of the SSJ/4 detector channels, $\Delta E_{SSJ/4}$, is smaller than the separation between neighboring channels ($\Delta E_{SSJ/4} \simeq 0.1E < E_i$ - E_{i-1}). However, the energy of the ion band appears to vary continuously (without discontinuous jumps) as the energy of the band increases from channel 1 at the lowest latitude to channel 4 at the highest latitude. This indicates that the energy width of the signature must be at least comparable to the spacing width of the channels themselves, and therefore

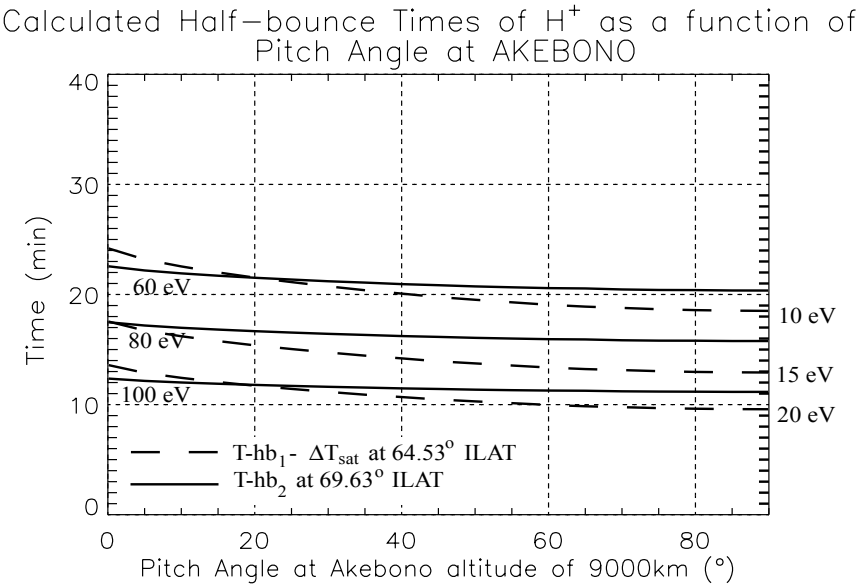

Figure 6.17: Comparison of T_{hb1} with $T_{hb2} - \Delta T_{sat}$ assuming the ions are H^+. The ion energies were interpolated from the lowest energy band (Band A) from the event on December 9, 1989.

that the maximum and minimum energies of the ion band can reasonably be defined by

$$E_{\text{maximum}} = \frac{E_i + E_{i+1}}{2}; \quad E_{\text{minimum}} = \frac{E_i + E_{i-1}}{2}, \tag{6.13}$$

where i denotes the channel number in which the peak in the flux is observed.

MLAT (°)	Time (UT)	Channel Number	Ion Energy (eV)		
			E_{maximum}	E	E_{minimum}
49.5	20:24	1	40	32	24
52.0	20:23	4	123	100	84

Table 6.7: Ion energy at the poleward and equatorward extremes of the clearest energy-dispersed signature observed in the SAPS region on April 6, 2000.

In Figure 5.1, only the lowest energy-dispersed ion band within the SAPS region is well-defined. There are hints of a second and possibly a third energy band but the differential energy flux of these bands is much more intermittent in space and/or

time. This situation is reminiscent of the Akebono spectrogram displaying ions with a pitch angle between 0° and 20° in Figure 6.3. For the Akebono event, the lowest energy-dispersed ion band is very well-defined in comparison with the second ion band. In Section 4.4, it was explained that this is expected, since ions with a field-aligned pitch angle distribution are lost due to collisions with the neutrals within the atmosphere after one half-bounce. The flux of ions in the second band corresponds to ions making three half-bounces. Since virtually all ions within the loss cone are lost after each half-bounce, the only ions observed in the field-aligned panel after a third half-bounce are ions which have undergone pitch angle scattering into the loss cone during the second and third half-bounces. If the pitch-angle scattering is weak, the second band will be weak. As the DMSP satellite observations are limited to the loss cone, observations of other energy-dispersed ion signatures such as the strong low-energy band observed in Figure 5.1 would most likely be the result of ions making a single half-bounce from the opposite hemisphere.

The DMSP satellite travelled equatorward through the auroral zone, and into the subauroral region. For the short-lived ionospheric ion acceleration model to be valid, the drift-bounce period T_{hb1} for ions observed at the poleward edge of the signature should be comparable to the drift-bounce period T_{hb2} minus the satellite transit time ΔT_{sat} for ions observed at the equatorward edge. Using Equation 4.1, the half-bounce period of ions with energies in the range outlined in Table 6.7 was calculated. For simplicity, it was assumed that, in the SAPS region, the ions primarily drifted westward along a constant L shell. Figure 6.18 compares the solid curves, which represent the range of T_{hb1}, to the dashed curves, which represent the range of $T_{hb2} - \Delta T_{sat}$, as a function of pitch angle at an altitude of 840 km. This figure is based on the assumption that the ions were O^+. The results show that there is no agreement between the range of $T_{hb2} - \Delta T_{sat}$ and the range of T_{hb1}.

In Figure 6.19, which is the companion plot to Figure 6.18, it was assumed that the ions were H^+. Like the O^+ case, there is no overlap in time between solid curves representing the range of T_{hb1} and the dashed curves representing the range $T_{hb2} - \Delta T_{sat}$. It might be argued that the assumption that the ions have

travelled primarily westward along a constant L-value could be the cause of this lack of agreement. However, consider the error in the comparison between T_{hb1} and $T_{hb2} - \Delta T_{sat}$ when the source is assumed to be positioned in the auroral zone and the convection transports the ions equatorward and westward into the SAPS region. If the source region is latitudinally narrow and longitudinally extended along the equatorward edge of the auroral precipitation, the half-bounce times for ions on both contours are actually longer than those values predicted in Figures 6.18 and 6.19. However, the increase in the half-bounce times for ions travelling on the equatorward contour is larger than that for ions travelling the poleward contour. This has the effect of making the agreement in between T_{hb1} and $T_{hb2} - \Delta T_{sat}$ worse. If the source is longitudinally narrow and latitudinally confined such that the ions first follow contours eastward, then equatorward through a convection reversal, and then westward into the SAPS region, the agreement is made even worse. The fact that $T_{hb2} - \Delta T_{sat}$ is greater than T_{hb1} means that the magnitude of the energy dispersion observed by DMSP is too large to be accounted for by the proposed model in its simplest form. It is therefore necessary to consider other possible explanations for the disagreement.

One possible solution is that the acceleration took place on a longer time scale and that there was a more steady outflow of ionospheric ions. This theory is discussed in more detail in Section 6.6.1. Another theory employed by *Boehm et al.* [1999] to aid in their analysis of particle spectra assumed that there are field-aligned voltage drops occurring at altitudes above the observing satellite. Such field aligned voltage drops have been cited by *Hirahara et al.* [1997a] as a probable acceleration mechanism for ionospheric secondary ions. Because of conservation of energy, as the thermal ion experiences a drop in electric potential energy, the kinetic energy increases. These upward potential drops appear as potential gains for suprathermal ions that are precipitating downward towards the ionosphere, and these gains act to decelerate the suprathermal ions. If an upward potential gain exists above the satellite altitude, downward-flowing ions observed by DMSP would have completed most of their half-bounce motion with energies larger than those observed. Therefore, their half-bounce

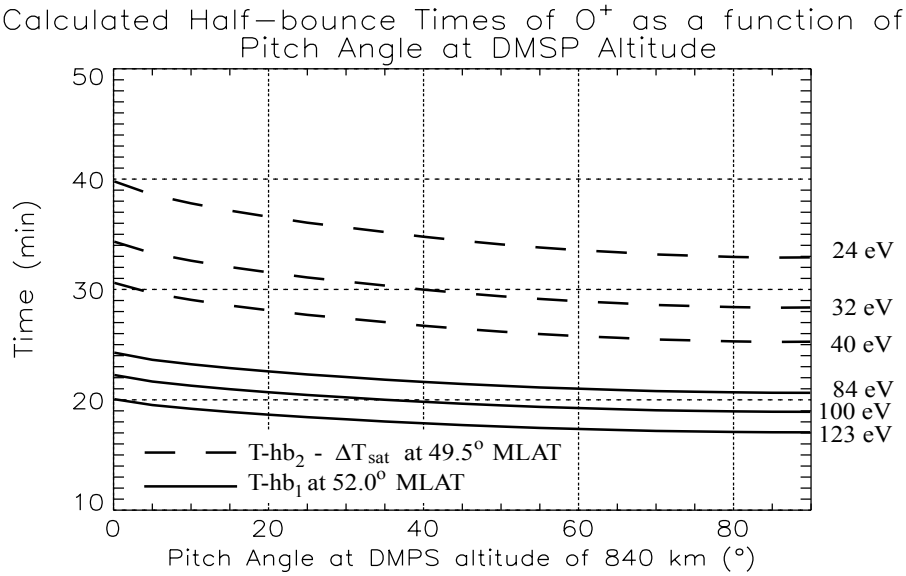

Figure 6.18: Comparison of T_{hb1} with $T_{hb2} - \Delta T_{sat}$ assuming the ions are O^+. The ion energies were interpolated from the lowest energy band in the SAPS region from the event on April 6, 2000.

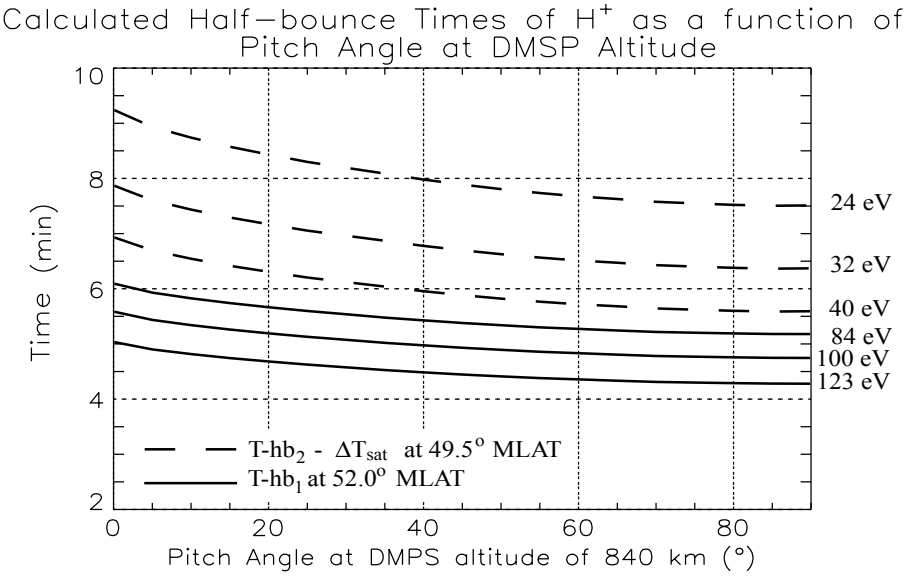

Figure 6.19: Comparison of T_{hb1} with $T_{hb2} - \Delta T_{sat}$ assuming the ions are H^+. The ion energies were interpolated from the lowest energy band in the SAPS region from the event on April 6, 2000.

periods would have been shorter than the estimates in Figures 6.18 and 6.19, thereby improving the overlap.

To calculate the voltage gains required to account for the lack of agreement between the estimated T_{hb1} and $T_{hb2} - \Delta T_{sat}$, the ion tracing software was used to model the transport of ions from an auroral zone source of APS ions, equatorward through a convection reversal and into the SAPS region. A full three-dimensional trace is necessary to properly calculate the half-bounce time of ions moving from the auroral zone into the SAPS region because the half-bounce time is directly proportional to the L-value (the larger the L-value, the longer the field line, which equates to longer half-bounce times) .

It is assumed that the auroral zone source is a longitudinally narrow belt that is extended in latitude, and is located in the northern hemisphere. The ion tracing software assumes that there is a field-aligned potential just above the ionospheric source region which accelerates the source of thermal secondary ions to suprathermal energies (1 eV to 1 keV). It is not within the scope of this thesis to delve into the details of the ion acceleration process. As ions bounce from the northern hemisphere to the southern hemisphere, the footprint of the flux tubes to which the ions are bound, trace out a half-circular high-latitude ionospheric path from the auroral zone equatorward through a convection reversal to the SAPS region where the signature is observed. The dimensions and shapes of the contour paths are illustrated in polar plot format in Figure 6.20. The dark black belt corresponds to the conjugate mapping of the northern hemisphere source into the southern hemisphere, where the observations are made. The boundary between the auroral zone and the SAPS region was selected to be located at the b1e boundary at -53.0° MLAT.

The ions observed with DMSP at the poleward and equatorward edges of the signatures are assumed to have travelled the "inner" and "outer" contours, respectively. The latitudinal range and ion energies which define the energy-dispersed signature are given in Table 6.7. Note that the ion energies reported in this table are the *observed* ion energies and the ion tracing software assumes that the *actual* energy of the ions during the majority of the drift bounce motion may have been larger, and,

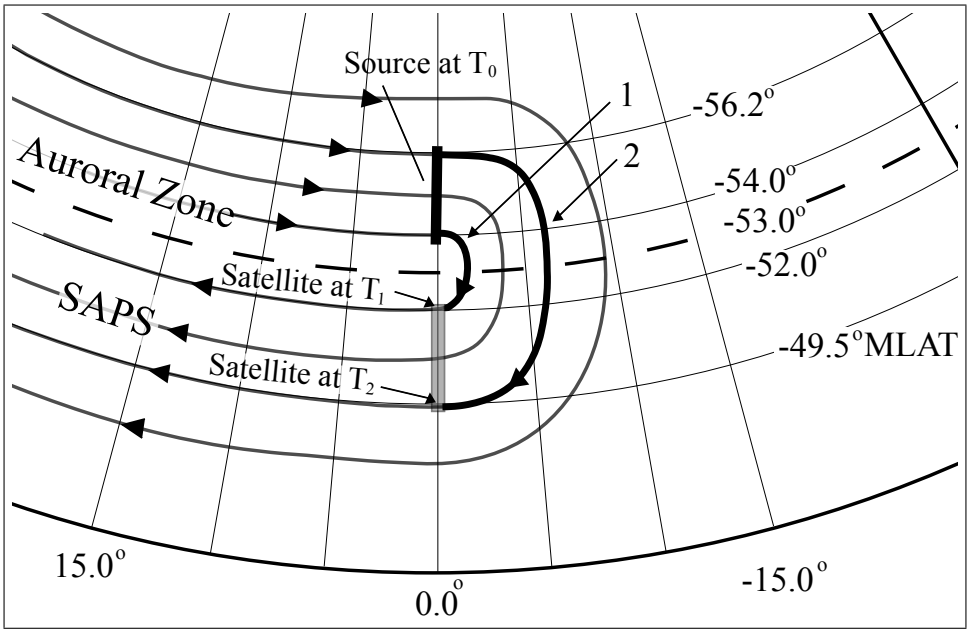

Figure 6.20: Illustration of the convection contours mapped to the southern hemisphere ionosphere. Ionospheric ions are accelerated out of a longitudinally narrow belt located in the northern hemisphere auroral zone at time T_0. The inner (1) and outer (2) convection contours consist of half-circular paths from the source region that flow equatorward through the convection reversal and into the SAPS region. The satellite positions at T_1 and T_2 are defined by DMSP MLATs of the poleward and equatorward edges of the energy-dispersed signature (located in the southern hemisphere).

due to an upward potential drop located above the observation altitude of 840 km, the kinetic energy of the ion decreases to the observed value. For simplicity, the software assumes that this upward potential drop occurs immediately above the satellite altitude.

Two solutions with field-aligned potential differences capable of satisfying the requirement that T_{hb1} is equal to $T_{hb2} - \Delta T_{sat}$ were found when assuming the ion source was O^+. For Solution 1, it was assumed that the ions travelling along the inner contour did not encounter a potential gain just prior to the satellite, and the energy observed at the poleward edge of the signature (100 eV) was the energy of the ion along its drift-bounce trajectory. The ions travelling along the outer contour, however, did encounter a potential gain such that the energy of the ions executing

drift-bounce on the outer contour was larger, and the effective $T_{hb2} - \Delta T_{sat}$ was equal to T_{hb1}. The predicted actual energy, the corresponding potential gain, and the half-bounce times for this solution are provided in Table 6.8. By employing Solution 1, a potential gain of only 60 V is required to account for the lack in agreement between drift-bounce times. Note, however, that because the outer contour has been modelled to be much longer than the inner contour, the magnitude of the drift along this contour must be larger. For Solution 1, the $\vec{E}\times\vec{B}$ drifts along the inner and outer contours were determined to be 320 m/s and 1015 m/s, respectively. Note that this increase in drift speed across the latitudinal extent is not unreasonable. In recalling the ion drift meter measurements for the April 6, 2000, event in Figure 5.1, the westward drift of ions at the equatorward edge of the energy-dispersed signature in the SAPS region was approximately 600 m/s larger than the westward drift of ions at the poleward edge.

	$E_{observed}$ (eV)	ΔV (V)	E_{actual} (eV)	Thb (min)	$v_{E\times B}$ (m/s)
Solution 1					
Inner contour	100	0	100	21.7	320
Outer contour	32	60	92	22.7	1015
Solution 2					
Inner contour	100	160	260	11.7	590
Outer contour	32	160	192	12.8	1800

Table 6.8: Two possible voltage gain solutions that can account for the lack of agreement between T_{hb1} and $T_{hb2} - \Delta T_{sat}$. Model assumes instantaneous acceleration of a source of O^+ ions located in ionosphere in the northern hemisphere. ΔT_{sat} for the April 6, 2000 event was ~ 1 minute.

For Solution 2, it was assumed that the ions travelling both the inner and outer contours encountered an equal potential gain just prior to the satellite altitude. As the values reported in Table 6.8 illustrate, a constant potential gain of 160 V accounts for the lack of agreement between T_{hb1} and $T_{hb2} - \Delta T_{sat}$. With this

solution, the actual energy of the ions during their drift-bounce motion is predicted to be much larger than the ion energy predicted with Solution 1. Therefore, the corresponding drift-bounce times are much shorter. The $\vec{E}\times\vec{B}$ convective drifts required to transport the ions along the inner and outer contours in the shorter time periods were determined to be 590 m/s and 1800 m/s, respectively. These drift speeds are not as compatible with the DMSP drift data as those calculated for Solution 1. However, these are not inconsistent with the magnitudes of drifts in the high speed flow channel called the polarization jet, or the subauroral ion drift that has been observed during magnetically disturbed periods (e.g., *Oksavik et al.* [2006]).

An attempt was made to model H^+ ions as the ion source responsible for the energy-dispersed signature. However, drifts of 3000 to 4000 m/s are required to transport the H^+ ions along the convection contours in the much shorter half-bounce times of H^+. These drifts are unrealistically high. One can conclude that the well-defined energy-dispersed signatures observed in the SAPS region, such as the event on April 6, 2000, are more likely to be the result of O^+ ions.

6.6 Discussion

6.6.1 Duration of acceleration

The hypothesis proposed to explain the energy-dispersed ion signatures observed in the low-latitude auroral and SAPS regions assumes that the acceleration of the ionospheric ions, the source of which is located in the auroral zone, occurred over a time period much shorter than the bounce period of the ions. Sections 6.3 to 6.5 provided evidence that this model could account for the magnitude of the energy-dispersed ion signature observed in three events. This short-lived ionospheric ion acceleration model is preferred over a model which assumes that the acceleration occurs more continuously because the nightside auroral zone is highly variable. However, it is beneficial to consider how the conclusions of the analysis may vary by assuming a more extended period of acceleration.

The method used to test if the proposed model could account for the magnitude of the energy-dispersed signature involved comparing the time required for ions to travel from the acceleration region to the observation point on the poleward drift path, in essence a comparison between the poleward drift-bounce time and the equatorward drift-bounce time. These drift-bounce times were calculated for a range of energies corresponding to the energy width of the ion band. If the ions were accelerated out of the ionosphere over a very short time period, after accounting for the delay time of the satellite crossing, the range of poleward drift-bounce times should overlap the range of equatorward drift-bounce times. If, however, the acceleration of the ions occurred over a longer time period, the requirement of the overlap of the two ranges may be relaxed by the time interval of the acceleration.

As an example, consider the Akebono event on December 9, 1989, where the range of poleward drift-bounce times overlapped the range of equatorward drift-bounce times almost precisely when H^+ was assumed to be the dominant species. A similar overlap is possible for O^+ if it is assumed that the acceleration of the ions occurred for approximately 40 minutes. This is of the same order of magnitude as the bounce period of O^+ ions which have energies less than 100 eV. It is also comparable to the value *Hirahara et al.* [1997b] have stated for the time period over which they inferred that the structures were stable. If these ion structures are produced over such a long time period, future research is necessary to examine what acceleration mechanisms exist that can persist for that long a period.

In the event on April 6, 2000 a clear energy-dispersed ion band was observed in the SAPS region. After comparing the ranges of the drift-bounce times at the poleward and equatorward edges of the signature and while accounting for the time delay of the satellite, no overlap between T_{hb1} and $T_{hb2} - \Delta\ T_{sat}$ was found while assuming either O^+ or H^+. In Section 6.5 this lack of agreement was overcome by assuming that field-aligned potential drops existed above the observing satellite that acted to decelerate the precipitating ions. If this assumption is removed, similar agreement in the comparison of the ranges of T_{hb1} and $T_{hb2} - \Delta\ T_{sat}$ can be achieved by assuming the duration of the acceleration was approximately 12 minutes if the

ions were O^+, or 3 minutes if the ions were H^+. Note that 3 minutes for H^+ is not a short duration compared to the ion bounce period of H^+, which is between 5 and 10 minutes as seen in Figure 6.19. Therefore, if no potential drop solutions exist to explain the lack of agreement between the ranges of T_{hb1} and $T_{hb2} - \Delta\ T_{sat}$, the requirement that the acceleration took place over a time period short compared to the ion bounce period ($<0.1\ T_{hb}$) must be relaxed.

6.6.2 A source of H^+ ions

The hypothesis examined in the present work was based on the assumption that the suprathermal ions observed drift-bouncing in the region of the magnetosphere mapping to the low-latitude portion of the auroral oval and then into the SAPS region are likely to be APS ions. That is, these ions are secondary ions which have been created by primary electron precipitation within the auroral oval and then have been accelerated by transverse and parallel acceleration mechanisms to suprathermal energies. The altitude of ionization of auroral energy electrons is from 120–200 km [*Rees*, 1982]. In recalling Figure 1.3, a sample ion and neutral density profile of the ionosphere, one can see that the majority neutral atom in this region is O. Therefore, the majority of secondary ions created by auroral electron precipitation are O^+ ions. The results of the analysis in Section 6.5 indicated that the suprathermal ions observed in the SAPS region are most likely to be O^+, which is consistent with the ion production theory. However, the results of the analyses in Sections 6.3 and 6.4 indicated that the ions observed in banded energy-dispersed signatures in the low-latitude portion of the auroral oval were H^+. This suggests that the ionosphere may be acting as a source of both O^+ and H^+ ions to the suprathermal ion populations observed in the magnetosphere.

Two significant ionization mechanisms exist which could be responsible for the secondary populations of H^+ in the ionosphere. Figure 6.21 presents the calculated values of the densities of molecular and atomic hydrogen as a function of altitude [*Schunk and Nagy*, 2000]. Below 150 km, the densities of H and H_2 reach 10^8 cm^{-3} and 10^{10} cm^{-3}, respectively. Above 150 km, the densities of H_2 and H

decrease to roughly 10^5 cm^{-3} and 10^3 cm^{-3}, respectively. Even though these neutral densities do not compare to the density of atomic oxygen below 300 km, auroral electron precipitation could create a significant secondary population of H^+. Also note that the mass of H is one-sixteenth the mass of O and thus H^+ ions can diffuse more easily upward along the magnetic field to regions where the recombination rates are lower due to lower neutral and ion densities.

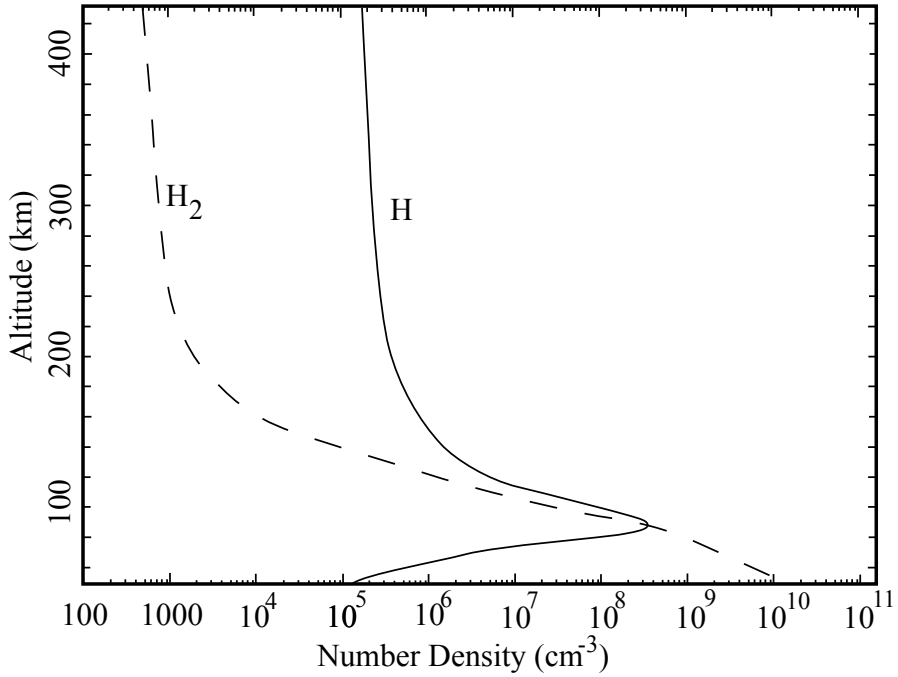

Figure 6.21: Sample profile of the H and H_2 densities as a function of altitude. Adapted from *Schunk and Nagy* [2000]

A second possibility for H^+ ions is the charge exchange of O^+ ions with neutral H atoms,

$$H + O^+ \rightleftharpoons H^+ + O. \tag{6.14}$$

This ionization mechanism is understood to be the main source of H^+ in the upper ionosphere (altitude of 600–1500 km) [*Schunk and Nagy*, 2000]. During active geomagnetic periods, when a significant population of secondary O^+ ions is created from primary electron precipitation, the population of H^+ can be enhanced by charge exchange. Similar charge exchange between precipitating O^+ ions and ionospheric

H will also contribute to the population of H^+.

Even though on first inspection one might predict that the suprathermal APS ions would be dominated by O^+, the ionosphere may be acting as a significant source of H^+. Therefore, the conclusions that the dominant species in the analyzed energy-dispersed signatures is O^+ for some events, while H^+ is the dominant species in other events, is consistent with the possibility of charge exchange with O^+ and with some direct H^+ production.

Chapter 7

Conclusions and suggestions for future research

7.1 Conclusions

Auroral precipitation is greatly enhanced and extremely structured in space and time during magnetically disturbed periods. A significant secondary population of thermal ions is created from the precipitation of electrons of auroral energies (1 to 10 keV). Since the dominant neutral atom at the ionization altitude of auroral electrons is oxygen, oxygen ions (O^+) are the dominant ion species created by electron precipitation. A significant population of protons (H^+) may also be created by the combination of auroral electron precipitation and the charge exchange between the enhanced population of oxygen ions and the ambient neutral hydrogen.

Numerous observations of outflowing ionospheric ions in the form of ion beams and ion conics have verified the presence of acceleration mechanisms capable of accelerating the thermal secondary ion population to suprathermal energies. Ions of suprathermal energies that escape the ionosphere and bounce along the magnetic field lines within the magnetosphere are termed auroral post-secondary (APS) ions. Because the curvature-gradient drift is negligible at suprathermal energies, these APS ions are bound to the magnetic flux tubes on which they are produced. These flux tubes convect at the $\vec{E}\times\vec{B}$ drift velocity, and therefore, the actual motion of the ions consists of their gyromotion around the magnetic field line, the bounce motion parallel to the magnetic field, and the $\vec{E}\times\vec{B}$ drift perpendicular to the magnetic field.

By monitoring the $\vec{E}\times\vec{B}$ drift within the ionosphere, one can map out the iono-

spheric footprint of the motion of magnetic flux tubes. This ionospheric convection map can include the westward subauroral flow enhancement called the subauroral polarization stream (SAPS), which appears as an extension of the afternoon convection cell. This flow distortion is consistent with existing radar observations and convection models. After auroral secondary ions are created and accelerated within the auroral zone, the $\vec{E}\times\vec{B}$ convective drift will transport these bouncing and drifting ions through the auroral zone and into the SAPS region. This is especially relevant for O^+ ions, as they have a bounce period sufficiently long to transport the O^+ ions into the SAPS region during a single half-bounce. Precipitation of these ions within the SAPS region at altitudes of 200–350 km may contribute to the enhanced occurrence of radar echoes observed in the SAPS region ionosphere.

Akebono and DMSP satellite data of suprathermal ions in the magnetospheric regions mapping to the low-latitude auroral oval and the SAPS region exhibit bands of enhanced flux. The energy of these suprathermal ion bands increases with increasing latitude. The present work examines the hypothesis that these suprathermal ion bands are the result of secondary ionospheric ions that have been created and accelerated out of the auroral zone in a time period comparable to the short time scales of intense auroral electron precipitation. A short acceleration duration implies that the dominant dispersion mechanism of suprathermal ions is the time of flight (TOF) mechanism. According to the TOF mechanism, a large cluster of ions with a broad energy distribution over a finite range of magnetic L shells produces a latitudinal energy dispersion because the high energy ions on the longer field lines will arrive at the observing altitude of a satellite in the opposite hemisphere at the same time as the lower energy ions on the shorter field-lines. A satellite moving across this region in which the ions are precipitating observes higher ion energies at higher latitudes.

Data from three sets of energy-dispersed ion observations were examined in detail to test the short-lived ionospheric acceleration hypothesis. The first two events, measured onboard the Akebono satellite, illustrated distinct multiple bands of energy-dispersed ions. The bands were consistent with the multiple-bounce banding mechanism, in which the lowest energy ion band was due to ions traveling a single half-

bounce from the source region, and the higher energy bands were due to ions traveling 3, 5, and 7 half-bounces. The high and low energies of the ion dispersion bands were used to estimate the drift-bounce time, namely the travel time between the ion source and the observer. While the dependence of the half-bounce time on both the length of the field line and the velocity of the ion are the only factors that lead to energy dispersion of bouncing ions, one must also account for the delays introduced in the data due to the transit time of the observing satellite across the dispersed ion feature. In the two Akebono events, the poleward and the equatorward drift-bounce times agreed well with the expected TOF dispersion, if one assumed that the ions were H^+. Akebono mass spectrometer measurements for the second event supported this assumption because they indicated that H^+ was the dominant suprathermal ion species (the dominant species for the first event was undetermined). Therefore, the short-lived ionospheric acceleration model was deemed able to account for the magnitude of the observed energy dispersion.

Data from the DMSP F12 satellite for the third event included a well-defined energy-dispersed ion signature located within the SAPS region. To determine if the short-lived ionospheric acceleration model could account for the magnitude of the observed energy-dispersion, three-dimensional ion tracing software was developed to more accurately model the motion of ions drift-bouncing from the auroral zone source equatorward into the SAPS region. This software accounted for the dependence of the half-bounce time on the length of the field line. As ions drift equatorward to lower latitudes, the length of the flux tube on which the ion is bouncing decreases, which shortens the half-bounce time. The results of the particle tracing showed that the short-lived ionospheric acceleration model could account for the magnitude of the energy-dispersion of the ion signature observed in the SAPS region if one allows for the existence of small field-aligned potentials ($\sim$ 100 V). Such field-aligned potentials are comparable to those employed by *Boehm et al.* [1999] in their study of energy-dispersed ion signatures, and are less than the observations of $\sim$ 800 V field aligned electric potentials reported by *Andersson et al.* [2002]. The ion species for this event was determined to be O^+ since the bounce time of H^+ is too short to allow for

the transport of the ions from the estimated acceleration region in the auroral zone equatorward to the latitudes where the ions were observed.

7.2 Suggestions for future research

The present work employed a three-dimensional ion tracing program capable of demonstrating that the short-lived ionospheric acceleration model could account for the energy-dispersed ion signature that was observed in the SAPS region on April 6, 2000. It was also used successfully to reproduce the multiple bands of energy-dispersed signatures observed by the Akebono satellite on December 21, 1989. However, the modelling of ion motion in the magnetosphere is an extremely broad and very complex subject. It involves incorporating an accurate magnetic field line model and realistic electric field distributions. It also requires a comprehensive understanding of the spatial and temporal variability and characteristics of ion acceleration mechanisms. Such complexity in ion modelling exceeded the scope of this project and the ion tracing software developed for this thesis made a number of simplifying assumptions in order to accomplish the first order calculations of the drift-bounce motion. These assumptions can be improved upon for future research. For example, one could adopt a complex magnetic field line model such as the Tsyganenko 96 magnetic field line model [*Tsyganenko and Stern*, 1996] in place of the dipole magnetic field used. The Tsyganenko 96 model provides a much more realistic description of Earth's magnetic field, and would greatly enhance the accuracy of the drift-bounce trajectories. With the aid of new mid-latitude SuperDARN radars, detailed convection maps that account for the subauroral flows could be used to provide actual convection maps that could be modelled for more accurate comparisons to observations. Also, because of the step-wise design of the ion tracing software, one can modify the software to incorporate field-aligned electric fields with temporal and spatial variability. Such modified programs would more effectively model the field aligned potentials that have been measured with satellite electric field instruments (e.g., *Andersson et al.* [2002], *Mozer and Kletzing* [1998]).

DMSP observations presented in Chapter 5 highlighted that the suprathermal secondary ions resulting from primary auroral precipitation have large enough number density and energy flux to contribute significantly to the dynamics of the disturbed magnetosphere-ionosphere system. This is especially true for those ions on flux tubes that have convected initially in the magnetospheric region that maps down to the auroral zone and subsequently into the SAPS region where the suprathermal particles are the primary population of precipitating ions. Suprathermal ions in the SAPS region have been recorded frequently by DMSP spectrometers, but there have been no direct measurements of the ion mass of the subauroral suprathermal ions. The Canadian Enhanced Polar Outflow Probe (e-POP) is scheduled to launch as a scientific payload on the CASSIOPE small satellite in 2007 [*Yau et al.*, 2006]. This satellite will be launched into a low-altitude, elliptical polar orbit (inclination of 80°) with an apogee and perigee of 325 km and 1500 km, respectively. One of the primary objectives of this mission is to study the outflow of plasma from the polar regions. To aid this objective, the e-POP instrument payload includes an imaging and rapid-scan mass spectrometer (IRM), which measures two-dimensional velocity distributions of ions with energies ranging from 0.5 to 100 eV with 10 ms resolution. This mission will provide invaluable observations to better characterize the outflowing ion populations.

Multi-instrument statistical studies, such as analyses of combined DMSP and e-POP data, will be very useful in the determination of characteristics of suprathermal ions in the auroral and SAPS regions. There is potential to examine the occurrence statistics of suprathermal ions within SAPS to examine the dependence of these suprathermal ions on magnetospheric conditions (Kp and D_{st} indices). An example of such a study is to examine the relationship between upward flowing O^+ and H^+ ions observed with e-POP and the precipitating ion flux observed with DMSP. One could also combine the e-POP and DMSP particle data with ground-based and satellite optical data (such as the TIMED Global Ultraviolet Imager (GUVI) data [*Christensen et al.*, 2003]) that provide excellent spatial and temporal observations of the very dynamic and structured electron precipitation. This would be extremely

useful in defining the boundaries of the auroral zone and for furthering the understanding of the suprathermal ion production.

Appendix A

Geomagnetic indices and observational equipment

A.1 Kp index

Magnetometers have been used to measure geomagnetic activity for many years. The Kp index or planetary index, described by *Bartels* [1957], is a measure of the magnetic disturbance due to the effects of variations in the magnetic field. This index is calculated as the arithmetic average of the station index, Ks, from 13 standard magnetic observatories [*Kivelson and Russell*, 1995]. To calculate Ks, first the regular magnetic field variations are subtracted from the raw magnetometer data. The data are then divided into three-hour intervals, and the peak to peak disturbance is converted from the measured scale (in gammas) to a quasi-logarithmic scale ranging from 0 to 9 in steps of 1/3. This scale is seen written as follows: $0^0, 0^+, 1^-, 1^0, 1^+, 2^-, \ldots, 9^-, 9^0$ (for a full discussion on the choice of range scaling see *Mayaud* [1980]). Higher Kp readings denote greater magnetic disturbance. For example, a Kp value of 2^- is considered a "quiet" period with little magnetic disturbance. A Kp above 3^- is considered magnetically disturbed. An event with a Kp greater than 7^- is extremely disturbed and quite rare.

A.2 D_{st} index

During a magnetic storm, there is a huge increase in the number of charged particles injected into the tail region. These particles drift sunward toward the Earth and, due to the curvature-gradient drift, ions drift westward and electrons drift eastward around the Earth. This charge-separating drift creates a current that encircles the Earth and that is localized near the equatorial plane roughly at radial distances of

3 to 5 R_E. This current is called the ring current. The magnetic field created by this current causes a negative H or southward perturbation of the surface magnetic field at low latitudes of the Earth. The measure of the perturbation of the magnetic field at the equator is the disturbance storm time index or D_{st} [*McPherron*, 1995]. Note that the strength of the ring current and the magnetic field perturbation of the ring current are directly linked to the strength of the magnetic storm. Therefore, the D_{st} index is a measure of the strength of the ring current and the strength of the magnetic storm.

The D_{st} index is based on the measurements of the southward perturbation of the magnetic field from four low latitude magnetometers. To calculate the D_{st} index, first the quiet-time horizontal (north-south) magnetic field is subtracted from the raw data. To approximate the actual magnetic fluctuation at the equator, the corrected amplitude of the magnetic perturbation is divided by the cosine of the magnetic latitude of the magnetometer station. The D_{st} index is the average of the adjusted magnetic perturbations from the four stations. The D_{st} index is recorded in nanoteslas (nT). Typical magnetic storms will have a D_{st} between -50 and -150 nT but storms with a D_{st} dropping below -500 nT have been recorded [*McPherron*, 1995].

A.3 Observational instruments

The Defense Meteorological Satellite Program (DMSP) satellites are in a low-altitude ($\sim$840 km), nearly-circular polar orbit. The orbital plane is inclined to 98.7°, which keeps the craft in a sun-synchronous orbit in either a 0600 to 1800 LT or a 1030 to 2230 LT meridian plane. The satellites are three-axis stabilized with the X-axis pointing in the nadir, the Y-axis pointing parallel or anti-parallel to the satellite velocity and the Z-axis perpendicular to the orbital plane with positive direction on the sunward side of the orbital plane [*Greenspan et al.*, 1986]

Each satellite is equipped with a Special Sensor Precipitating Electron and Ion Spectrometer (SSJ/4) [*Hardy et al.*, 1984]. This instrument consists of two pairs of

cylindrical curved plate electrostatic analyzers, one for measuring ions and one for electrons. One analyzer in each pair measures the charged particles in ten channels spread logarithmically from 30 to 1000 eV. The other analyzer in each pair measures the charged particles in ten channels spread logarithmically from 1 to 30 keV. With one overlapping channel, the result is a 19-channel spectrograph measuring ion and electron flux in the energy ranging from 30 eV to 30 keV. The SSJ/4 detector is mounted so that the aperture is pointed in the negative-X direction (zenith). For the low altitude orbit of DMSP, the detector is capable of viewing only ions and electrons precipitating well within the atmospheric loss cone as the satellite travels through the auroral and subauroral latitudes.

A schematic of a curved plate analyzer is illustrated in Figure A.1. The analyzers operate by applying a voltage across the curved plates, which is directed inward for the ion analyzer and outward for the electron analyzer. When an ion (or electron) has a velocity such that the centrifugal force balances the electric force applied around the curve, the ion reaches the detector channeltron. Varying the voltage between the curved plates allows the detector to sample each of the ten different energy channels. Note that the angles subtended by the curved plates for the analyzers measuring the high and low energy charged particles are 60° and 130°, respectively.

Also onboard each DMSP satellite is a Special Sensor Ion and Electron Scintillation Monitor (SSIES) [*Greenspan et al.*, 1986]. This sensor is actually a collection of four instruments: an ion drift meter, a retarding potential analyzer (RPA), an ion scintillation monitor and a Langmuir probe (LP). The ion drift meter measures the thermal plasma flow in the plane perpendicular to the velocity of the satellite. It consists of four collector plates mounted with the aperture pointing in the direction of the velocity vector. As the satellite orbits the Earth, the ion drift meter acts as an ion bucket, sampling the thermal plasma along the orbital path. The horizontal (vertical) speed of the ion is calculated from the difference in current between the left and right (bottom and top) collectors. The ion drift velocity parallel to the satellite velocity is available through the use of the RPA. The RPA aperture also faces in the direction of the satellite velocity to collect thermal ions. The retarding potential is

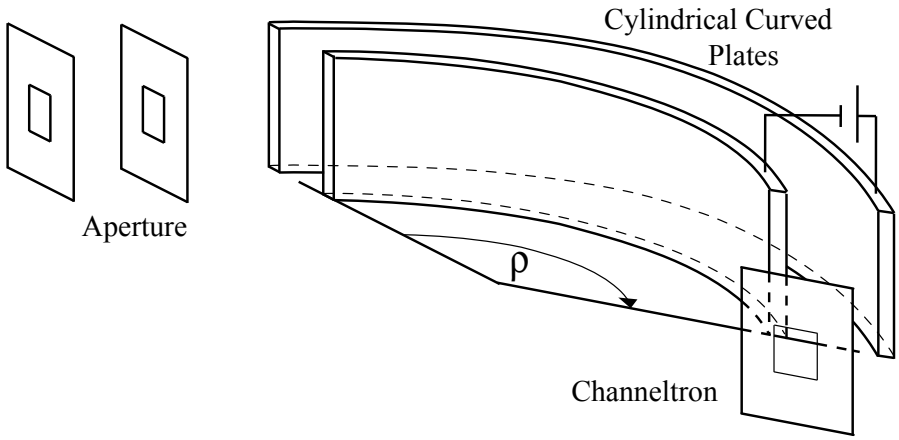

Figure A.1: Configuration of the curved plate analyzer with a radius of curvature of 130°, which corresponds to the detector measuring ions in the low energy range from 30 to 1000 eV. Adapted from *Hardy et al.* [1984].

swept through a range of voltages and the current incident on the collector plate is recorded. The ion velocity (parallel to satellite track) is deduced from comparisons of the current versus voltage data with theoretical current-voltage plots.

The Akebono (EXOS-D) satellite was launched in an elliptical orbit with a 75° inclination and with an apogee and perigee of 10,500 km and 274 km respectively [*Oya and Tsuruda*, 1990]. It is spin stabilized such that the axis of the spin is pointed directly at the sun (for maximum power from solar panels) and has a spin rate of 7.5 revolutions-per-minute.

Onboard Akebono is the Low Energy Particle (LEP) instrument which is composed of two energy-per-charge (E/Q) analyzers (LEP-S1, LEP-S2) and one energetic ion mass-spectrometer (LEP-M or IMS) [*Mukai et al.*, 1990]. LEP-S1 and LEP-S2 are identical detectors with 5 pairs of channeltrons each. For each pair, one analyzer is designed for electrons and the other for ions. Each pair of channeltrons are spaced at 60°, 90°, 120°, and 180° from the spin axis each with approximately a 7° by 9° field of view (see Figure A.2). The energy range of the analyzers is 10 eV to 16 keV for electrons and 13 eV/q to 20 keV/q for ions and is divided into 29 logarithmically spaced steps [*Hirahara et al.*, 1997a]. The energy resolution $\Delta\ E/E$ of the LEP in-

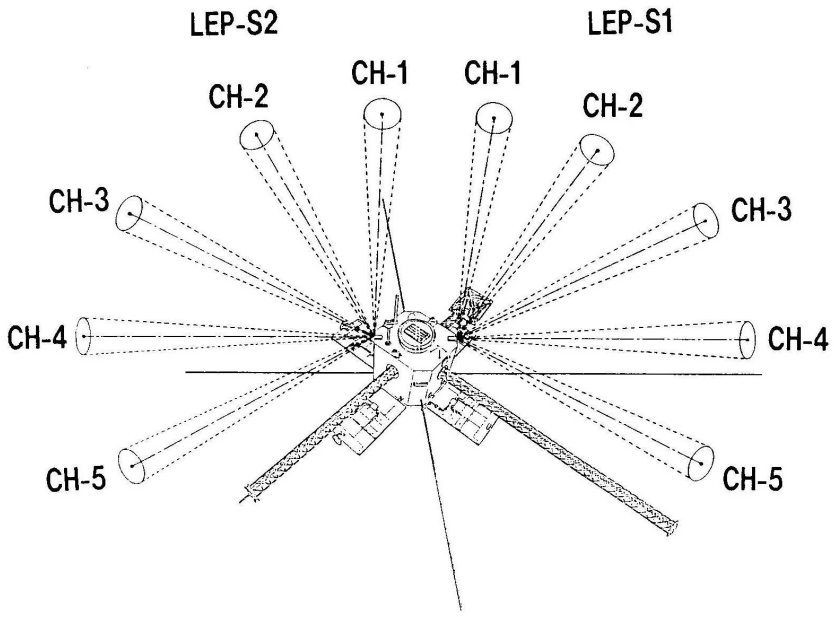

Figure A.2: Schematic drawing of the fields of view of the LEP-S1 and LEP-S2. From *Mukai et al.* [1990].

struments is $\sim 12\%$. The spin of the satellite allows observations at all pitch angles.

The IMS measures the energy spectra for the ion species H^+, He^+, and O^+ [*Kayay et al.*, 1990]. The energy range is 300 eV/q to 25 keV/q and is divided into 32 logarithmically spaced steps. The instrument points perpendicular to the spin axis with a field of view of 3° by 34°. In addition to the IMS, Akebono also has onboard a suprathermal mass spectrometer (SMS), which has an optimum response in the thermal (0 to 25 eV) and suprathermal (25 eV to 3 keV) energy ranges [*Whalen et al.*, 1990].

Both the Akebono and the DMSP satellite programs have advantageous features. DMSP is a long-running program in which at least two satellites are operational at all times. Their near-circular, low-altitude orbits provide continuous tracers of ionospheric convection. They provide excellent sampling of the precipitating ion and electron flux over a broad energy range, and ions over a larger pitch angle range. DMSP, however, measures only precipitating ions and electrons, with the exception

of the most recent DMSP satellites, which operate a new SSJ/5 detector that is capable of sampling in six 15° pitch angle sectors from zenith to horizon [*Kadinsky-Cade et al.*, 2004]. Also, DMSP has no method of directly measuring ion mass. Akebono provides a more densely sampled data set of particle fluxes at all pitch angles, with the mass spectrometers (IMS and SMS) is capable of providing mass composition measurements of the three main ion populations (H^+, He^+, O^+).

Appendix B

Derivation of the bounce period and the bounce-average curvature-gradient drift

B.1 Bounce period in a dipole magnetic field

The period of the bounce motion of a charged particle is calculated by integrating the incremental displacement along the magnetic field line, $ds_\parallel$, divided by the parallel velocity, $v_\parallel$, over one complete bounce,

$$T_{\text{bounce}} = \oint \frac{ds_\parallel}{v_\parallel}. \tag{B.1}$$

In a dipole magnetic field, $ds_\parallel$ is related to the equatorial distance to the field line, r_0, and the latitude of the particle, θ, in the equation

$$ds_\parallel = r_0 \cos\theta \sqrt{1 + 3\sin^2\theta} d\theta. \tag{B.2}$$

The parallel velocity, $v_\parallel$, is given by

$$v_\parallel = v \cos\alpha, \tag{B.3}$$

where α, known as the pitch angle, is defined as the angle between the particle velocity, $\vec{v}$, and the magnetic field, $\vec{B}$. Using the first adiabatic invariant, μ, given by the equation

$$\mu = \frac{K_\perp}{B} = \frac{m v_\perp^2}{2B} = \frac{m v^2 \sin^2\alpha}{2B}, \tag{B.4}$$

one can relate the pitch angle to the equatorial values of the pitch angle and magnetic field with the equation

$$\sin^2\alpha = \sin^2\alpha_0 \frac{B}{B_0}. \tag{B.5}$$

Using the trigonometric relation

$$\cos\alpha = \sqrt{1 - \sin^2\alpha}, \tag{B.6}$$

and the relation for B/B_0 from the equation of a dipole field

$$\frac{B}{B_0} = \frac{\sqrt{1+3\sin^2\theta}}{\cos^6\theta}, \tag{B.7}$$

one can obtain the equation for $v_\parallel$ as a function of θ,

$$v_\parallel = v\sqrt{1-\frac{\sin^2\alpha_0\sqrt{1+3\sin^2\theta}}{\cos^6\theta}}. \tag{B.8}$$

Substituting Equation B.8 into Equation B.1 gives the full-integral bounce period equation,

$$T_{\text{bounce}} = \frac{4r_0}{v}\int_{\theta=0}^{\theta_m}\frac{\cos\theta\sqrt{1+3\sin^2\theta}}{\sqrt{1-\frac{\sin^2\alpha_0\sqrt{1+3\sin^2\theta}}{\cos^6\theta}}}d\theta, \tag{B.9}$$

where the limits of the integral define one quarter-bounce from equatorial plane, $\theta = 0$, to the mirror latitude, $\theta = \theta_m$.

The integral in Equation B.9 is sometimes referred to as the bounce-integral and must be solved numerically. However, *Hamlin et al.* [1961] has shown that the bounce-integral can be effectively approximated by

$$I(\alpha_0) \simeq 1.30 - 0.56\sin\alpha_0, \tag{B.10}$$

and so the Hamlin approximation for the bounce period of charged particles in a dipole magnetic field simplifies to

$$T_{\text{bounce}} = \frac{4r_0}{v}I(\alpha_0) \simeq \frac{4r_0}{v}(1.30 - 0.56\sin\alpha_0). \tag{B.11}$$

B.2 Bounce-averaged curvature-gradient drift

The assumption that space plasma is "frozen" to the convecting magnetic field requires that the drift effect of the curvature-gradient drift, $\vec{v}_{cg}$, is negligible compared to the $\vec{E}\times\vec{B}$ drift. From Section 2.1 the $\vec{v}_{cg}$ was shown to be dependent on the particle parallel and perpendicular kinetic energy, $K_\perp$ and $K_\parallel$ in the equation

$$\vec{v}_{cg} = \frac{K_\perp + 2K_\parallel}{qB^3}(\vec{B}\times\nabla_\perp B), \tag{B.12}$$

where q is the charge and $\vec{B}$ is the magnetic field. Although the direction of $\vec{v}_{cg}$, determined by the term $\vec{B} \times \nabla_{\perp} B$, is directed in the $\hat{\phi}_{west}$ direction at all points along the dipole magnetic field lines, the magnitude of this quantity is function of the latitude. Therefore, to compare the relative contribution of the $\vec{v}_{cg}$ to the total plasma drift with that of the $\vec{E} \times \vec{B}$ drift, one must calculate the curvature-gradient drift averaged over one complete bounce-period.

The bounce-averaged curvature-gradient, $\bar{v}_{cg}$, is given by

$$\bar{v}_{cg} = \bar{w} r_0, \tag{B.13}$$

where r_0 is the equatorial distance to the magnetic field line and $\bar{w}$ is the angular velocity averaged over one bounce period. The equation for $\bar{w}$ is

$$\bar{w} = \frac{1}{T_{\text{bounce}}} \int_{t=0}^{T_{\text{bounce}}} \left(\frac{d\phi}{dt} \right) dt, \tag{B.14}$$

where $d\phi$ is the incremental angular displacement in the $\hat{\phi}$ direction. $d\phi$ can be written in terms of the incremental arc length, dS_{az} (az denotes azimuthal), with the equation

$$d\phi = \frac{dS_{az}}{r \cos\theta}. \tag{B.15}$$

By substituting Equation B.15 into Equation B.14, $\bar{w}$ becomes

$$\bar{w} = \frac{1}{T_{\text{bounce}}} \int_{t=0}^{T_{\text{bounce}}} \left(\frac{1}{r \cos\theta} \right) \left(\frac{dS_{az}}{dt} \right) dt. \tag{B.16}$$

Using the substitution,

$$dt = \frac{d_{\parallel}}{v_{\parallel}}, \tag{B.17}$$

and inserting v_{cg} for dS_{az}/dt, Equation B.16 can be written as

$$\bar{w} = \frac{4}{T_{\text{bounce}}} \int_{\theta=0}^{\theta_{\text{mirror}}} \frac{v_{cg}}{r \cos\theta} \frac{d_{\parallel}(\theta)}{v_{\parallel}(\theta)}, \tag{B.18}$$

where $d_{\parallel}(d\theta)$ are found in Appendix B.1 and only v_{cg} is yet to be derived as a function of θ.

To derive $\vec{v}_{cg}$ as a function of θ in a dipole magnetic field, one can use the set of equations defining the parallel and perpendicular kinetic energy given here,

$$K_{\perp} = \frac{m v_{\perp}^2}{2} \;=\; \frac{m v^2 \sin^2\alpha}{2}, \tag{B.19}$$

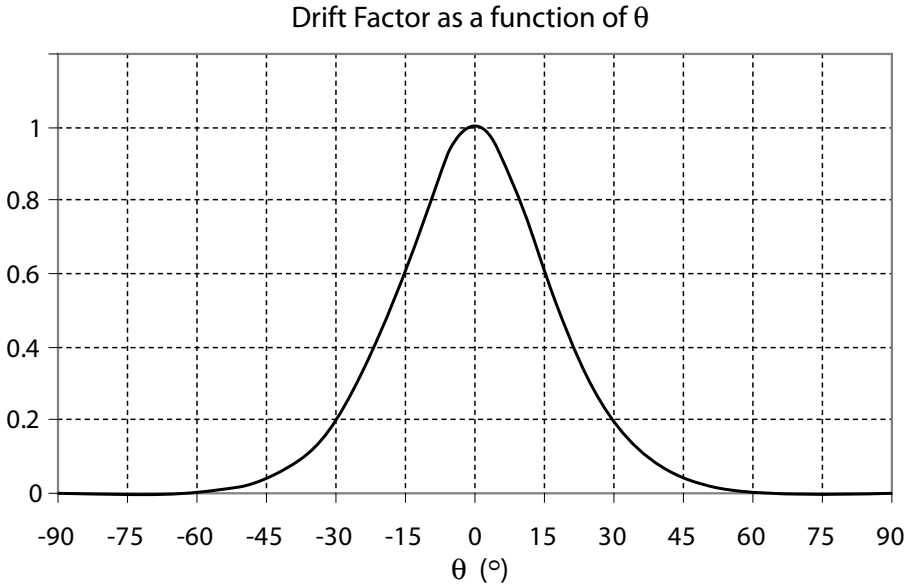

Figure B.1: The drift factor as a function of latitude.

$$K_{\parallel} = \frac{mv_{\parallel}^2}{2} \;=\; \frac{mv^2\cos^2\alpha}{2}, \tag{B.20}$$

to collect a common factor of the total kinetic energy from Equation B.13, and v_{cg} simplifies to,

$$\vec{v}_{cg} = \frac{K}{qB^3}(1+\cos^2\alpha)[\vec{B}\times\nabla_{\perp}B]. \tag{B.21}$$

After substituting the equation of a dipole magnetic field for $\vec{B}$ and performing the cross product, this equation becomes

$$\vec{v}_{cg} = \frac{3K}{qB_0r_0}(1+\cos^2\alpha)\left[\frac{\cos^5\theta(1+\sin^2\theta)}{(1+3\sin^2\theta)^2}\right]\hat{\phi}_{west}. \tag{B.22}$$

The term in the square brackets is known as the drift factor [*Lyons and Williams*, 1984]. Figure B.1 illustrates a plot of the drift factor for θ ranging from $-90°$ to $90°$. Note that this term quickly drops off to zero for θ greater than $45°$ degrees, and is less than 0.2 for θ greater than $30°$. Therefore, the majority of the drift due to v_{cg} occurs during the portion of the particle bounce motion when the particle is within $30°$ of the equatorial plane.

By extracting the relation between $\cos\alpha$ and the equatorial pitch angle α_0 from

Equation B.8,

$$\cos\alpha = \sqrt{1 - \frac{\sin^2\alpha_0\sqrt{1+3\sin^2\theta}}{\cos^6\theta}}, \tag{B.23}$$

v_{cg} becomes

$$\vec{v}_{cg} = \frac{6K}{qB_0r_0}\left(1 - \frac{\sin^2\alpha_0\sqrt{1+3\sin^2\theta}}{2\cos^6\theta}\right)\left[\frac{\cos^5\theta(1+\sin^2\theta)}{(1+3\sin^2\theta)^2}\right]\hat{\phi}_{west}. \tag{B.24}$$

When combining this relation for v_{cg} with Equations B.2 and B.8, $\bar{w}$ becomes

$$\bar{w} = \frac{6K}{qB_0r_0v}\frac{4}{T_{\text{bounce}}}\int_{\theta=0}^{\theta_{\text{mirror}}} \frac{\cos^3\theta(1+\sin^2\theta)\left(1 - \frac{\sin^2\alpha_0\sqrt{1+3\sin^2\theta}}{2\cos^6\theta}\right)}{(1+3\sin^2\theta)^{3/2}\sqrt{1 - \frac{\sin^2\alpha_0\sqrt{1+3\sin^2\theta}}{\cos^6\theta}}}d\theta, \tag{B.25}$$

where the integral is more simply denoted by $Q(\alpha_0)$. After substituting the equation of the bounce period (Equation B.11) into Equation B.25, $\bar{w}$ may be written as

$$\bar{w} = \frac{6K}{qB_0r_0^2}\frac{Q(\alpha_0)}{I(\alpha_0)}. \tag{B.26}$$

Similar to the approximation for $I(\alpha_0)$, *Hamlin et al.* [1961] illustrated that a reasonable approximation for the term $Q(\alpha_0)/I(\alpha_0)$ is

$$\frac{Q(\alpha_0)}{I(\alpha_0)} \simeq 0.35 + 0.15\sin\alpha_0, \tag{B.27}$$

and so the equation for the bounce-averaged curvature gradient drift simplifies to

$$\bar{v}_{cg} = \frac{6K}{qB_0r_0}\frac{Q(\alpha_0)}{I(\alpha_0)} \simeq \frac{6K}{qB_0r_0}(0.35 + 0.15\sin\alpha_0). \tag{B.28}$$

Using Equation B.28 to calculate the bounce-averaged curvature-gradient drift, the change in longitude per time, $d\phi/dt$, due to $\bar{v}_{cg}$ is plotted in Figure B.2 as a function of energy. For this plot it was assumed that the drift-bounce motion occurs on the L = 6 magnetic dipole shell and that the mirror altitude is 100 km. The plot also provides $d\phi/dt$ due to purely longitudinal $\vec{E}\times\vec{B}$ drifts of 100 m/s and 500 m/s, measured at an altitude of 840 km. This plot illustrates that the drift in longitude due to $\bar{v}_{cg}$ is much smaller than the $\vec{E}\times\vec{B}$ drift for particles energies less than 2 keV when the $\vec{E}\times\vec{B}$ drift (measured at an altitude of 840 km) is greater than 500 m/s. For a low $\vec{E}\times\vec{B}$ drift of only 100 m/s the effect of the bounce-averaged curvature-gradient drift is negligible for ions of energies up to ∼400 eV.

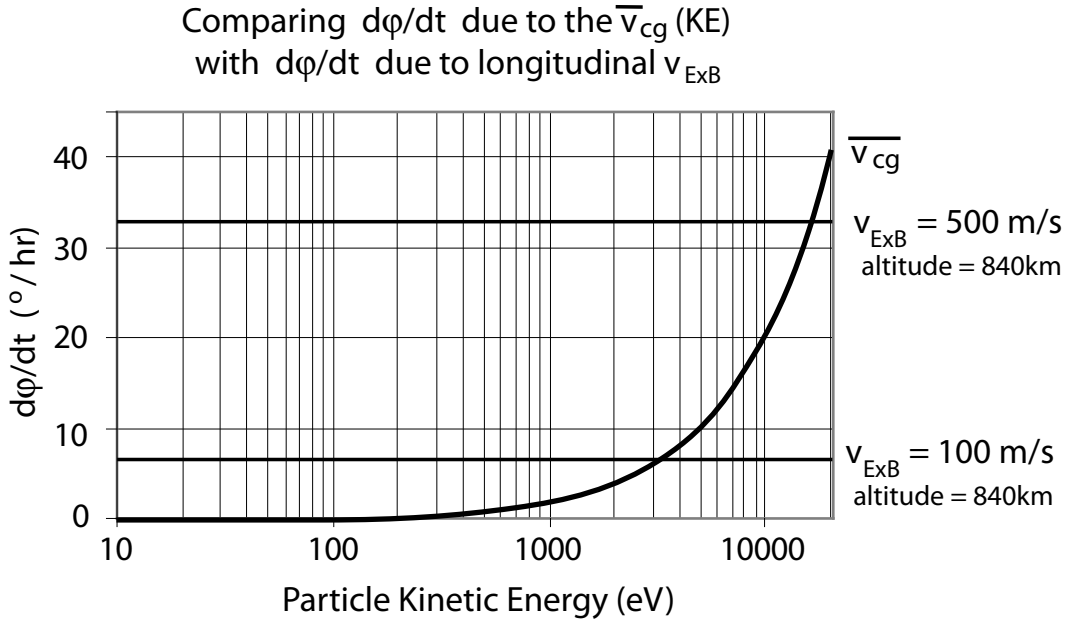

Figure B.2: Comparison of the change in longitude per time due to the bounce-averaged curvature-gradient drift with that due to a longitudinal $\vec{E}\times\vec{B}$ drift of 100 m/s and 500 m/s measured at an altitude of 840 km. The drift-bounce motion is assumed to occur on the L=6 shell with a mirror altitude of 100 km.

References

Akasofu, S.-I., The development of the auroral substorm, *Planetary and Space Science*, *12*, 273–282, 1964.

Andersson, L., R. E. Ergun, D. L. Newman, J. P. McFadden, C. W. Carlson, and Y.-J. Su, Characteristics of parallel electric fields in the downward current region of the aurora, *Physics of Plasmas*, *9*, 3600–3609, 2002.

Bartels, J., Solar influences on geomagnetism, *The Proceedings of the National Academy of Sciences of the United States of America*, *43*, 75–81, 1957.

Baumjohann, W., and R. A. Treumann, *Basic Space Plasma Physics*, Imperial College Press, 1996.

Boehm, M. H., D. M. Klumpar, E. Möbius, L. M. Kistler, J. P. McFadden, C. W. Carlson, and R. E. Ergun, Fast auroral snapshot observations of bouncing ion distributions: Fieldline length measurements, *Journal of Geophysical Research*, *104*, 2343–2355, 1999.

Burch, J. L., P. H. Reiff, R. A. Heelis, J. D. Winningham, W. B. Hanson, C. Gurgiolo, J. D. Menietti, R. A. Hoffman, and J. N. Barfield, Plasma injection and transport in the mid-altitude polar cusp, *Geophysical Research Letters*, *9*, 921–924, 1982.

Carlson, H. C., Jr., and A. Egeland, *Introduction to Space Physics*, chap. 14, pp. 459–502, Cambridge University Press, 1995.

Christensen, A. B., et al., Initial observations with the Global Ultraviolet Imager (GUVI) in the NASA TIMED satellite mission, *Journal of Geophysical Research*, *108*(A12), 1451, doi:10.1029/2003JA009918, 2003.

Cowley, S. W. H., The Earth's magnetosphere: A brief beginner's guide, *EOS Transactions*, *76*, 525–525, 1995.

Foster, J. C., and W. J. Burke, SAPS: A new characterization for subauroral electric fields, *EOS Trans. AGU*, 2002.

Foster, J. C., and A. J. Coster, Conjugate localized enhancement of TEC at low latitudes in the American sector, *Journal of Atmospheric and Solar-Terrestrial Physics*, in press, 2007.

Foster, J. C., and H. B. Vo, Average characteristics and activity dependence of the subauroral polarization stream, *Journal of Geophysical Research*, *107*(A12), 1475-1485, doi:10.1029/2002JA009409, 2002.

Frahm, R. A., P. H. Reiff, J. D. Winningham, and J. L. Burch, Banded ion morphology: Main and recovery storm phases, in *Ion Acceleration in the Magnetosphere and Ionosphere*, edited by T. Chang, M. K. Hudson, J. R. Jasperse, R. G. Johnson, P. M. Kintner, and M. Schulz, vol. 38 of *Geophysical Mongraph Series*, pp. 98–107, American Geophysical Union, Washing, D. C., 1986.

Galperin, Y. I., V. N. Ponomarev, and A. G. Zosimova, Plasma convection in polar ionosphere, *Annales de Geophysique*, *30*, 1–7, 1974.

Glatzmaier, G. A., and P. H. Roberts, A three-dimensional convective dynamo solution with rotating and finitely conducting inner core and mantle, *Physics of the Earth and Planetary Interiors*, *91*, 63–75, 1995.

Greenspan, M. E., P. B. Anderson, and J. M. Pelagatti, Characteristics of the thermal plasma monitor (SSIES) for the Defense Meteorological Satellite Program (DMSP) spacecraft F8 through F10, *Tech. Rep. AFGL-TR-86-0227*, Air Force Geophys. Lab., Hanscom Air Force Base, Mass., 1986.

Greenwald, R. A., et al., Darn/Superdarn: A Global View of the Dynamics of High-Lattitude Convection, *Space Science Reviews*, *71*, 761–796, 1995.

Gustaffson, G., A revised corrected geomagnetic coordinate system, *Arkiv för Geophysik*, *5*, 1970.

Hamlin, D. A., R. Karplus, R. C. Vik, and K. M. Watson, Mirror and azimuthal drift frequencies for geomagnetically trapped particles, *Journal of Geophysical Research*, *66*, 1961.

Hardy, D. A., L. K. Schmitt, M. S. Gussenhoven, F. J. Marshall, H. C. Yeh, T. L. Shumaker, A. Hube, and J. Pantazis, Precipitating electron and ion detectors (SSJ/4) for the block 5D/flights 6-10 DMSP satellites: Calibration and data presentation, *Tech. Rep. AFGL-TR-84-0317*, Air Force Geophys. Lab., Hanscom Air Force Base, Mass., 1984.

Hargreaves, J. K., *The solar-terrestrial environment*, Cambridge University Press, 1992.

Heppner, J. P., and N. C. Maynard, Empirical high-latitude electric field models, *Joural of Geophysical Research*, *92*, 4467–4489, 1987.

Hess, W. N., *The Radiation Belt and Magnetosphere*, chap. 2, pp. 23–67, Blaisdell Publishing Company, 1968.

Hirahara, M., T. Mukai, N. Kaya, and H. Hayakawa, Multiple energy-dispersed ion precipitations in the low-latitude auroral oval: Evidence of ExB drift effect and upward flowing ion contribution, *Journal of Geophysical Research*, *102*, 2513–2530, 1997a.

Hirahara, M., A. Yamazaki, K. Seki, T. Mukai, E. Sagawa, N. Kaya, and H. Hayakawa, Characteristics of downward flowing ion energy dispersions observed in the low-altitude central plasma sheet by Akebono and DMSP, *Journal of Geophysical Research*, *102*, 4821–4839, 1997b.

Holzer, T. E., Interaction between the solar wind and the interstellar medium, *Annual review of astronomy and astrophysics*, *27*, 199–234, 1989.

Hughes, W. J., *Introduction to Space Physics*, chap. 9, pp. 227–287, Cambridge University Press, 1995.

Johnson, C. Y., Ion and neutral composition of the ionosphere, *Annals of the IQSY*, *5*, 1969.

Kadinsky-Cade, K., E. G. Holeman, J. McGarrity, F. J. Rich, W. F. Denig, W. J. Burke, and D. A. Hardy, First results from the SSJ5 precipitating particle sensor on DMSP F16: Simultaneous observations of keV and MeV particles during the 2003 Halloween storms, *EOS Trans. AGU, 85*(17), Joint Assembly Suppl., Abstract SH53A-03, 2004.

Kayay, N., T. Mukai, and E. Sagawa, Preliminary results from new type ion mass spectrometer onboard the Akebono (EXOS-D) satellite, *Journal of Geomagnetism and Geoelectricity*, *42*, 497–509, 1990.

Kivelson, M. G., and C. T. Russell, *Introduction to Space Physics*, Cambridge University Press, 1995.

Koustov, A. V., R. A. Drayton, R. A. Makarevich, K. A. McWilliams, J.-P. St-Maurice, T. Kikuchi, and H. U. Frey, Observations of high-velocity SAPS-like flows with the King Salmon SuperDARN radar, *Annales Geophysicae*, *24*, 1591–1608, 2006.

Lennartsson, W., and R. D. Sharp, A comparison of the 0.1-17 kev/e ion composition in the near equatorial magnetosphere between quiet and disturbed conditions, *Journal of Geophysical Research*, *87*, 6109–6120, 1982.

Lyatsky, W., A. Tan, and G. V. Khazanov, A simple analytical model for sub-auroral polarization stream (SAPS), *Geophysical Research Letters*, *33,* L19101, doi:10.1029/2006GL025949, 2006.

Lyons, L. R., and D. J. Williams, *Quantitative Aspects of Magnetospheric Physics*, D. Reidel Publishing Company, Dordrecht, Holland, 1984.

Mayaud, P., *Derivation, Meaning, and Use of Geomagnetic Indices*, American Geophysical Union, 1980.

McIlwain, C. E., Coordinates for mapping the distribution of magnetically trapped particles, *Journal of Geophysical Research*, *66*, 3681–3691, 1961.

McPherron, R. L., *Introduction to Space Physics*, chap. 13, pp. 400–458, Cambridge University Press, 1995.

Miyashita, Y., et al., Plasmoids observed in the near-Earth magnetotail at $X{\sim}{-}7$ R_E, *Journal of Geophysical Research*, *110*(A12214), doi:10.1029/2005JA011263, 2005.

Mozer, F. S., and C. A. Kletzing, Direct observations of large, quasi-static, parallel electric fields in the auroral acceleration region, *Geophysical Research Letters*, *25*, 1629–1632, 1998.

Mukai, T., et al., Low energy charged particle observations in the "auroral" magnetosphere: First results form the Akebono (EXOS-D) satellite, *Journal of Geomagnetism and Geoelectricity*, *42*, 4779–496, 1990.

Newell, P. T., Y. I. Galperin, and C.-I. Meng, Morphology of nightside precipitation, *Journal of Geophysical Research*, *101*, 10,737–10,748, 1996.

Nishida, A., Magnetic reconnection in the tail of the magnetosphere, *Advances in Space Research*, *10*, 135–144, 1990.

Nishida, A., T. Mukai, T. Yamamoto, and Y. Saito, GEOTAIL observations on the reconnection process in the distant tail in geomagnetically active times, *Geophysical Research Letters*, *22*, 2453–2456, 1995.

Northrop, T. G., *The Adiabatic Motion of Charged Particles*, Interscience, New York, 1963.

Oksavik, K., R. A. Greenwald, J. M. Ruohoniemi, M. R. Hairston, L. J. Paxton, J. B. H. Baker, J. W. Gjerloev, and R. J. Barnes, First observations of the temporal/spatial variation of the sub-auroral polarization stream from the superdarn wallops hf radar, *Geophysical Research Letters*, *33,* L12104, doi:10.1029/2006GL026256, 2006.

Oya, H., and K. Tsuruda, Introduction to the Akebono (EXOS-D) Satellite Observations, *Journal of Geomagnetism and Geoelectricity*, *42*, 367–370, 1990.

Quinn, J. M., and C. E. McIlwain, Bouncing ion clusters in the Earth's magnetosphere, *Journal of Geophysical Research*, *84*, 7365–7370, 1979.

Quinn, J. M., and D. J. Southwood, Observations of parallel ion energization in the equatorial region, *Journal of Geophysical Research*, *87*, 10 536–10 540, 1982.

Rees, M. H., On the interaction of auroral protons with the earth's atmosphere, *Planetary and Space Science*, *30*, 463–472, 1982.

Reiff, P. H., T. W. Hill, and J. L. Burch, Solar wind plasma injection at the dayside cusp, *Journal of Geophysical Research*, *82*, 479–491, 1977.

Rosenbauer, H., H. Gruenwaldt, M. D. Montgomery, G. Paschmann, and N. Sckopke, Helios 2 plasma observations in the distant polar magnetosphere: The plasma mantle, *Journal of Geophysical Research*, *80*, 2723, 1975.

Rowland, D. E., and J. R. Wygant, Dependence of the large-scale, inner magnetospheric electric field on geomagnetic activity, *Journal of Geophysical Research*, *103*, 14,959–14,964, 1998.

Russell, C. T., *Introduction to Space Physics*, chap. 1, pp. 1–26, Cambridge University Press, 1995.

Schunk, R. W., and A. F. Nagy, *Ionospheres: Physics, Plasma Physics and Chemistry*, chap. 8-11, pp. 216–365, Cambridge University Press, 2000.

Sergeev, V. A., E. M. Sazhina, and N. A. Tsyganenko, Pitch-angle scattering of energetic protons in the magnetotail current sheet as the dominant source of their isotropic precipitation into the nightside ionosphere, *Planetary and Space Science*, *31*, 1147–1155, 1983.

Shelley, E. G., R. D. Sharp, and R. G. Johnson, He^{++} and H^{+} flux measurements in the dayside cusp: Estimates of convection electric field, *Journal of Geophysical Research*, *81*, 2363–2370, 1976.

Skoug, R. M., J. T. Gosling, J. T. Steinberg, D. J. McComas, C. W. Smith, N. F. Ness, Q. Hu, and L. F. Burlaga, Extremely high speed solar wind: 29-30 October 2003, *Journal of Geophysical Research*, *109*, A09102, doi:10.1029/2004JA010494, 2004.

Sofko, G. J., and A. Walker, Electric field mapping in a dipole field - a tutorial overview, 2006 Annual SuperDARN workshop, Chincoteague, USA, 2006.

Sofko, G. J., R. D. Schwab, M. Watanabe, C.-S. Huang, and J. C. Foster, Auroral post-secondary ions from the nightside ionosphere in the inner magnetosphere, *Journal of Atmospheric and Solar-Terrestrial Physics*, in press, 2007.

Southwood, D. J., and R. A. Wolf, An assessment of the role of precipitation in magnetospheric convection, *Journal of Geophysical Research*, *83*, 5227–5232, 1978.

Spiro, R. R., R. A. Heelis, and W. B. Hanson, Rapid subauroral ion drifts observed by Atmospheric Explorer C, *Geophysical Research Letters*, *6*, 657–660, 1979.

Trondsen, T. S., and L. L. Cogger, High-resolution television observations of black aurora, *Journal of Geophysical Research*, *102*, 363–378, 1997.

Trondsen, T. S., and L. L. Cogger, A survey of small-scale spatially periodic distortions of auroral forms, *Journal of Geophysical Research*, *103*, 9405–9415, 1998.

Tsyganenko, N. A., and D. P. Stern, Modelling the global magnetic field of the large-scale Birkeland current system, *Journal of Geophysicsal Research*, *101*, 1749–1754, 1996.

Wahlund, J.-E., H. J. Opgenoorth, I. Häggström, K. J. Winser, and G. O. L. Jones, EISCAT observations of topside ionospheric ion outflows during auroral activity: Revisited, *Journal of Geophysical Research*, *97*, 3019–3037, 1992.

Whalen, B. A., et al., The Suprathermal Ion Mass Spectrometer (SMS) onboard the Akebono (EXOS-D) Satellite, *Journal of Geophysical Research*, *42*, 511–536, 1990.

Winningham, J. D., J. L. Burch, N. Eaker, V. A. Blevins, and R. A. Hoffman, The Low Altitude Plasma Instrument /LAPI/, *Space Science Instrumentation*, *5*, 465–475, 1981.

Winningham, J. D., J. L. Burch, and R. A. Frahm, Bands of ions and angular V's: A conjugate manifestation of ionospheric ion acceleration, *Journal of Geophysical Research*, *89*, 1749–1754, 1984.

Wolf, R. A., The quasi-static (slow-flow) region of the magnetosphere, in *Solar-terrestrial Physics: Principles and Theoretical Foundations*, edited by R. L. Carovillano and J. M. Forbes, vol. 104, p. 314, D. Reidel Publishing Company, 1983.

Wolf, R. A., *Introduction to Space Physics*, chap. 10, pp. 288–329, Cambridge University Press, 1995.

Yau, A. W., H. G. James, and W. Liu, The Canadian Enhanced Polar Outflow Probe (e-POP) mission in ILWS, *Advances in Space Research*, *38*, 1870–1877, 2006.